The ABC Effect in Double-Pionic Fusion to Deuterium

Dissertation

zur Erlangung des Grades eines Doktors
der Naturwissenschaften
der Fakultät für Mathematik und Physik
der Eberhard-Karls-Universität Tübingen

vorgelegt von
Olena Khakimova
aus Novokuznezk

2009

Tag der mündlichen Prüfung: 17. April 2009

Dekan: Prof. Dr. W. Knapp

1. Berichterstatter: Prof. Dr. Heinz Clement

2. Berichterstatter: Prof. Dr. Gerhard Wagner

Kurzfassung

Der ABC-Effekt wird bei der 2π-Produktion in Nukleon-Nukleon oder Nukleon-Kern-Stößen beobachtet, wenn eine Fusion des Projektils mit Targetnukleonen auftritt. Als ABC-Effekt bezeichnet man eine Überhöhung des differentiellen Wirkungsquerschnitts bei kleinen invarianten $\pi\pi$-Massen. Er wurde zuerst in inklusiven Messungen der doppelt-pionischen Fusion von Deuterium und Wasserstoff zu ^3He entdeckt. Später wurde er auch in inklusiven Messungen der Reaktion $np \to d\pi\pi$ mit einem Neutronen-Strahl beobachtet.

In dieser Arbeit werden erste exklusive Messungen der Reaktion $pd \to pd\pi^0\pi^0$ durchgeführt und zwar bei Strahlenergien von $T_p = 1.03$ und 1.35 GeV am CELSIUS Speicherring in Uppsala/Schweden. Der WASA Detektor kann geladene und neutrale Teilchen im nahezu gesamten 4π-Raumwinkelbereich nachweisen. Deuteronen wurden im *Forward Detector* gemessen, während die 4 Photonen, die aus dem Zerfall von $2\pi^0$ entstanden, im *Central Detector* nachgewiesen wurden.

Die gewählten Strahlenergien sind sehr nahe am Maximum des totalen Wirkungsquerschnittes der Reaktion $pn \to d\pi^+\pi^-$, der bei den vorherigen inklusiven Messungen erhalten wurde. Deswegen sind sie optimal für die Untersuchung des ABC-Effektes geeignet. Die Reaktion $pn \to d\pi^0\pi^0$ wurde als quasifreie Reaktion $pd \to p_{spec}d\pi^0\pi^0$ mit einem Spektator-Proton p_{spec} sehr kleiner Energie gemessen. Weil alle Teilchen außer dem Spektator-Proton gemessen wurden, konnte sein Impuls mit Hilfe eines dreifach überbestimmten kinematischen Fits rekonstruiert werden. Mithin konnte die Fermi-Bewegung im Deuteron-Target genutzt werden, um bei gegebener Strahlenergie einen Bereich Relativenergien im pn-System zu überdecken.

Der $\pi^0\pi^0$-Kanal ist rein isoskalar und frei von Isovektor-Beiträgen. Er zeigt eine große Überhöhung im $M_{\pi^0\pi^0}$-Spektrum an der $\pi\pi$-Schwelle, die viel größer ist als in vorherigen inklusiven Messungen beobachtet und mit $\Delta\Delta$-Rechnungen vorhergesagt wurde. Im Gegensatz zu letzteren wie auch zu den inklusiv gemessenen Daten wurde eine Überhöhung bei hohen invarianten Massen $M_{\pi^0\pi^0}$ nicht beobachtet und inzwischen als 3π und η-Meson Produktion interpretiert.

Da die verfügbaren $\Delta\Delta$-Modelle die exklusiv gemessenen Daten nicht beschreiben können, wird hier eine andere mögliche Erklärung vorgestellt. Die Überhöhung bei niedrigen invarianten Massen steht in einem engen Zusammenhang mit der beobachteten resonanzartigen Struktur des totalen Wirkungsquerschnittes. Die exklusiv gemessenen Daten können beschrieben werden, wenn man eine Resonanz im isoskalaren pn-System annimmt, die überwiegend über ein isoskalares $\Delta\Delta$-System zerfällt.

Mit diesem so genannten s-Kanal-Resonanz-Ansatz erhält man eine sehr gute Beschreibung des totalen Wirkungsquerschnitts sowie der differentialen Spektren. Masse und Breite dieser isoskalaren dibaryonischen Resonanz ergeben sich zu $M_R \approx 2.36$ GeV/c^2 und $\Gamma_R \approx 80$ MeV. Diese verblüffenden Resultate wurden bereits in Phys. Rev. Lett. **102**, 052301 (2009) publiziert.

Abstract

The ABC effect is observed in the 2π-production in nucleon-nucleon or nucleon-nucleus collisions, if fusion of the projectile with the target nucleons occurs. The ABC effect is a low-mass enhancement in the $\pi\pi$ invariant mass spectrum. It was first discovered in the inclusively measured double pionic fusion of deuterons and protons to ^3He. Lateron it has also been observed in inclusive measurements of the reaction $np \to d\pi\pi$ with a neutron beam.

In this work the first exclusive measurements of the reaction $pd \to pd\pi^0\pi^0$ have been carried out at beam energies of $T_p = 1.03$ and 1.35 GeV at CELSIUS storage ring in Uppsala/Sweden. The WASA detector with almost full 4π solid angle coverage allows to detect charged and neutral particles. Deuterons were measured in the *Forward Detector*, whereas the 4 photons, which originated from $2\pi^0$ decay, detected in the *Central Detector*.

The selected energies are close to the maximum cross section of the reaction $pn \to d\pi^+\pi^-$ observed in the previous inclusive measurements. Therefore they are optimal for the study of the ABC effect. The reaction $pn \to d\pi^0\pi^0$ has been measured as quasifree $pd \to p_{spec}d\pi^0\pi^0$ reaction with a spectator proton p_{spec} of very small momentum. Since all particles except of the spectator proton have been measured, the spectator 4-momentum could be reconstructed by kinematical fits with 3 overconstraints. Hence one could exploit the Fermi motion of the target neutron to cover a range of relative energies in the pn-system for a given beam energy.

The $\pi^0\pi^0$ channel, which is purely isoscalar and free of any isovector contributions, shows a large low-mass enhancement in the $M_{\pi^0\pi^0}$ spectrum, which is much larger than observed in the inclusive measurements and also larger than predicted in previous $\Delta\Delta$ calculations. In contrast to these and also to the inclusive data a high-mass enhancement in the $M_{\pi^0\pi^0}$ spectrum was not observed and is meanwhile interpreted as 3π and η-meson production.

Since the available $\Delta\Delta$ calculations are not successful in the description of the exclusively measured data, another explanation is presented here. The enhancement in the low invariant mass $M_{\pi^0\pi^0}$ is strongly correlated with the observed resonance-like structure in the total cross section. Indeed, all exclusive data can be described, if one assumes a resonance in the isoscalar pn-system, which dominantly decays via the isoscalar $\Delta\Delta$ system.

With this so-called s-channel resonance ansatz a very good description of the data in the total cross section as well as in the differential spectra has been achieved. Mass and width of this isoscalar dibaryonic resonance are $M_R \approx 2.36$ GeV/c^2 and $\Gamma_R \approx 80$ MeV, respectively. These intriguing results have already been published in Phys. Rev. Lett. **102**, 052301 (2009).

Contents

Chapter 1

Introduction: The ABC Effect

1.1 Experimental situation

The history of the ABC effect began in 1960 with the first publication "Possible Anomaly in Meson Production in $p + d$ Collisions" [Aba60]. Three scientists Alexander Abashian, Norman E. Booth and Kenneth M. Crowe performed an experiment with a single arm magnetic spectrometer at Berkeley. They measured the reaction $pd \rightarrow {}^3He + X$ (where X could be π or $\pi\pi$) in the range of beam energies from 624 to 743 MeV at one fixed polar angle of 11.7 $^\circ$ and observed an unexpected enhancement at low X invariant masses which they called an "anomaly in meson production". Later this enhancement got the name ABC effect after the initials of the surnames of the authors.

A narrow peak with a mass of 310 MeV and a width of about 16 MeV was interpreted first as the possible existence of a new neutral particle or resonance in $\pi\pi$ system. Abashian, Booth and Crowe also tried to measure the reaction $pd \rightarrow {}^3H + X$, where only the isospin $I_X = 1$ was allowed, but due to the small number of events it was difficult to draw a firm conclusion [Aba60]. Therefore this result was regarded as tentative.

In 1961 the measurements were repeated with a new experimental setup [Aba61], which was able to measure both the ${}^3He$ and ${}^3H$ recoil particles with improved resolution and accuracy. The new data showed that the anomaly appears only in channels with $I_X = 0$ and a possible explanation was a strong s-wave $\pi\pi$ attraction with a scattering length of $a = 2.3fm$, and not a p-wave $\pi\pi$ resonance as had been claimed before [Aba60, Aba61].

Ten years later in 1971 J. Banaigs $et\ al.$ [Ban71] carried out measurements of the reaction $dp \rightarrow {}^3He + X$ at p_d = 3.25, 3.42, 3.59 and 3.76 GeV/c at Saclay. The follow up measurement in 1973 of the reaction $dp \rightarrow {}^3He + X$ with a deuteron beam with an incident momentum of $2.8 < p < 3.8$ GeV/c showed a similar result [Ban73].

Later on, the low mass $\pi\pi$ peak was also observed in several other hadronic reactions by different groups with different experimental setups.

In 1969 the experimental group at Birmingham measured the quasifree reaction on the target neutron $pd \rightarrow d(p_{spect})\pi\pi$ at $T_p = 991$ MeV [Hal69], where the proton was a spectator. They used a missing mass spectrometer at the lab angle of 4.2 ° to detect the recoil particles.

In 1971 the same reaction $dp \rightarrow d(p_{spect})\pi\pi$ but with reversed kinematics was carried out by J. Banaigs $et\ al.$ at Saclay [Ban71] . In 1978 F. Plouin $et\ al.$ measured the reaction $np \rightarrow d + \pi\pi$ with a neutron beam [Plo78]. The analysed data also show an enhancement at low $\pi\pi$ mass. Fig. 1.1 displays the results from their inclusive measurement of the reaction $np \rightarrow d+\pi\pi$ at $P_n = 1.88$ GeV and $\theta_d = 0°$. The deuteron momentum k_d spectrum shows three enhancements: two outer peaks which correspond to a low $\pi\pi$ invariant mass of the X-system (ABC), and the middle enhancement (with the question mark) which corresponds to a high $\pi\pi$ mass.

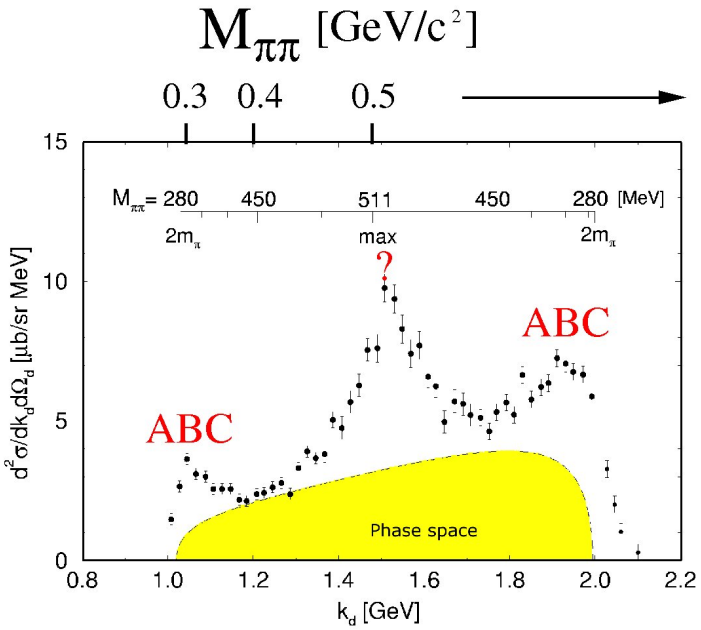

Figure 1.1: The missing momentum spectrum of the reaction $np \rightarrow d + X$, measured at $P_n = 1.88$ GeV and $\theta_d = 0°$. Note that the missing momentum in the cms is given by the measured deuteron momentum k_d. The black points are data, which have been taken from [Plo78]. The yellow area is the phase space for the 2π production. The upper scale inside the figure translates k_d into the invariant two pion mass $M_{\pi\pi}$ in a nonlinear way.

Another hadronic reaction $dd \rightarrow {}^4He + X$ at $T_d = 0.8$-2.4 GeV was measured at Saclay in 1976 [Ban76]. Since the X-system has $I = 0$, the ABC effect was expected to be seen. Indeed, the ${}^4He$ momentum spectrum also exhibits three peaks at small, middle and large ${}^4He$ momenta, which correspond to low and high invariant masses of the X-system.

Unfortunately most of the experiments have been inclusive measurements using single arm magnetic spectrometers, which means that only the outgoing nuclei

in the final channel have been detected. There was no possibility to distinguish between one, two or three pion production. Depending on the beam energy the system X could include $\pi^+\pi^-$, $\pi^0\pi^0$ pairs or even 3π or η's.

There were also several exclusive measurements of the reactions $pd \rightarrow ^3He + \pi\pi$ and $pn \rightarrow d + \pi\pi$. One such measurement was performed by the MOMO collaboration at COSY in 1999 using the magnetic spectrometer Big Karl [Bel99]. Unfortunately only the reaction $pd \rightarrow ^3He + \pi^+\pi^-$, where the $\pi\pi$-system can be both in isospin $I = 0$ and $I = 1$, was measured. Additionaly the beam energy of $T_p = 546$ MeV was too low to observe the ABC effect.

Another exclusive measurement of the $pd \rightarrow ^3He + \pi\pi$ reaction at a beam energy of $T_p = 477$ MeV was carried out by Andersson $et\ al.$ at CELSIUS in 2000 [And00]. In this case the low-statistics data were also below the ABC energy region.

In 1973 exclusive measurements of the reaction $np \rightarrow d + \pi^+\pi^-$ at neutron momenta below 3.5 GeV/c were performed at DESY with an 85 cm hydrogen bubble chamber [Bar73]. In 1979 A. Abdivaliev $et\ al.$ measured the same reaction with a neutron incident momentum $P_n = 1.73$ GeV/c at the JINR (Dubna) using a 1 m hydrogen bubble chamber [Abd79]. In both experiments the data have low statistics.

Most recently the CELSIUS/WASA collaboration performed several exclusive experiments at the CELSIUS ring in Uppsala with the WASA detector, in order to investigate the ABC effect in more detail.

In March 2005 measurements of the reactions $pd \rightarrow ^3He + \pi^+\pi^-$ and $pd \rightarrow ^3 He + \pi^0\pi^0$ at the $T_p = 895$ MeV were conducted [Bash06a]. The results show a large enhancement of the differential cross section at low $\pi\pi$ invariant masses in both channels, however the enhancement is more pronounced in the $\pi^0\pi^0$ case.

A similar result has been obtained for $dd \rightarrow \alpha + \pi^+\pi^-$ and $dd \rightarrow \alpha + \pi^0\pi^0$ at $T_d =$ 1.03 GeV, which was the final experiment at CELSIUS in June 2005 [Kel08].

In 2004-2005 the reaction $pn \rightarrow d + \pi^0\pi^0$ at $T_p = 1.037$ GeV and $T_p = 1.36$ GeV was also exclusively measured with the WASA detector at CELSIUS. This experiment and its analysis and interpretation form the subject of this thesis.

So far the ABC effect has been observed in the following reactions:

- $pn \rightarrow d + \pi^+\pi^-(\pi^0\pi^0)$
- $pd \rightarrow ^3He + \pi^+\pi^-(\pi^0\pi^0)$
- $dd \rightarrow \alpha + \pi^+\pi^-(\pi^0\pi^0)$

All these results show that the ABC effect appears in fusion reactions, i.e. in reactions leading to bound nucleons in the final state and to $\pi\pi$-system.

1.2 Theoretical situation

Since the discovery of the ABC effect many authors proposed the existence of new particles and $\pi\pi$ resonances. However the position and width of the peak varied in different reactions. In addition, the suggested large s-wave $\pi\pi$ scattering length was later contradicted by measurements of the $e^+e^- \rightarrow \pi^+\pi^-$ and $\pi N \rightarrow \pi\pi N$ reactions.

In 1973 T. Risser and M.D. Shuster in the paper "Anomalous enhancements in multiple-pion production with deuterons" gave a theoretical analysis of the reaction $pn \rightarrow d + \pi\pi$ [Ris73]. Since the ABC effect appeared at beam energies corresponding to the double-delta excitation, they suggested that the two pions are dominantly produced via a $\Delta\Delta$ excitation.

The calculations lead to three enhancements in the deuteron momentum spectra (see Fig. 1.1). The two outer peaks correspond to low $\pi\pi$ invariant masses, the first at low momentum to the case, where the deuteron flies backward in the cms but forward in lab system, and the second at high momentum corresponds to the situation where the deuteron goes forward in both the cms and the lab system. The middle bump belongs to high invariant $\pi\pi$ masses.

In the invariant mass spectrum the low-mass enhancement then corresponds to the parallel decay of two Δ with small relative momentum, i.e. the two pions move in parallel from the $\Delta\Delta$ system, while the high mass peak appears, when two Δ decay antiparallel to each other and the relative momentum is maximal, i.e. the two pions move in antiparallel from the $\Delta\Delta$ system.

The low $\pi\pi$ mass peak is more dominant when $\sqrt{(s)} \leq 2M_\Delta$, while the high-mass enhancement is expected to be more pronounced at $\sqrt{(s)} > 2M_\Delta$ [Ris73, Mos99].

In 1999 C.A. Mosbacher and F. Osterfeld presented a new calculation of $\Delta\Delta$ and ΔN excitations in the reaction $np \rightarrow d + \pi\pi$ [Mos99]. This model includes contributions from π, ρ, ω, and σ exchange and takes into account two different reaction mechanisms: $\Delta\Delta$ excitation and ΔN intermediate state. Fig. 1.2 shows the Feynman diagrams of the two pion production in the $np \rightarrow d + \pi\pi$ reaction.

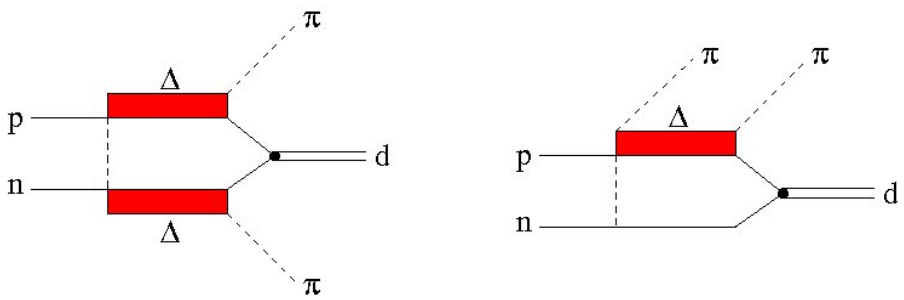

Figure 1.2: The Feynman diagrams used in [Mos99]: excitation of a $\Delta\Delta$ intermediate state, where both Δ each decay into a pion and a nucleon (left) and a ΔN resonance, where 2 pions couple to the same Δ (right).

As shown above (see Fig. 1.1) the missing momentum spectra from inclusive measurements [Plo78] exhibit a three peak structure. In Fig. 1.3 it can be seen that this model is able to explain to some extent the characteristic structure of the deuteron momentum distribution. The red solid line displays the full calculation with all intermediate interactions and the dashed line represents only the ΔN mechanism. This indicates that the $\Delta\Delta$ mechanism is the only important contribution to two pion production in the ABC energy region, while the ΔN excitation is practically negligible.

The calculations show a good agreement with the inclusive experimental data at high $\pi\pi$ invariant masses but underestimate the cross section at low $\pi\pi$ masses (outer peaks), i.e. the ABC effect.

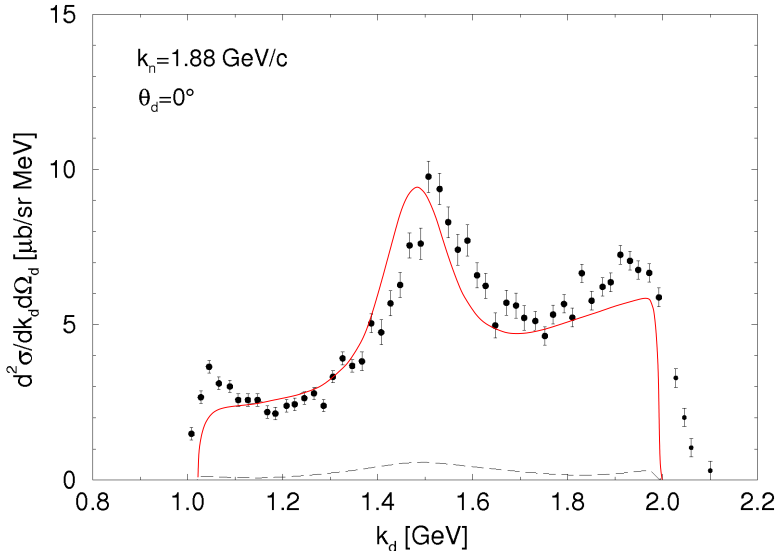

Figure 1.3: Theoretical calculation [Mos99] in comparison with the experimental data [Plo78]. The solid red line represents the calculation with all intermediate interactions and the dashed line displays only ΔN excitation contribution.

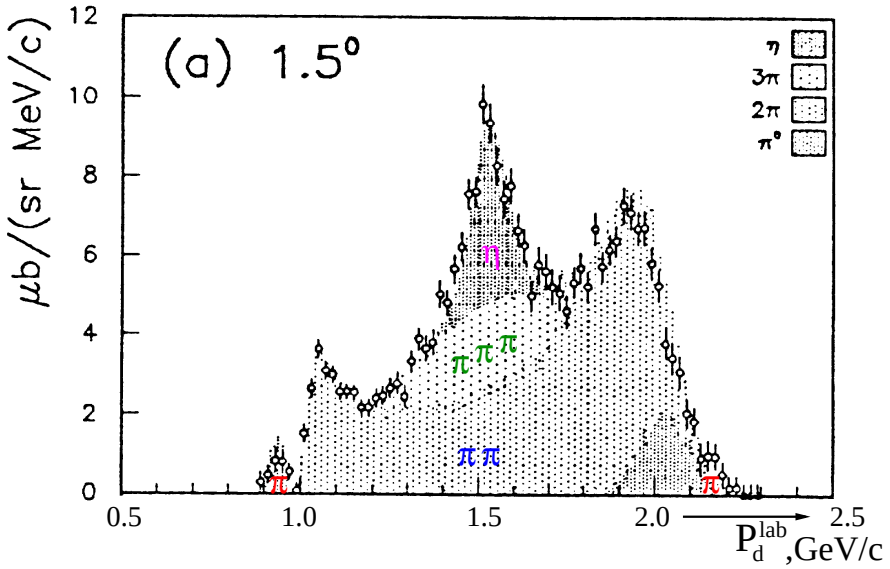

Figure 1.4: Deuteron momentum distribution of the reaction $np \rightarrow d + X$ and its interpretation in [Plo78].

Since all the previous measurements were inclusive, which means only a d or He have been detected, the X-system could also include the 3π or η production. Therefore it was suggested that the central peak in the momentum spectrum could be from 3 pion and η production [Plo90] (see Fig. 1.4).

Since up to 2004 there had been no exclusive data on this field available, the first exclusive measurements of the reaction $pn \rightarrow d\pi^0\pi^0$ have been carried out using the WASA 4π detector at the CELSIUS Ring in Uppsala, the result of which will be presented in the following chapters.

Chapter 2

Experimental Setup

2.1 The Theodor Svedberg Laboratory - TSL

The experiment presented in this thesis took place at the national accelerator facility, the Theodor Svedberg Laboratory (TSL) in Uppsala (Fig. 2.1). The TSL was founded in 1986 by researchers from Sweden and abroad and operated from 1994 to 2005 .

TSL houses two accelerators, the Gustaf Werner cyclotron and the CELSIUS storage and cooler ring. The Gustaf Werner cyclotron delivers beams of light and heavy ions and acts as ion-injector for the CELSIUS ring.

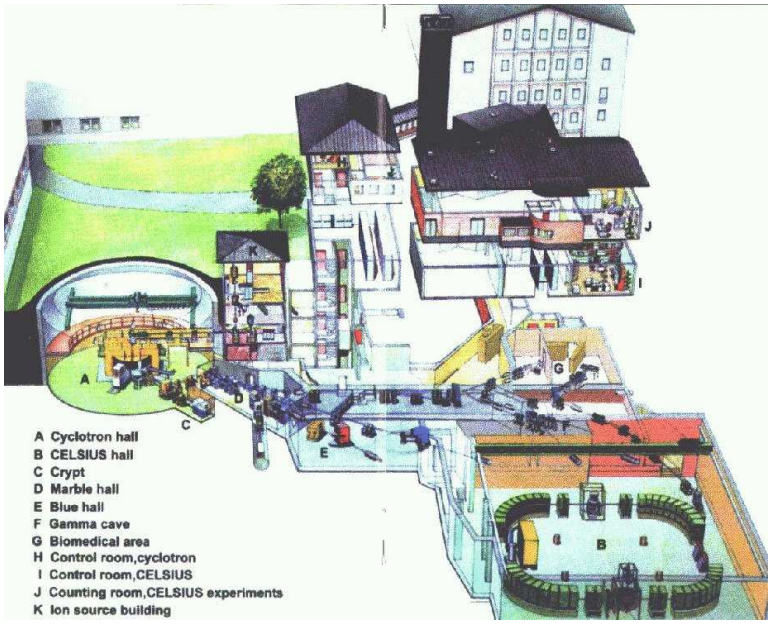

Figure 2.1: Drawing of the Svedberg Laboratory (TSL)

2.2 The CELSIUS storage ring

In 1982 it was proposed to build the CELSIUS storage ring in Uppsala. CELSIUS is an acronym for **C**ooling with **EL**ectrons and **S**toring of **I**ons from the **U**ppsala **S**ynchrocyclotron. The CELSIUS ring provides a high energy circulating beam of protons and charged ions. The maximum kinetic energy for protons was 1.45 GeV and for ions with a charge-to-mass ratio of one half it was 0.52 GeV per nucleon.

CELSIUS consisted of four quadrants, each with ten dipole magnets and two quadrupole magnets. The four straight sections contained a cluster-jet target, a pellet target system, the injection elements and some beam diagnostics equipment and an electron cooler. The cluster-jet target was used by the CHICSi facility for proton-nucleus and nucleus-nucleus reaction studies, while the pellet target was used with the WASA 4 π detector.

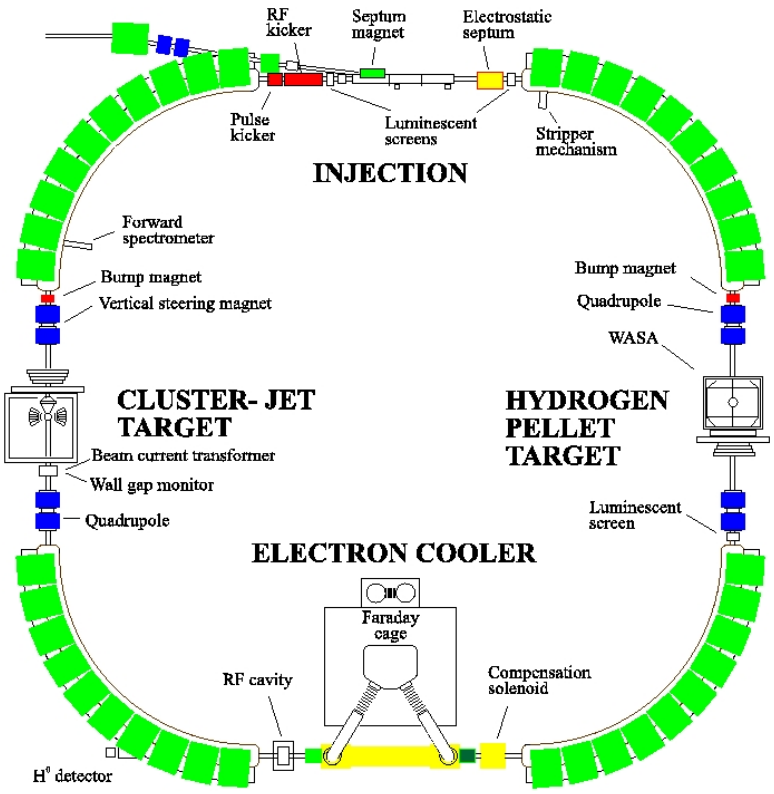

Figure 2.2: The CELSIUS Storage Rings

CELSIUS was operated in cycles with parts for injection, acceleration, flat top and return of the magnetic fields to their values for injection.

Two different injection methods were available, the multiturn injection (without stripping) and the second and more preferable stripping injection.

During stripping injection the accelerated ions, H_2^+ or D_2^+ , passed through a carbon foil with a thickness of 40 μ g/cm^2, which was mounted on the entrance to the CELSIUS ring for stripping the electrons from the ions.

After injection the ions were accelerated up to the desired energy using an RF cavity and then stored in the ring by a constant magnetic field. During the flat top the experimental data were taken. At the end of a cycle the magnetic field was returned to the values used for injection.

The typically duration of cycles was 3 to 15 minutes.

2.3 The pellet target

One of the major parts of the WASA set-up is the pellet target system. It provides frozen droplets of deuterium or hydrogen of diameters 25-35 μm. The principle of operation is as follows:

- deuterium (hydrogen) gas is cooled down by the cold head until it liquefies (triple point temperature = 14 K for hydrogen).
- a jet of liquid deuterium is pushed through the jet nozzle into the droplet chamber, where it is broken up into droplets by a piezo-electrical transducer. The typical transducer frequency is 70 kHz.
- the droplets are injected into a vacuum through the vacuum injection capillary.
- the droplets are cooled down by evaporation and are completely frozen after travelling a short distance in the vacuum and form so called pellets, which then interact with the beam.

Finally after an interaction with the beam the pellets are collected in the cryogenic dump placed under the detector. Some main parameters of the pellet target are listed in Tab. 2.1.

Pellet target parameters	
Pellet diameter	25μm
Pellet frequency	$10 - 20kHz$
Pellet stream divergence	0.04°
Effective target thickness	$10^{15} - 10^{16}$ atoms/cm^2
Pellet tube diameter at the CELSIUS beam	5 mm

Table 2.1 Design parameters of the pellet target system

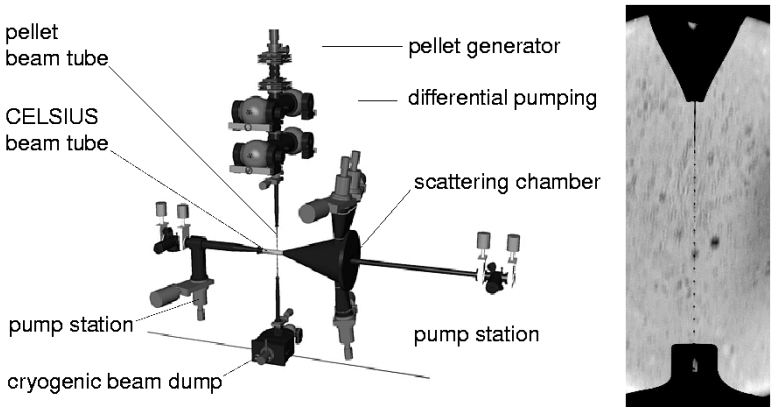

Figure 2.3: Schematic view of the pellet target system

2.4 The WASA Detector

The WASA Detector was designed initially for studies of rare decays of light mesons, especially π^0 and η mesons. WASA provides the possibility of realizing measurements at a high luminosity of $10^{32} cm^{-2} s^{-1}$ and with almost full solid angle coverage. The WASA detector consists of three parts:

- the *Central Detector*, mainly suitable for measurements of mesons and their decay products.
- the *Forward Detector*, which allows one to measure angle and kinetic energy of charged particles and to some extent also neutral particles.
- a zero degree spectrometer, which is located at the CELSIUS dipole magnet downstream of the target and is used for tagging $\eta's$ in $pd \rightarrow {}^3He\eta$ reactions by detecting ${}^3He$ escaping into the beam pipe. The spectrometer was not used in the present analysis.

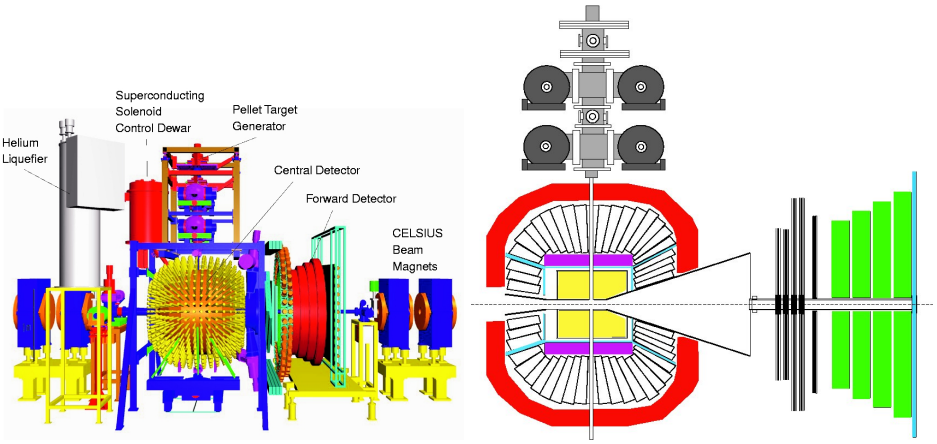

Figure 2.4: CAD view and the cross section of the WASA Detector Setup

2.4.1 The Central Detector - CD

The main purpose of the CD is to detect and measure high energy gammas and electrons coming from meson decays, but it can also be used to detect charged pions. The photons are measured in the electromagnetic calorimeter, which covers scattering angles from 20° to 169°. Charged particle identification is possible due to the magnetic field, which is provided by the superconducting solenoid, and done by a $p - \Delta E$ and $E - \Delta E$ technique, respectively, using momentum information from the Mini Drift Chamber and deposited energy from Plastic Scintillator Barrel and Scintillator Electromagnetic Calorimeter.

The Mini Drift Chamber - MDC

The MDC is the central tracking device of the CD and surrounds the beryllium beam pipe. It was developed and built by the Dubna/Russia group.

The MDC is a cylindrical drift chamber consisting of 1738 thin aluminized mylar straw tubes in 17 cylindrical layers. Nine layers are parallel to the beam direction and eight layers are skewed by a small angle of 6-9 degrees with respect to the beam axis. The pellet pipe goes vertically through the MDC (see Fig. 2.4). The readout electronics of the MDC consist of a preamplifier and a discriminator for each tube.

The MDC fulfills the following tasks:

- it delivers the momentum and scattering angles of charged particles.
- it provides the vertex position of the reaction.

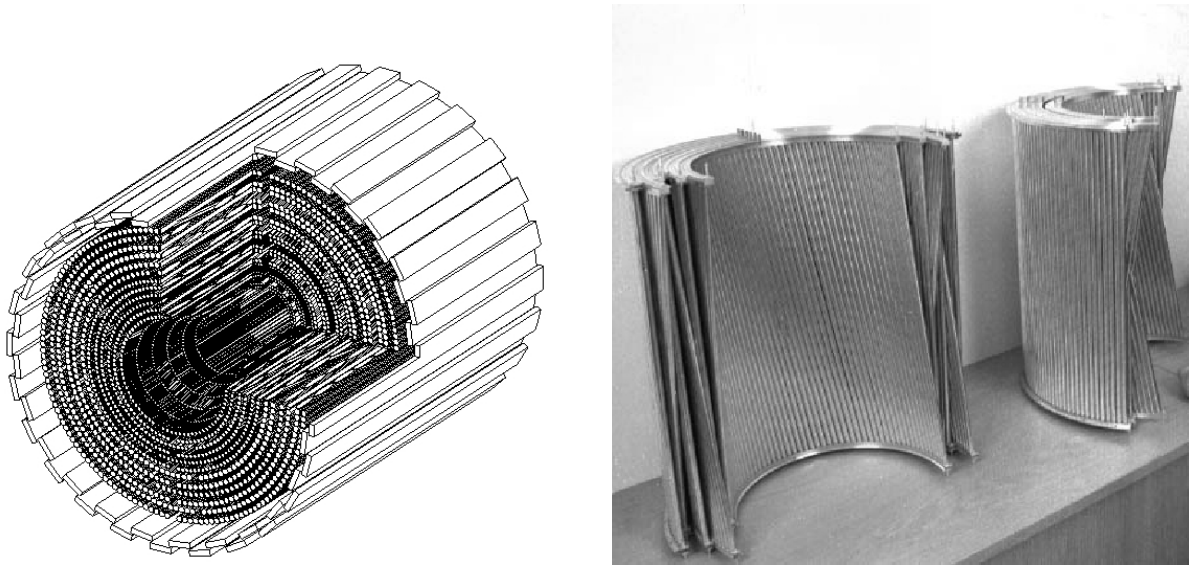

Figure 2.5: 3D CAD view of the MDC

The Plastic Scintillator Barrel - PSB

The PSB was built in Warsaw/Poland and placed between MDC and Superconducting Solenoid. It consists of 3 parts: cylindrical central and circular forward and backward parts. The radius of the circular parts is 230 mm and the length of the cylindrical part amounts to 550 mm. It is made of 8 mm thick plastic scintillators and is composed of 146 elements in total.

The Plastic Barrel provides fast signals for triggers as well as particle identification information using the $p - \Delta E(E - \Delta E)$ technique.

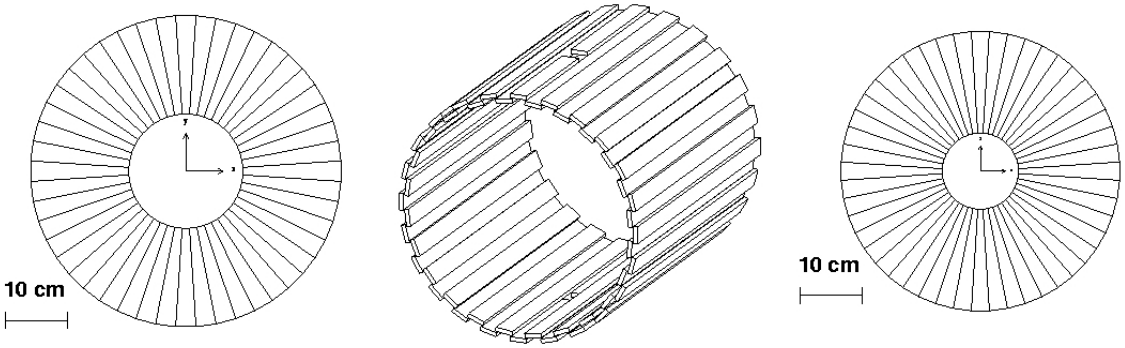

Figure 2.6: Drawing of the Plastic Barrel (PSB)(front, central and backward parts)

The Superconducting Solenoid - SCS

The SCS is an ultra-thin-walled superconducting solenoid magnet, which provides a central axial magnetic field of up to 1.3 Tesla. It allows the measurement of charged particles momenta in the MDC. It also used to protect the CD against low energy delta electrons produced in beam-pellet interactions. The magnet, with a mass of 20 kg, is placed inside the Calorimeter and has a thickness of 0.18 radiation lengths, which is equivalent to 2.6 mm of copper or 16 mm of aluminium. The cooling system with liquid helium provides a coil temperature of 4.7 K.

The Scintillator Electromagnetic Calorimeter - SEC

The last layer of the CD is the SEC, which is installed between SCS and iron yoke. It consists of 1021 sodium-doped CsI scintillating crystals, which have different shapes and lengths and are placed in 24 layers along the beam. The advantage of inorganic crystals is their high stopping power due to their high density and high atomic number.

The SEC consists of 3 parts: central (SEC), forward (SEF) and backward (SEB). The crystals were grown in Kharkov/Ukraine, then transported to Novosibirsk/Russia and prepared for the experiment.

The SEC was designed to detect and measure charged and neutral particles.

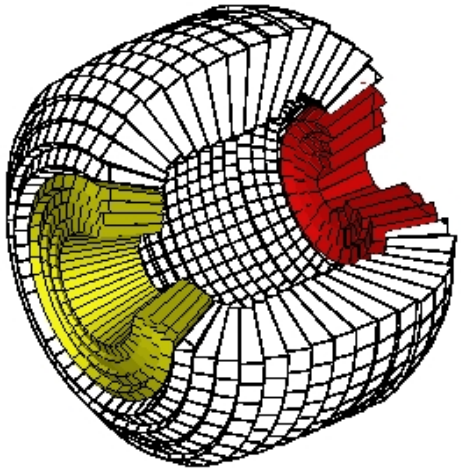

Figure 2.7: View of the Scintillator Electromagnetic Calorimeter. The SEF part is marked by red color, the SEC part is white and the SEB part is shown by yellow color.

2.4.2 The Forward Detector - FD

The FD covers scattering angles from 3° to 18°. It has an angular resolution of 0.2 degree and a time resolution of < 3 ns.

The FD mostly consists of several plastic scintillator planes, which are used for particle identification via $\Delta E - E$ technique and which also provide fast signals for the first level trigger. The maximum kinetic energy for stopping of $\pi's$ is 170 MeV, for protons about 300 MeV and for deuterons 400 MeV.

In the measurements described in this work almost all particles punched through the detector, i.e. their energy had to derived from the deposited energies in different detector planes.

Forward Window Counter - FWC

The FWC is a thin trigger hodoscope which was designed and built by the Tübingen group. This first layer of the FD consists of 12 scintillators, each 5 mm thick and inclined by 10 degree relative to the normal plane of the beam pipe. The FWC provides signals for the first level trigger.

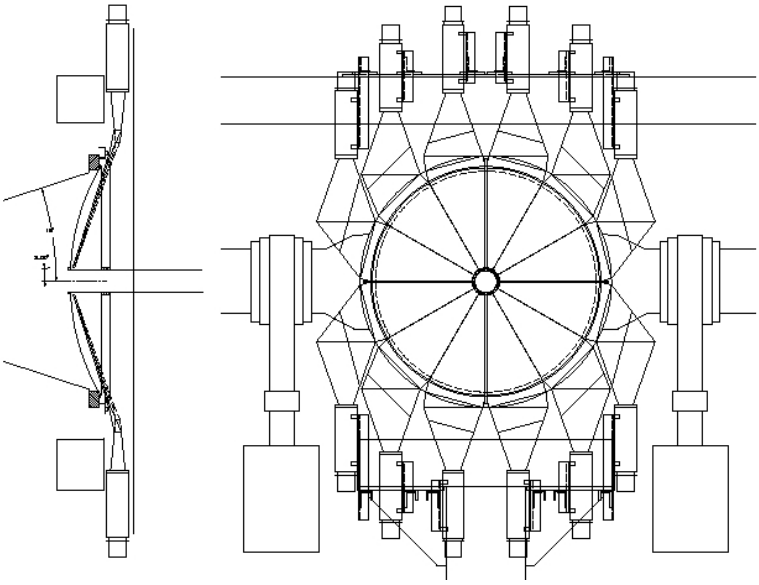

Figure 2.8: Forward Window Counter: side view (left) and front view (right)

The Forward Proportional Chamber - FPC

The second layer after the FWC is FPC. It was built by the Uppsala group. Originally 4 modules were projected for track detection in four different directions. During the beam time of the measurement described in this thesis only two of four modules were installed.

Each module consists of 4 layers with 122 proportional drift tubes (straws) of 8 mm diameter. The straws are made from aluminized mylar of 26 μm thickness with a sense wire of stainless steel of 35 μm diameter inside. This tracking device is used for accurately measuring and reconstructing the scattering angles of charged particles.

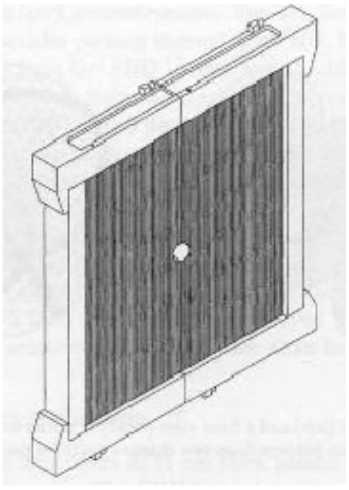

Figure 2.9: View of the Forward Proportional Chamber

The Forward Trigger Hodoscope - FTH

The FTH was built in Jülich, therefore it also is called Forward Jülich Hodoscope or "Jülich Quirl".

It consists of three layers each of 5 mm thick plastic scintillators (BC404). The first two layers are composed of 24 Archimedian spiral shaped elements, while the third layer is segmented into 48 pizza-like elements. The angular resolution is 1.2 ° for the polar angle and 4.6 ° for the azimuthal angle.

The FTH is particularly suitable as a trigger for detection of particles and to deliver a fast signal for the first level trigger. The third layer of the FTH together with the Forward Range Hodoscope (see the next section) is usually used for particle identification via the $\Delta E - E$ technique.

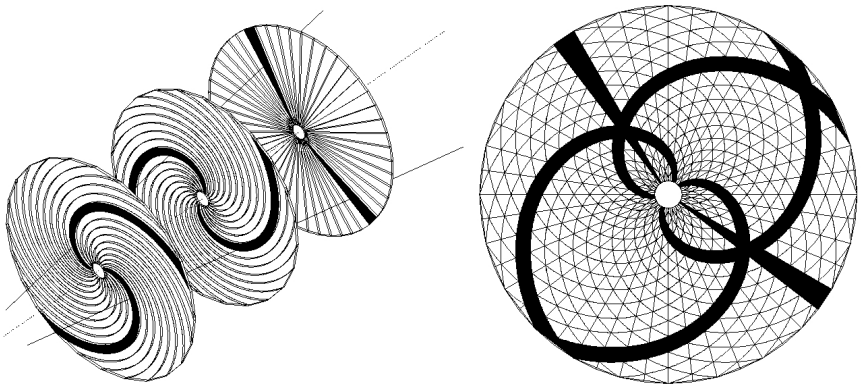

Figure 2.10: Forward Jülich Hodoscope

The Forward Range Hodoscope - FRH

The FRH is a calorimeter composed of four layers of plastic scintillators (BC400) each layer being 11 cm thick and thus the largest part of FD. It was built by the Warsaw group. Each layer is divided into 24 cake-like segments of 15 ° (polar angle). Their radii increase from 53 to 71 cm (see Fig. 2.11). It is placed behind the FTH in such a position that one FRH sector covers two FTH sectors of the third layer.

The FRH is mainly used for energy determination of charged particles flying through the detector and also for particle identification by the $\Delta E - E$ method.

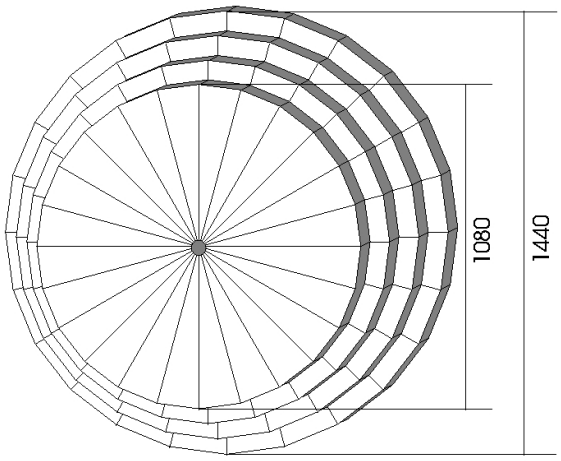

Figure 2.11: Forward Range Hodoscope

The Forward Range Intermediate Hodoscope - FRI

The FRI is a thin layer of scintillator counters placed between the third and fourth layers of the FRH. This detector was built by the Hamburg group. It consists of two planes of 32 plastic scintillator bars in a crossing geometry. The bars are 5 mm thick and 3 cm or 6 cm wide growing in length from the beam pipe towards the outside. The FRI was designed to improve the angular hit resolution in ϕ and to give better position information for particles. It is also used to measure neutron angles via detecting the position of recoil protons.

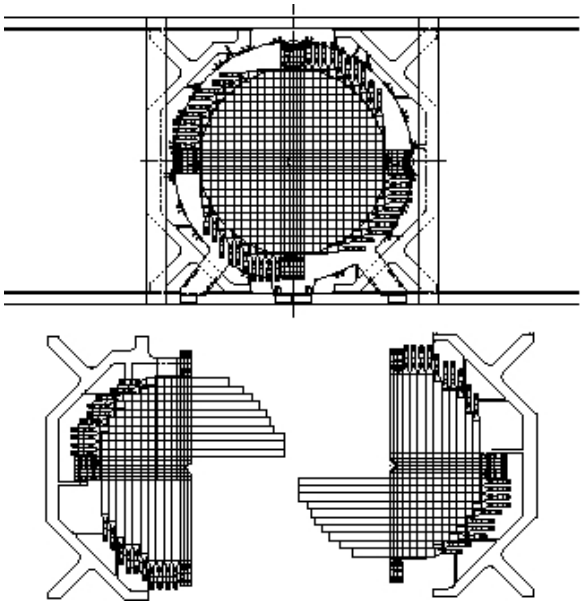

Figure 2.12: Forward Range Intermediate Hodoscope

The Forward Veto Hodoscope - FVH

The last layer of the FD is the FVH. It was built by the Tübingen group. It consists of 12 horizontal plastic scintillator bars, each 2 cm thick, 13.7 cm high and 165 cm in length. It detects particles punching through the FD and serves as veto counter in the first level trigger.

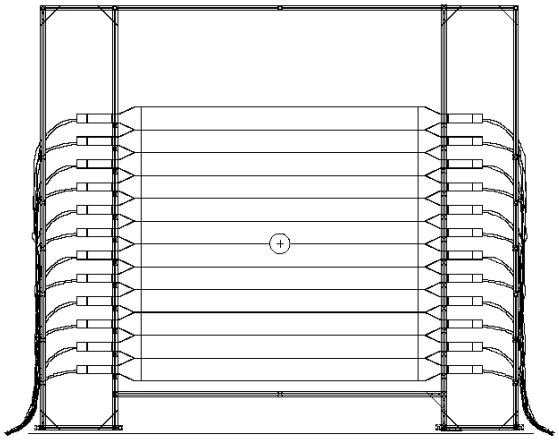

Figure 2.13: Forward Veto Hodoscope

2.5 The Data Acquisition System (DAQ)

The DAQ hardware is an interface between the signal and computer.

The scheme of the DAQ for the WASA experiment is shown in Fig. 2.14. It works in the following way: the analog signals from all detectors are transfered from the experimental hall to the electronics hut by RG58 cables. Then the signals are divided into two branches in splitter-delay boxes. Signals from one of them are delayed by 300 ns and then passed to Analog-to-Digital Converters (ADCs/QDCs), while the other branch sends signals to discriminators. The discriminated signals in turn are also split for Time-to-Digital Conversion (TDC) and for the trigger system.

The digital electronics used Fastbus crates: Lecroy 1881 QDCs and Lecroy 1876 TDCs. The data collected in the Fastbus crates were delivered to the event builder (VME) and then distributed to the monitoring stations via a parallel 32-bit RS485 data link. The link provides data transfer with a speed of 40 Mb/s. The data were then stored on DLT tapes and discs.

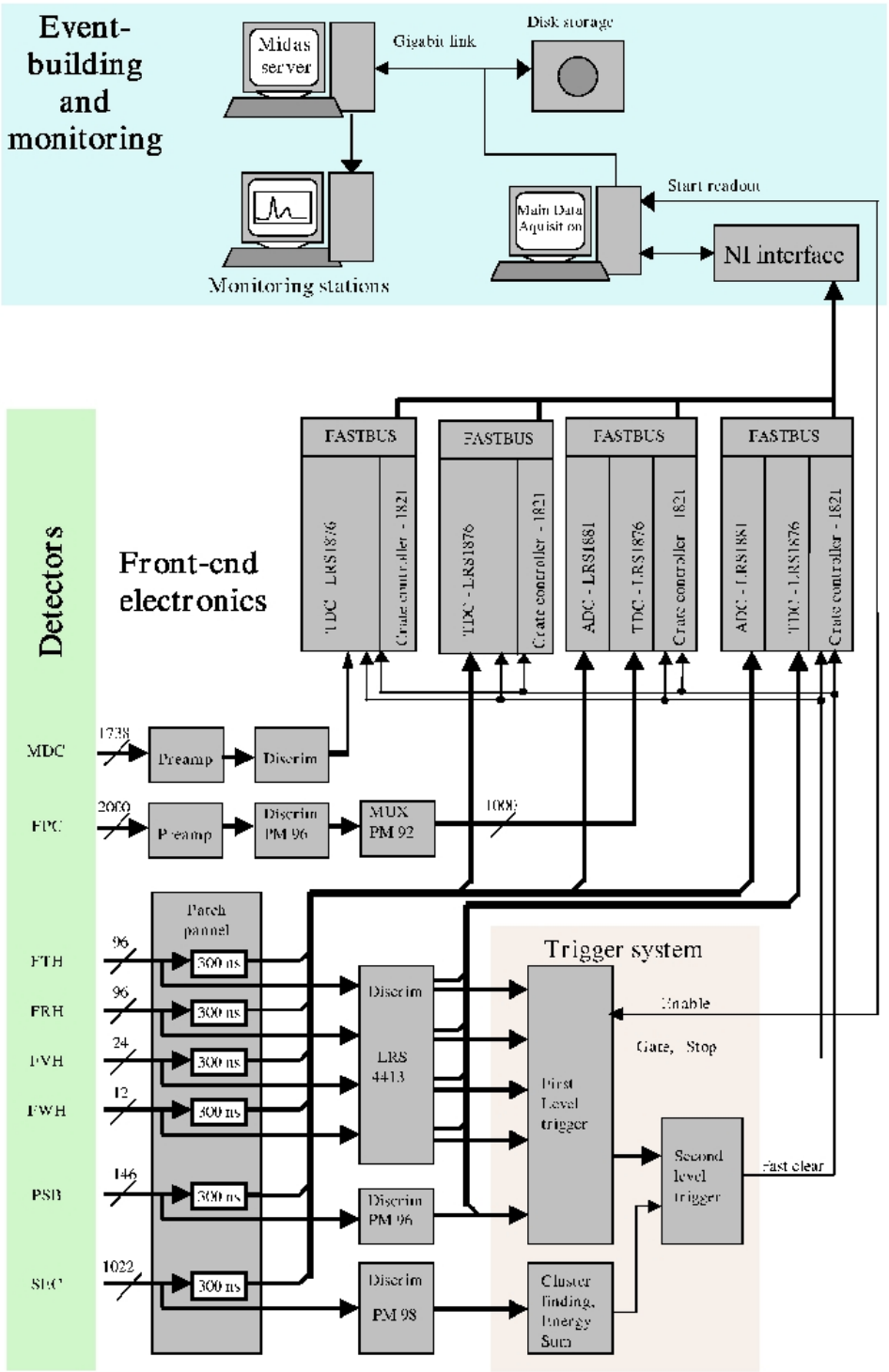

Figure 2.14: The Data Acquisition System for WASA

2.6 The Trigger System

The triggers are used to select a particular reaction from the manifold of other reactions which are produced simultaneously. In order to do so, certain conditions (criteria), which identify the reaction, e.g. coincidence between two or more detectors, number of particles in outgoing channels etc. have to be met.

Originally the WASA trigger system was supposed to be organized in three levels. But the software-based third level has not been implemented. Therefore the system has two levels: the first level operates on fast plastic scintillator detectors, such as the FD scintillators and the PSB and is intended for triggering the data aquisition system and producing the gates and strobe signals (start) for the front-end electronics, whereas the second level is designed for reconsidering events taking into account additional information about the cluster multiplicity and energy deposition from slower detectors, like the SEC. The multiplicity of clusters and a quickly calculated deposited energy sum give the possibility for additional cuts in the trigger rate.

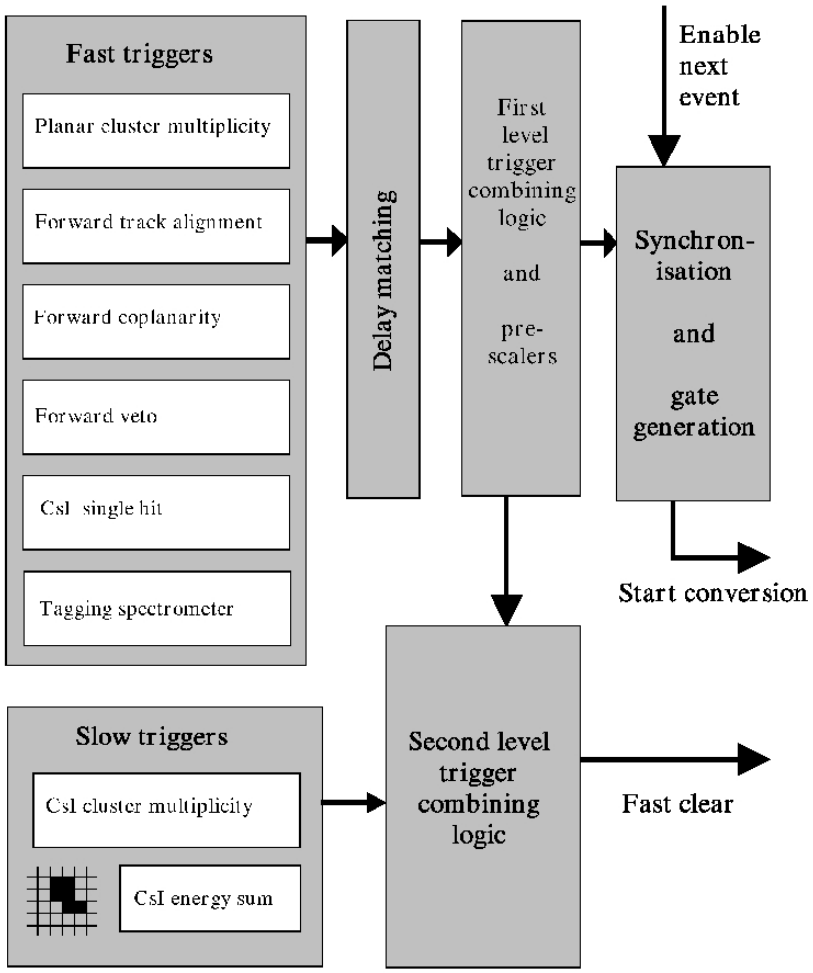

Figure 2.15: Trigger system for WASA

Chapter 3

Analysis Tools

This chapter gives an overview of the software package used in the data analysis. During the experiment the raw data have been saved on hard disks and backed up on DLT tapes in digital format. The task of the offline analysis is to reconstruct the four-momentum vectors of the detected particles. For better understanding and interpreting the experimental data Monte Carlo simulations of the detector response are performed. A identical way in treating real and simulated data is very important for reliable acceptance and efficiency corrections of the experimental data. Fig. 3.1. presents the analysis procedure.

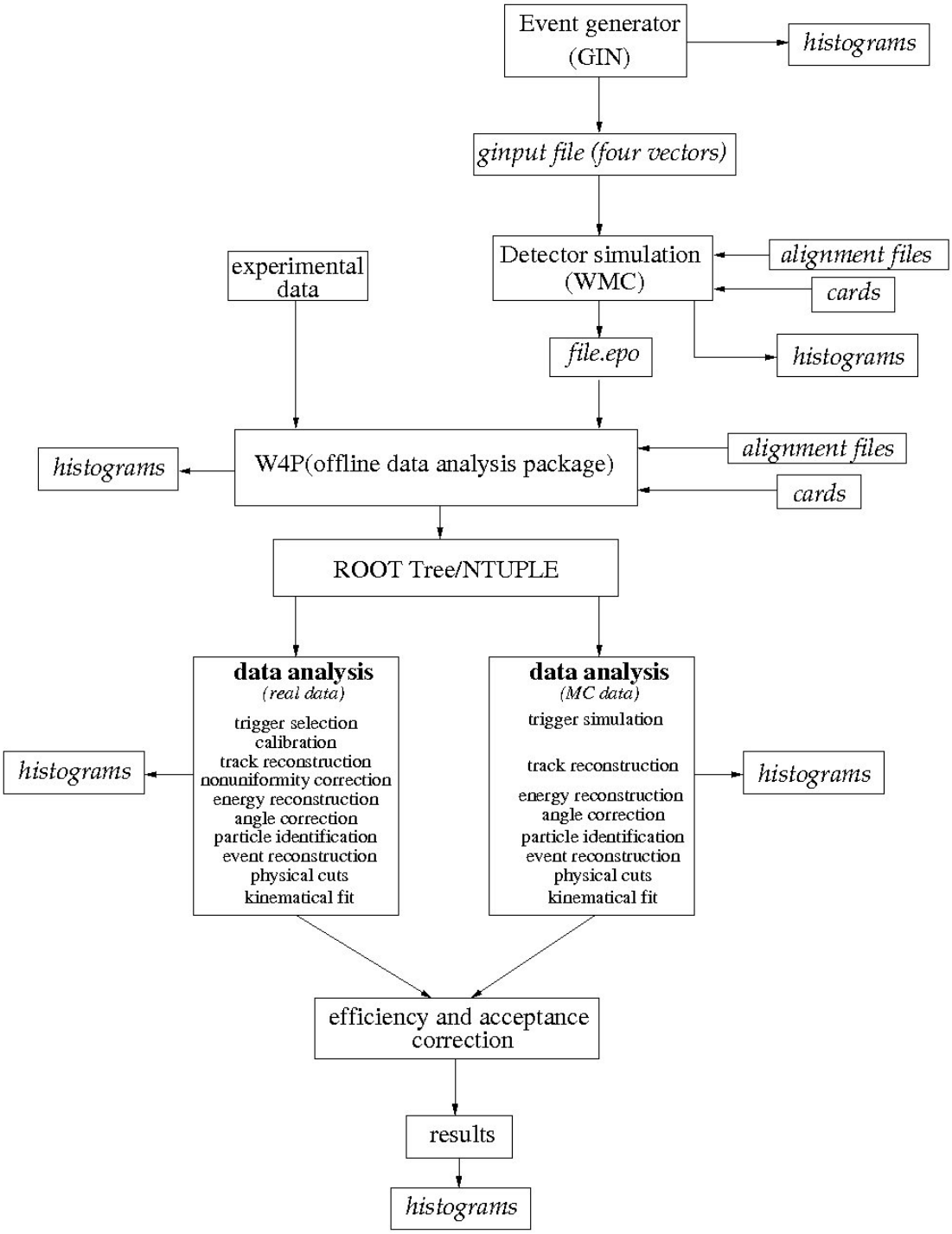

Figure 3.1: Flow chart of the analysis tools.

3.1 The Phase Space Event Generator - GIN

For the generation of simulated data the ROOT Event Generator has been used. The generator is a phase space generator and implemented in the code as TGenPhaseSpace class [1].

The event generator generates an event of the chosen channel after defining the masses of the ingoing and outgoing particles, beam and target, and the energy of the beam in such a form that energy and momentum are conserved. The event is generated in the center-of-mass frame, but the decay products are finally boosted into the lab system by a Lorentz transformation. The output contains the four momentum vectors. The same algorithm is used in the GENBOD function (CERNLIB).

One can also implement some geometrical cuts or define "toy"-models by modifying the event weights.

The GIN program produces a ASCII output data file, which later will be used as input to the Monte-Carlo Simulations of the detector response.

3.2 The Wasa Monte Carlo Simulation - WMC

The WMC Simulation is the detector Monte Carlo simulation for the WASA experiment. The aim of the simulation is to choose geometry and material of the detector as close as possible to the real setup. The software package is based on the GEANT3 programm from CERN.

The GEANT software contains many different subroutines, which provide:

- the transport of particles through the experimental setup taking into account the interactions with the material and magnetic field
- the graphical visualisation of the detector and the particles trajectories
- the response of the detector elements

Fig. 3.2 shows the simulated WASA setup. One can see the central and the forward parts of the detector, consisting of different chambers and plastic scintillator layers as described in Chap. 2. As an example the simulation of the reaction $pn \rightarrow d\pi^0\pi^0$ is shown. In this case two pions go into the *Central Detector*, where they decay into four gammas and create showers. The deuterons punch through the *Forward Detector*.

The main program consists of three parts: initialisation, event processing and termination. In the initialisation phase one can define the geometry of the different components of the setup and tracking medium parameters, specify which

[1] see example of use in $ROOTSYS/tutorials/physics/PhaseSpace.C

elements of the setup should be considered as a sensitive detector element, providing a signal in case of a hit by a particle. Additionally the energy loss and cross-section tables for all materials of the detector will be prepared.

In the processing part the initialisation of event processing, tracking of particles according to its type, translation of deposited energy into ADC and TDC channels as well as storage of the information of the current track segment have been done. The track of a particle through the virtual detector is divided into many small steps Δx. In each Δx the particle deposits a small amount of energy ΔE. The detection process in plastic scintillator material involves converting the deposited energy of particles into light. In principal the intensity of light emission and energy are directly proportional to each other $L \propto E$. However, not all energy is converted into light but partly dissipated through molecular excitation. This effect of quenching without light production increases with high ionisation density. The simulation of the quenching effect is done according to the Birk's formula [Leo87], where the light output is given by:

$$\frac{dL}{dx} = \frac{1}{1 + kB\frac{dE}{dx} + C(\frac{dE}{dx})^2} \tag{3.1}$$

In the table 3.1 the parameters for the different particle types are presented.

particle	kB [cm/GeV]	C [$(cm/GeV)^2$]
p	12.6	0
π	11.4	0
d	9.17	4.6

Table 3.1 Quenching parameters used for plastic scintillator material in the detector simulation [Cra70, Roz88].

Additionaly the hadronic interactions can be simulated via the hadronic shower generator.

In the termination phase some statistical information (time per event, use of dynamic memory, etc.) can be printed.

The output file is written in the EPIO format.

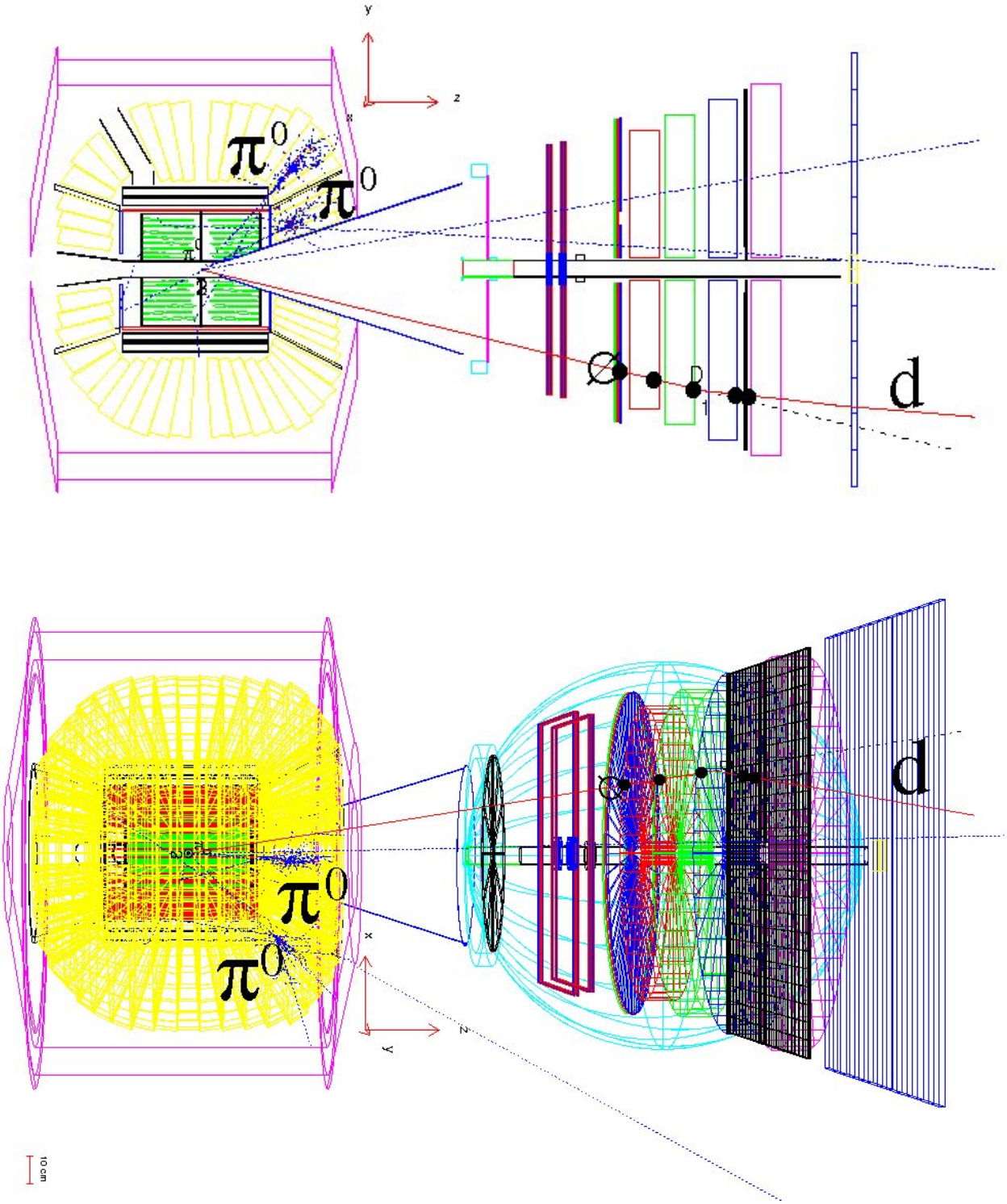

Figure 3.2: Side (top) and 3D (bottom) view of the WASA detector as described in the detector simulation. The simulation of the reaction $pn \rightarrow d\pi^0\pi^0$ at the beam energy $T_p = 1.35$ GeV is shown. Two pions are detected in the *Central Detector* while the deuteron flies into the *Forward Detector*. The pions decay after 10^{-17} s into two gammas, which each create a shower in the CD (see blue dotted lines). The deuterons punch through the FD as shown by the red solid line.

3.3 W4P Program

The W4P is the acronym for Wasa 4π. This offline data analysis package is used for track and energy reconstruction. The W4P program works in the following steps:

- read events from the input file (experimental or simulated data)
- decoding hits
- selection of the trigger
- pedestal subtraction
- energy and time calibration (ADC$\rightarrow$ energy, TDC$\rightarrow$ time)
- track reconstruction in FD and CD (hit clusters in planes, track segments in detectors)
- nonuniformity correction
- particle identification
- energy reconstruction
- building of the event from selected tracks

One should note that the analysis of experimental data and Monte-Carlo simulated events are slightly different. The input file format depends on whether experimental or simulated data are read. The output file has the hbook format and contains the track information.

3.4 ROOT Tree's/Ntuple Track Format (NTF)

The Ntuple is implemented within the Physics Analysis Workstation (PAW) from CERN. The Ntuples are 2D-arrays, which are used as a storage of analysed data for further processing. The storage requirement is proportional to the number of columns in one event and can be very large for large event samples.

Using the storage in the Ntuple Track Format can save a lot of time, because one needs to analyse events only once and store the tracks in the track format (ROOT TTree). Thereafter the analysis of the different reactions can be started already from tracks and no longer from the hit processing and track finding.

For further details concerning the Ntuple Track Format used for the analysis see [Bash06a].

3.5 Particle Identification

The particle identification method is based on the ΔE-E or ΔE-p technique. It plays an important role during the analysis. The final result depends crucially from the ability to identify a particle accurately. The WASA Detector allows to identify four possible track types:

- Charge tracks in CD (electrons, positrons, pions, protons)
- Neutral tracks in CD (photons, neutrons)
- Charge tracks in FD (electrons, pions, protons, deuterons, ^3He and ^4He)
- Neutral tracks in FD (gammas, neutrons)

In the following subsections the methods and applications will be presented in some detail.

3.5.1 Charged Particles in FD

In the passage of charged particles through matter they lose kinetic energy due to inelastic atomic electron collisions. In these collisions the passing charged particle transfers a small fraction of the total kinetic energy to the atom causing excitation or ionization. These processes were first introduced by Bohr using classical arguments and later by Bethe, Bloch and others using quantum mechanics. We used the Bethe-Bloch formula as e.g. given by [Leo87].

The forward part of the WASA detector consists of many plastic scintillator layers. The particles are identified via $\Delta E/E$ plots, i.e. the energy loss determined in each layer of FD. Usually the information from the Jülich and the Range hodoscopes is used. Fig. 3.3 shows the $\Delta E/E$ scatter plot of events detected in the FD. The particle selection has been done using a neural net analysis. A detailed description about this method in WASA can be found in [Bash06a].

3.5.2 Neutral Particles in FD

Neutral particle identification is more difficalt due to the lack of an electric charge. There are two kinds of particles, which can be identified as neutrals: gammas and neutrons. The energy loss mechanisms of photons in matter are:

- the photoeffect
- Compton scattering
- pair production and bremsstrahlung emission

The photoeffect and Compton scattering dominate at relatively low photon energies and high atomic number Z. Since in the experiments at WASA the photons energies are much higher than $2m_ec^2$, the main interaction mechanism is pair production. During this process the transformation of a photon into an electron-positron pair occurs. The electron-positron pairs emit energetic bremsstrahlung photons, which in turn convert into e^+e^- pairs. The result are electomagnetic showers of γ, e^- and e^+.

Fast neutrons can be identified by detecting recoil protons, which dominantly arise from the (n,p) nuclear reaction on hydrogen in the scintillator material.

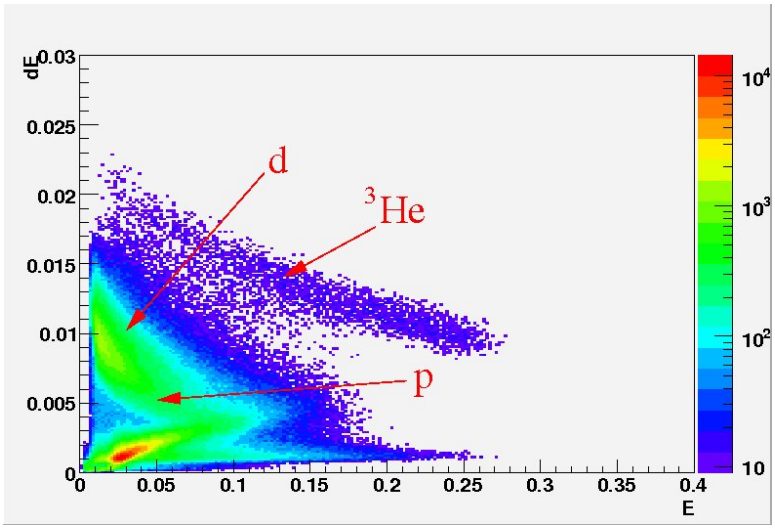

Figure 3.3: Example of particle identification in the *Forward Detector* with dE being the energy loss in the "Jülich Quirl", third layer and E denoting the deposited energy in FD. The typical dE/E plot shows ^3He, deuteron and proton "bananas". The backbent "bananas" correspond to the punch-through particles.

3.5.3 Charged Particles in CD

The CD has a solenoid magnet, which provides a magnetic field allowing determination of particle charge and momentum. The identification was done by implementation of a neural net. Fig. 3.4 shows the $\Delta E/p$ plot. One can easily distinguish between π^-, π^+ and protons.

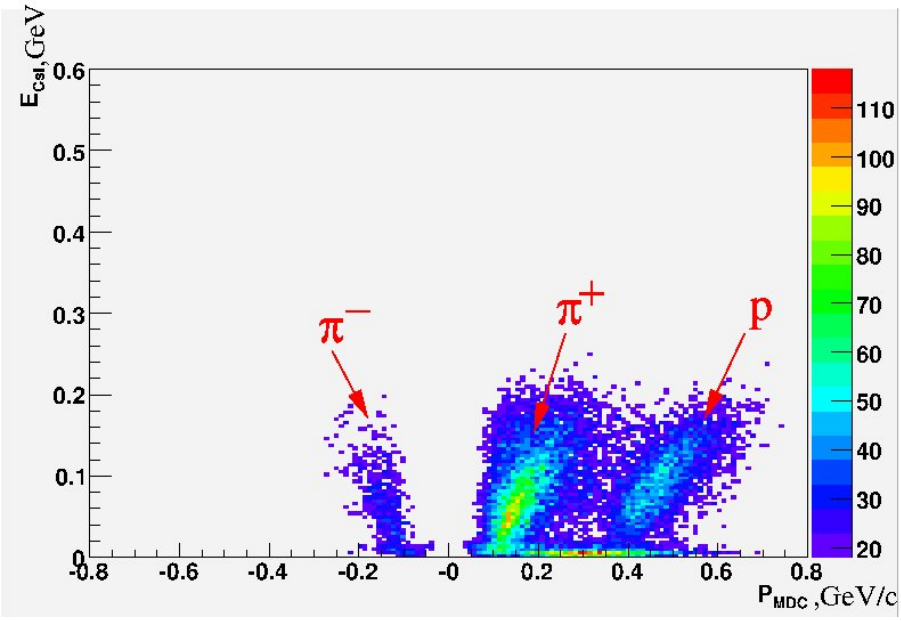

Figure 3.4: Example of charged particle identification in the *Central Detector*. The energy in the Scintillator Electromagnetic Calorimeter plotted versus momentum in the Mini Drift Chamber. On the E/p plot one can clearly distinguish between π^-, π^+ and proton events.

3.5.4 Neutral Particles in CD

There are two kinds of neutral particles in the CD: photons and neutrons. Almost all neutrons have $\theta < 40^\circ$ by kinematics in the beam energy region. Therefore only a few of them can be detected in CD, using the information from the scintillating crystals. Most of the signals are coming from photons. From the gammas detected in the calorimeter one can reconstruct the π^0 4-momenta, from which they originated. Such an example is shown in Fig. 3.5.

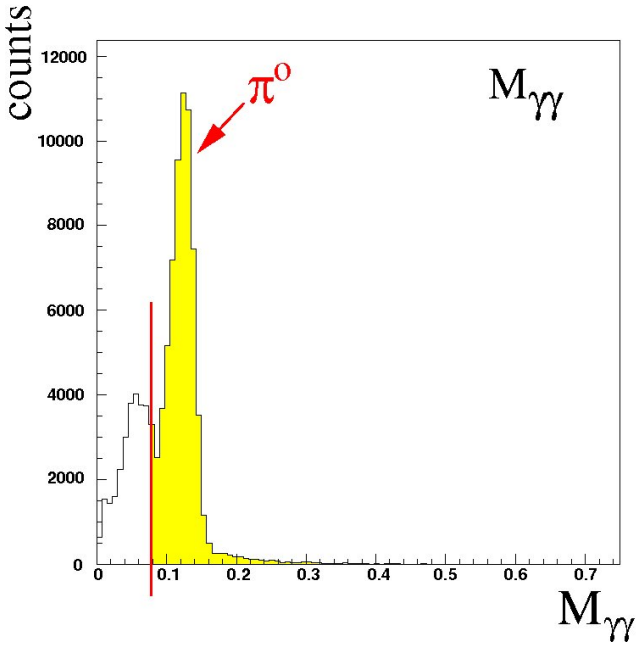

Figure 3.5: Example of neutral particle identification in the *Central Detector*. The invariant mass of two photons is shown. The usual way to identify π^0 is to detect two gammas. The yellow area corresponds to the invariant mass range accepted for the identification of a neutral pion. The red line shows the cut condition.

3.6 Energy reconstruction in the Forward Detector

The particle energy measured in the experiment is the energy deposited during the traveling of the particle through material. It is smaller than the particle had at the beginning due to dead material in the detector parts and due to the quenching effects in the plastic scintillator (see Chap. 3.2). The translation $E_{dep} \rightarrow E_{kin}$ depends on the particle type, because the effects are different for different particles.

For forward going deuterons (see Fig. 3.6) it was done in the following way: first the different conditions for the particles stopping in different layers were applied. Depending on the kinetic energy the deuterons may be stopped in FRH1 or FRH2 or FRH3 of FRH4 or punch through the *Forward Detector*. Accordingly there are five functions for the $E_{dep} \rightarrow E_{kin}$ transformation.

To give an example: the stopping energy for deuterons is 400 MeV. Since according to kinematics deuterons have kinetic energies up to 1.0 GeV, most of them do not stop but punch through the last layer FRH4. For this case the translation $E_{dep} \rightarrow E_{kin}$ is the following:

$$E_{kin} = [1 + e^{(A1+A2*E_{dep})} + e^{(A3+A4*E_{dep})} + \theta \cdot (e^{(A5+A6*E_{dep})} + \\ + e^{(A7+A8*E_{dep})})] \cdot E_{dep} \quad (3.2)$$

where $E_{dep} = E_{dep}^{FRH1} + E_{dep}^{FRH2} + E_{dep}^{FRH3} + E_{dep}^{FRH4}$ is the deposited energy in the full Forward Range Hodoscope in GeV, θ is the polar angle in radians and A1-A8 are calibration coefficients.

The coefficients A1-A8 were obtained from simulation of the reaction $pp \rightarrow d\pi^+$ at $T_p = 640$ MeV.

Table 3.2 gives an overview of the calibration constants for deuterons for different FRH stopping planes.

constants	FRH1	FRH2	FRH3	FRH4	punch through
A1	2.03227	0.468512	0.768832	9.1301	11.8193
A2 [GeV^{-1}]	-67.2193	-15.9898	-14.5199	-45.4404	-78.5049
A3	0.219912	-1.58284	-1.9609	-0.716251	3.58860
A4 [GeV^{-1}]	-9.19007	-0.549665	0.206675	-2.93309	-15.445
A5	1.37639	27.1494	30.597	7.11065	1.96028
A6 [GeV^{-1}]	-120.31	-214.319	-156.116	-36.207	-12.2744
A7	-0.925965	-1.42227	-2.63549	-17.2432	-0.0852235
A8 [GeV^{-1}]	-18.5342	-12.9962	-7.04743	37.461	0.280786

Table 3.2 Calibration coefficients for deuterons stopping in different layers of FRH in the *Forward Detector*.

3.7 Energy reconstruction in the Central Detector

The calibration procedure of the Plastic Scintillator Barrel (PSB) and the Scintillator Electromagnetic Calorimeter (SEC) used for the analysis is presented in [Jac04] and [Koc04] respectively.

The calibration constants for the PSB were obtained using the elastic reaction $pp \rightarrow pp$. The calibration of the CsI calorimeter is based on the selection of the reaction $pp \rightarrow pp\pi^0\pi^0$.

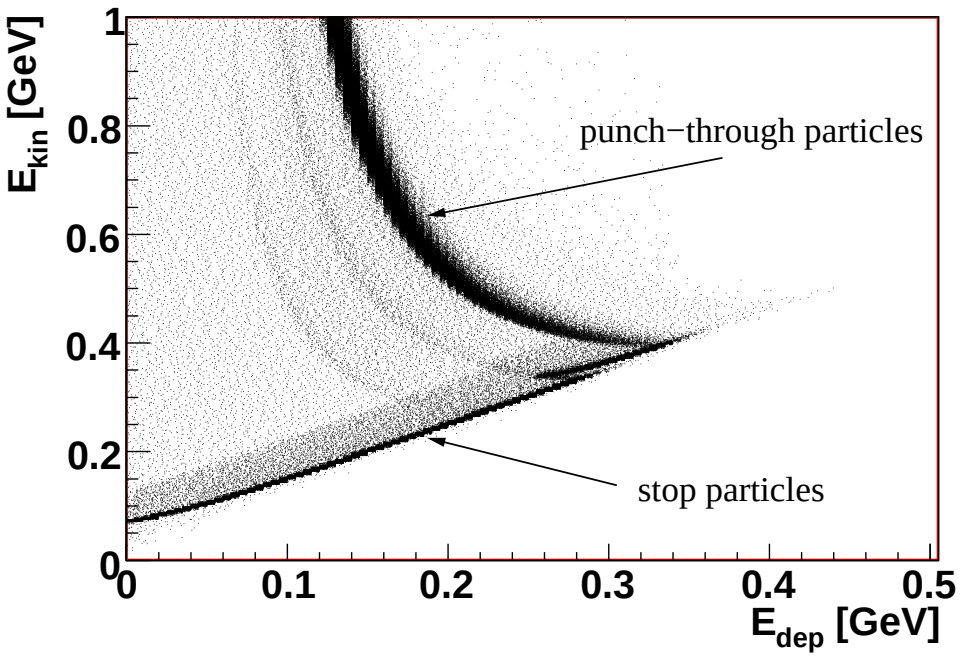

Figure 3.6: Scatter plot E_{kin} versus E_{dep} for deuterons in plastic scintillators as generated by Monte Carlo simulations. The lower band corresponds to particles, which stop in the detector, while the upper "banana" displays punch-through particles, which are identified by the signal in the FVH. The rest of distribution comes from hadronic interactions.

3.8 Treatment of the quasifree reaction kinematics

Since neutron targets are not available because of their short lifetime, the measurements of this reaction have been done by use of a deuteron target. In order to simulate such a process one assumes that the proton in the deuteron is a spectator, which influences the reaction only in terms of the Fermi motion of the bound neutron.

To check this assumption one should require the detection of the spectator proton which was performed in inverse kinematics i.e. with a deuteron beam by [Abd06]. We used a deuteron target and due to low energy of the spectator proton of only a few MeV it does not reach any detectors. In kinematically complete measurements it is possible to reconstruct the spectator. In the case of a free reaction the target particles are usually at rest while in a quasifree reaction the target nucleon moves with a momentum, which corresponds to the Fermi momentum inside the target nucleus.

In order to simulate the reaction $pn \rightarrow d\pi^0\pi^0$ one has to incorporate the spectator particle into a Monte Carlo simulation.

The momentum of the nucleons within the deuteron is calculated according to the Hulthén wave function:

$$\psi(p_F) = \frac{1}{\kappa^2 + {p_F}^2} - \frac{1}{\beta^2 + {p_F}^2} \tag{3.3}$$

where $\kappa = \sqrt{m_n \delta}$ with δ being the binding energy of deuteron, $\delta = 2.22$ MeV and $\beta = 5.2\kappa$. This Fermi momentum distribution of nucleons inside the deuteron is shown in Fig. 3.8

Fig. 3.7 represents schematically the quasi-free reaction. The spectator proton gives information carried by the off-shell neutron. According to momentum conservation inside the deuteron the neutron momentum is given as:

$$\vec{p_n} \equiv \vec{p}_{Fermi} \approx -\vec{p}_s \tag{3.4}$$

where $\vec{p_s}$ is (deduced) on-shell momentum of the spectator proton. The total energy of the free spectator proton is:

$$E_s = \sqrt{{m_p}^2 + |\vec{p_s}|^2}; \;\; (c = 1) \tag{3.5}$$

The total energy of the target neutron is then:

$$E_n \cong m_d - E_s \tag{3.6}$$

where $m_d = m_n + m_p - \delta$ is the mass of the target deuteron at rest.

Since the neutron is off-shell, the effective mass of the target neutron is lower than the mass of a free neutron:

$$m_n = \sqrt{{E_n}^2 - |\vec{p_s'}|^2} \tag{3.7}$$

In this approach we assume $\vec{p_s'}^2 = \vec{p_s}$

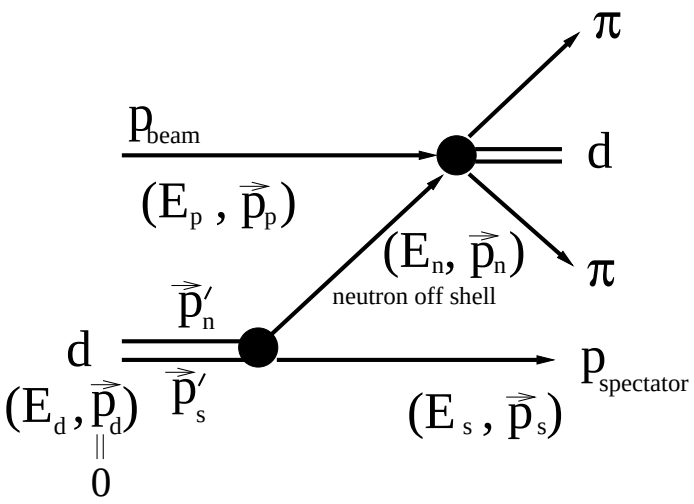

Figure 3.7: Schematic representation of the reaction $pd \rightarrow dp_s\pi^0\pi^0$ in the laboratory system. The process shows the spectator proton and the off shell neutron, which plays the role of the target in the rection $pn \rightarrow d\pi^0\pi^0$.

The simulation of the reaction $pn \rightarrow d\pi^0\pi^0$ was done in the following way. For each event θ, ϕ and p of the target were generated: a random $cos\theta$ in the interval [-1,+1], a random ϕ in the interval [0,2π] and a random momentum $|p|$ in the interval [0,0.4] GeV. The $cos\theta$ and ϕ distributions are homogeneous, the momentum distribution follows the Fermi momentum of the nucleons inside the deuteron.

From equation (3.7) we see that the effective neutron mass m_n decreases with increasing Fermi momenta. In Fig. 3.9 the 3-dimensional lego plot shows the correlation between the effective neutron mass versus the simulated Fermi momentum.

After identification of the three-momentum vector given by $|\vec{p}|$, $cos\theta$, ϕ and the effective mass of the target neutron the generation of the reaction and the further simulation were done according to the procedure described in Chaps. 3.1 and 3.2, respectively.

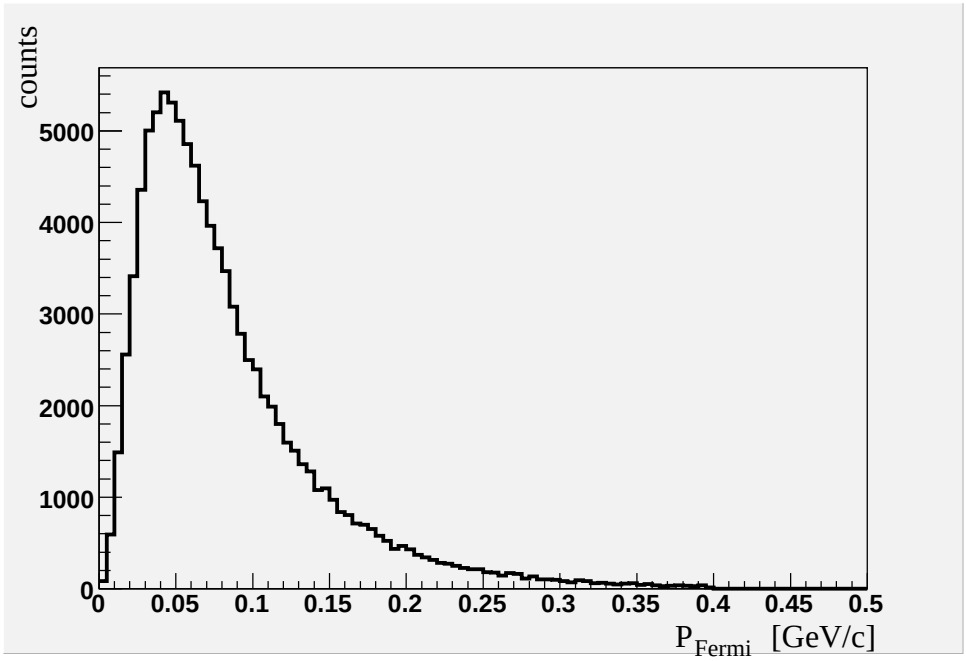

Figure 3.8: Distribution of the theoreticly calculated momentum of the nucleons inside the deuteron. The calculation was done according to the Hulthén wave function of the deuteron.

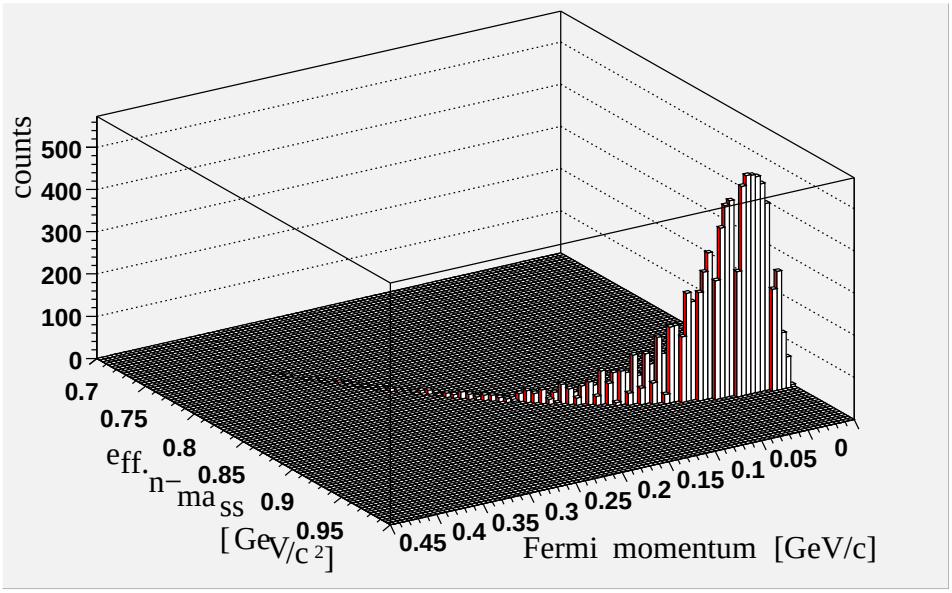

Figure 3.9: 3D lego plot of effective neutron mass m_n versus generated Fermi momentum for the reaction $pn \rightarrow d\pi^0\pi^0$ based on the Hulthén wave function.

Chapter 4

Analysis

The analysed data have been taken with a proton beam and a deuterium pellet target during beam times in 2004 and 2005. Table 4.1 gives a short overview of the mentioned beam periods.

Beam time	Run	Cycle [s]	Flat top [s]	Data taken [Gb]	Number of events [10^6]
June 2004 @1037	61-70	180	30-150	104	44
March 2005 @1360	120-137	180	50-150	127	48

Table 4.1 Summary of the analysed beam periods.

The actual beam energies were somewhat below the energies noted in the logbook. The main goal of the June 2004 beam time was to measure η right at threshold. The kinematical analysis of the η-production data resulted in an actual beam energy of $T_p = 1.03$ GeV (instead of 1.037 GeV) for the June 2004 run [Zło]. In March 2005 the actual beam energy was $T_p = 1.35$ GeV, since already in thesis of S. Häggström it was noted that the nominal energy of 1.36 GeV corresponds in reality to 1.35 GeV [Häg97].

4.1 Hardware trigger

To select the reaction of interest one needs appropriate conditions and constraints. This can be done on the hardware trigger level. The signals from *Forward* and *Central Detectors* are combined in the modules and if the trigger conditions are appropriate for the event, then the trigger fires and the event will be written on tape.

The main trigger, which was used in this analysis, is PT30. This is the so called energy trigger. It is based on a deposited energy sum threshold in the calorimeter, at least 2 neutral hits in SEC, one hit in Forward Hodoscope, one hit in the first FRH layer, and the veto condition on the PS to get rid of charged particles.

Trigger	Definition	Prescale Factor
PT30	ecf1*Vpsd*Pe2nfwd1ra1Vps	1
PT39	Pe2nfwd1ra1Vps = se2n*fhdw1*frha1*Vps	1

Table 4.2 Trigger summary for run periods June 2004 with $T_p = 1.03$ GeV and March 2005 at $T_p = 1.35$ GeV.

This trigger fulfills the desired conditions only for neutral channels. An attempt with a less restrictive trigger allowing for charged pion production failed because of heavy background: 3 000 $\pi^+\pi^-$ events were accompanied by 33 million background events.

In order to apply the acceptance correction one has to set exactly the same trigger conditions in the analysis of Monte Carlo data as in data taking. Therefore one has to simulate the trigger in Monte Carlo. To extract the threshold value for the energy sum trigger from the data the analog signals of all calorimeter crystals for the forward (SEF) and central (SEC) part are summed and plotted as 2-dimensional plot. Such a plot is shown in Fig. 4.1.

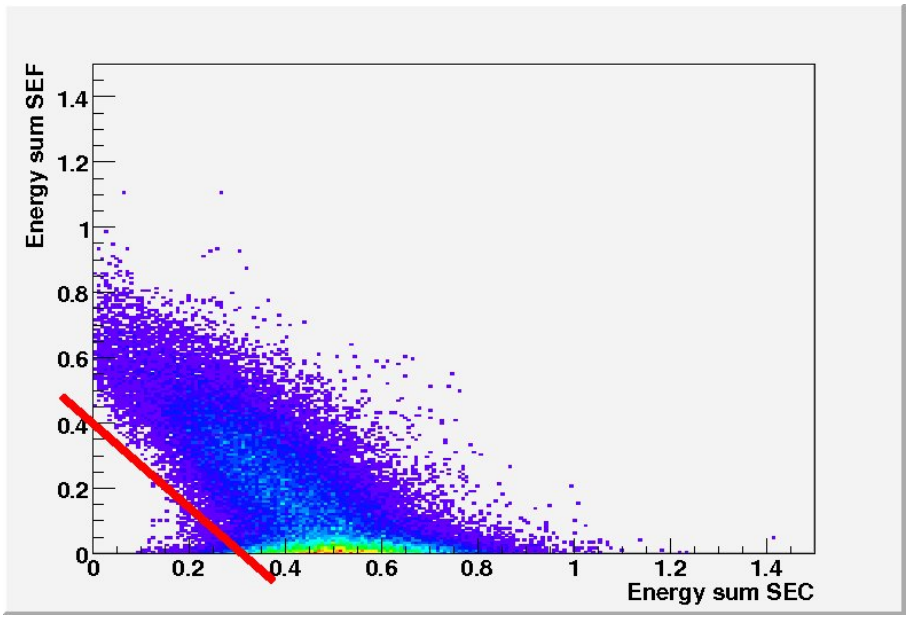

Figure 4.1: Deposited energy sum in the SEF versus SEC for experimental data taken with trigger PT30. The red line displays the software cut.

4.2 Selection cuts for the $pn \to d\pi^0\pi^0$ reaction

After the trigger selection we have to apply additional cuts in order to reduce the amount of background reactions. The summary of cuts, which were used for selection of the reaction $pn \to d\pi^0\pi^0$, are presented in Table 4.3.

applied cuts for $pn \to d\pi^0\pi^0$	
track in FD = 1	track in CD ≥ 4
$\Theta < 20^\circ$	$\Theta > 20^\circ$
$\phi > 180^\circ$	1970 < Time < 2200 [ns]
$0.2 < E_{kin} < 2.0$ [GeV]	$E_{kin} > 0.01$ [GeV]
Dep.E((FRH1)+(FRH2)+(FRH3)) > 0.1 + 0.6*Dep.E(FRH4) [GeV]	Dep.E(SEF) > 0.4 - 1.33*Dep.E(SEC) [GeV]
planarity cut $\Delta\phi_{\pi^0\pi^0-d} > 2.8$[rad]	
$MM^2_{d\pi^0\pi^0} \geq 1.42 - 0.6 \cdot M_{d\pi^0\pi^0}$ [GeV]	
$-0.3 \leq MM^2_{d\pi^0\pi^0} \leq 0.3$ [GeV]	

Table 4.3 Summary of cuts for the selection of the reaction $pn \to d\pi^0\pi^0$.

The main condition for selection of the reaction $pn \to d\pi^0\pi^0$ is the number of reconstructed particle tracks. We require 1 charged track in the *Forward Detector* (1FDC) and 4 neutral tracks in the *Central Detector* (4CDN). The next restriction for forward and central tracks affects the polar angle, for forward tracks $\theta < 20^\circ$ and for central tracks $\theta > 20^\circ$. The time window for central tracks is set to 1970 < Time < 2200 [ns]. The azimuthal angle for forward tracks was restricted to $\phi > 180^\circ$ due to the beam time conditions. Additionally cuts for kinetic energy were applied: for tracks in FD $0.2 < E_{kin} < 2.0$ GeV and for central tracks $E_{kin} > 0.01$ GeV respectively. For a further improved selection the cuts of deposited energy: in FD Dep.E((FRH1)+(FRH2)+(FRH3)) > 0.1 + 0.6*Dep.E(FRH4) and in CD Dep.E(SEF) > 0.4 - 1.33*Dep.E(SEC) were used. Finally the planarity cut $\Delta\phi_{\pi^0\pi^0-d} > 2.8$ rad and cuts on the invariant mass of the full system $M_{d\pi^0\pi^0}$ and on the missing mass $MM^2_{d\pi^0\pi^0}$ were applied.

As mentioned in Chap. 3.5 for the identification of particles $\Delta E/E$ plots have been used in the *Forward Detector*. According to kinematics the deuterons have kinetic energies up to 0.8 GeV at $T_p = 1.03$ GeV and up to 1.0 GeV at $T_p = 1.35$ GeV. That means that almost all deuterons punch through the *Forward Detector*. Therefore it is reasonable to look at the last layers of the FRH.

Fig. 4.2 shows the deposited energy in the third layer of the FRH versus its fourth layer. One can see two back-bent "bananas", which correspond to protons and deuterons, respectively. Additionaly after all energy corrections we make a kinematical cut $0.2 < E_d < 2.0$ GeV in order to reduce the protons from the background reaction $pn \to pn\pi^0\pi^0$.

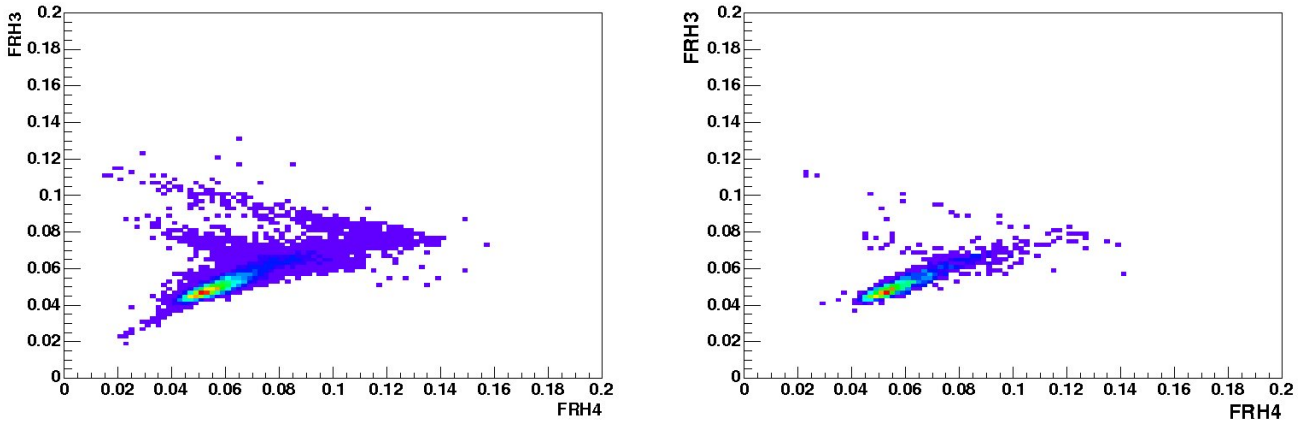

Figure 4.2: $\Delta E/E$ scatter plot for particles in the *Forward Detector*. The left plot with 1FDC requirement, the right plot with $\pi^0\pi^0$ pair selection and additional constraint of the particle with the identification number ID = 45 (deuterons). The left plot shows both back-bent "bananas" of protons and deuterons, whereas the right plot depicts mostly the deuteron "banana".

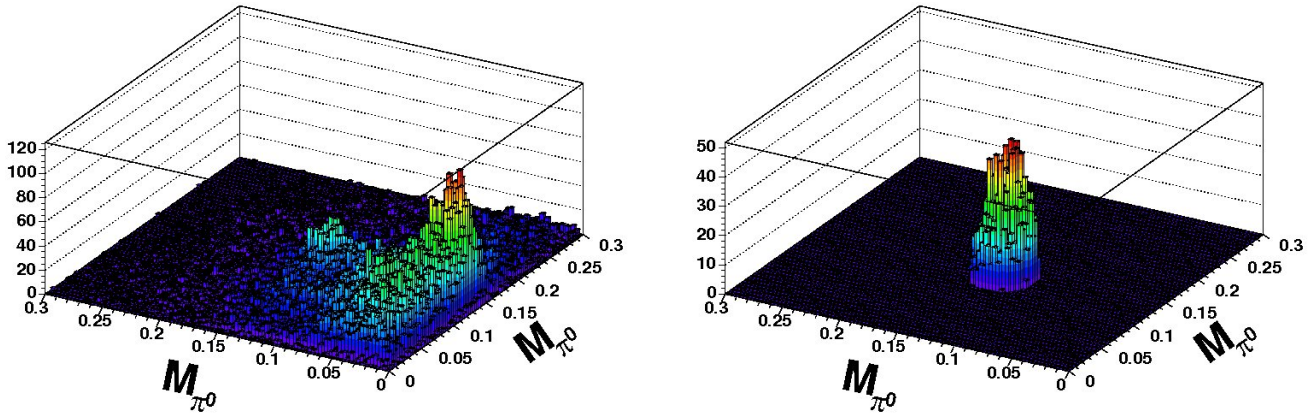

Figure 4.3: Invariant mass $M_{\pi^0{}_1}$ versus invariant mass $M_{\pi^0{}_2}$. The left plot contains all possible combination of π^0's, while the right spectra displays the best combination for the $pn \rightarrow \pi^0\pi^0$ reaction.

To check the correct forward track selection one can look at the missing mass of the rest system. Fig. 4.4 shows the missing mass of 4 photons. The first distribution depicts $MM_{\pi^0\pi^0}$ after selection of 1 forward charged track and four or more central neutral tracks. The second and third figures display the missing mass after additional cuts on $M_{\pi^0\pi^0}$ and planarity cut $\Delta\phi$, respectively. These restrictions make the distributions narrower at the cost of statistics, of course. The peak position is at 1.89 GeV and corresponds just to the mass of the deuteron.

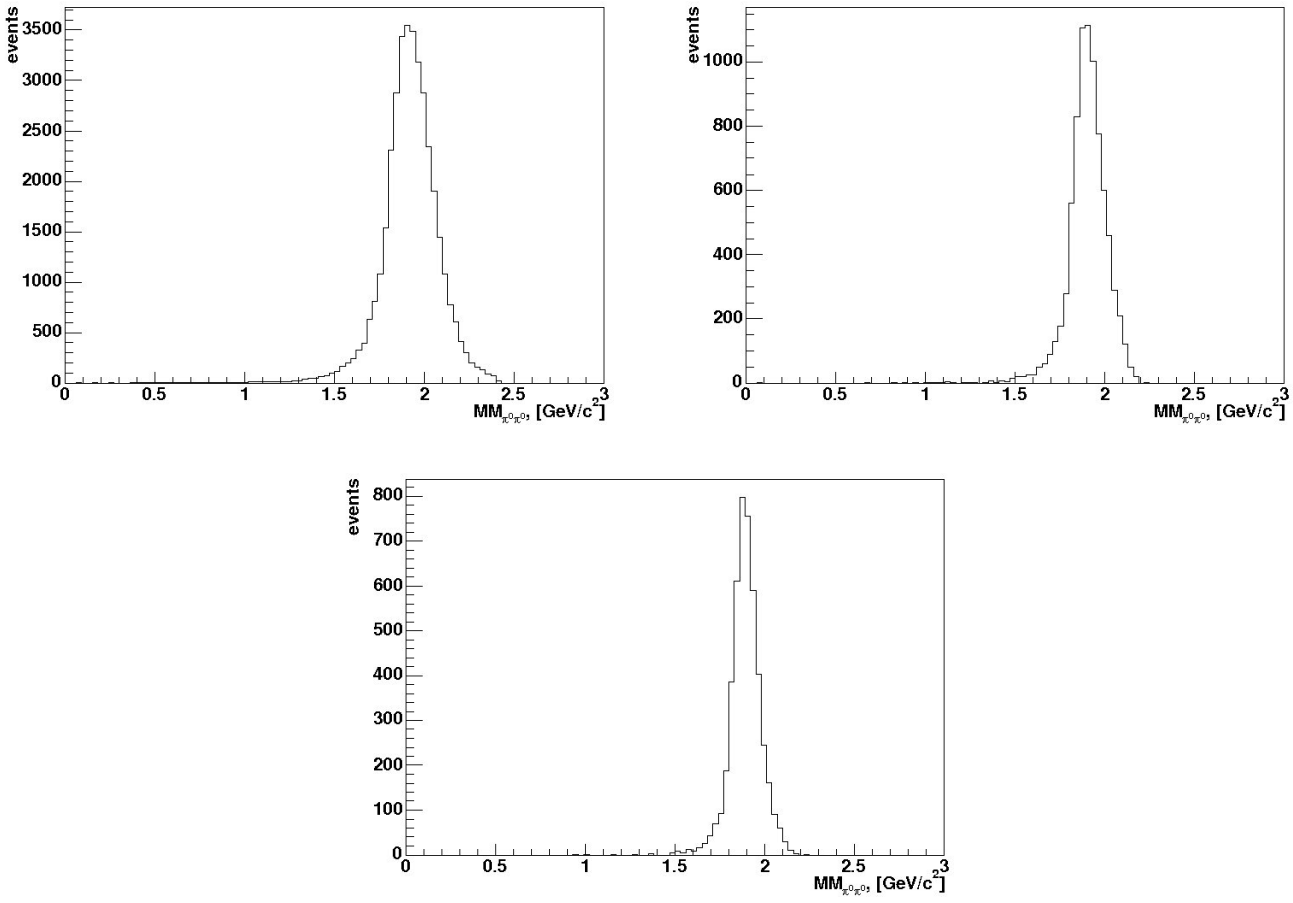

Figure 4.4: Missing mass of the two-pions system. The peak position corresponds to the mass of the deuteron. The first picture depicts the pion-pion missing mass after the requirement of the 1FDC and 4CDN tracks. The second figure shows the $MM_{\pi\pi}$ after the cut $(M_{\gamma_1\gamma_2} - M_{\pi^0})^2 + (M_{\gamma_3\gamma_4} - M_{\pi^0})^2 \leq 0.025$ on the invariant mass of two pions. The last histogram reproduce the $MM_{\pi\pi}$ after the additional planarity cut $\Delta\phi_{\pi\pi-d} > 2.8$ rad.

4.3 $\pi^0\pi^0$ selection

Since the lifetime of π^0 is only $10^{-17}s$ and since it decays into two gammas before it reaches the detector, one can detect only the decay particles, i.e. the photons.

In order to select 2 neutral pions one has to require four or more neutral tracks in CD and then combine it into two π^0.

Additional suppression of the background is achieved by using a time cut on the hits. The time window of selected hits in the *Central Detector* is about 230 ns. Fig. 4.5 shows the hit time in the calorimeter. The red curves shows the applied time cuts.

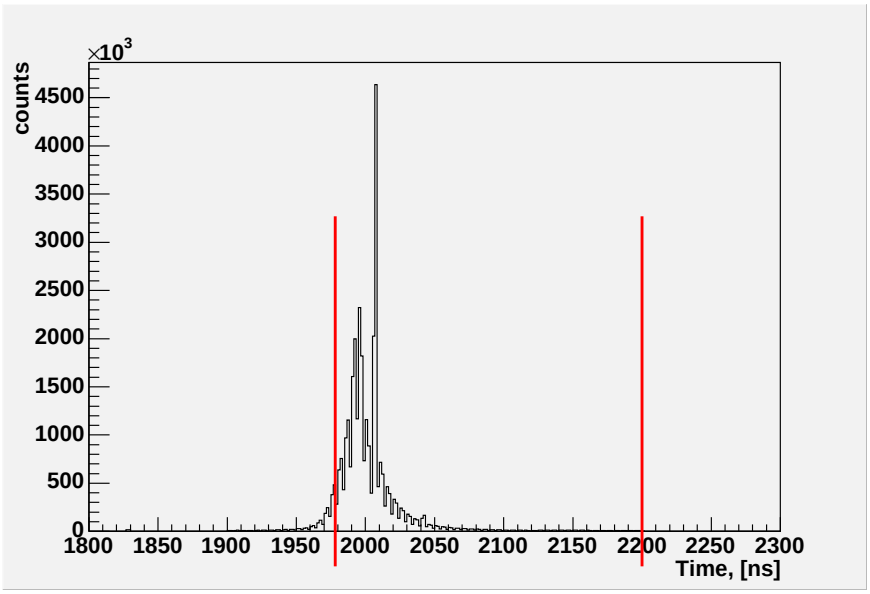

Figure 4.5: Time distribution of hits in the *Central Detector*. The red lines depict the applied time window.

The combination has been done in the following way. We have 3 possibilities to form 2 π^0 candidates out of 4 gammas.

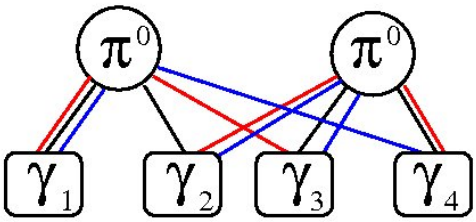

$M_{\pi_1^0}$	$M_{\pi_2^0}$
$\gamma_1\gamma_2$	$\gamma_3\gamma_4$
$\gamma_1\gamma_3$	$\gamma_2\gamma_4$
$\gamma_1\gamma_4$	$\gamma_2\gamma_3$

Figure 4.6: Photon combinatoric

Fig. 4.3 (left plot) displays the invariant mass of one π^0 versus the invariant mass of the second π^0.

Next a circular cut has been applied. We calculate the following expression for

all 3 combinations:

$$(M_{\gamma_1\gamma_2} - M_{\pi^0})^2 + (M_{\gamma_3\gamma_4} - M_{\pi^0})^2 = min \tag{4.1}$$

where $M_{\pi^0} = 0.135$ GeV.

To achieve the most probably combination and cleanly select $2\pi^0$ events we set: $min < 0.025$ GeV^2. The results is shown in Fig. 4.3 (right plot).

4.4 Other physical cuts for the analysed reaction

The reaction $pn \rightarrow d\pi^0\pi^0$ is a three body reaction. Nevertheless there is the possibility to apply a planarity cut. The $\pi^0\pi^0$-pair can be treated as one particle with momentum $\vec{p}_{\pi^0\pi^0} = \vec{p}_{\pi^0_1} + \vec{p}_{\pi^0 2}$. Fig. 4.7 shows the opening angle between deuteron and $\pi^0\pi^0$-pair versus the azimuthal angle. The result of the cut $\Delta\phi > 2.8$ rad i.e. 160° depicts Fig. 4.7 (right).

The additional requirement of one charged track in FD with particle ID = 45 (deuteron) also helps to reduce the background. As one can see from Fig. 4.2 (right) this additional condition cleans the $\Delta E/E$ spectrum.

Having now completely reconstructed events, there is still some background from other reactions in the selected events, coming mostly from three pion production $pn \rightarrow d\pi^0\pi^0\pi^0$. This is demonstrated in Fig. 4.8 (left), where the missing mass squared of the full system $MM^2_{d\pi^0\pi^0}$ is plotted versus the invariant mass $M_{d\pi^0\pi^0}$. In order to get rid of the disturbing events we apply the last cut with the following conditions: $MM^2_{d\pi^0\pi^0} \geq 1.42 - 0.6 \cdot M_{d\pi^0\pi^0}$ and $-0.3 \leq MM^2_{d\pi^0\pi^0} \leq 0.3$. The result is seen in Fig. 4.8 (right).

Since the measurements were performed using a deuteron target, the reaction to be analysed is in fact $pd \rightarrow dp_s\pi^0\pi^0$. Therefore after the selection of "good" events we can reconstuct the 4-momentum of the spectator proton using the conditions that energy and momentum are conserved.

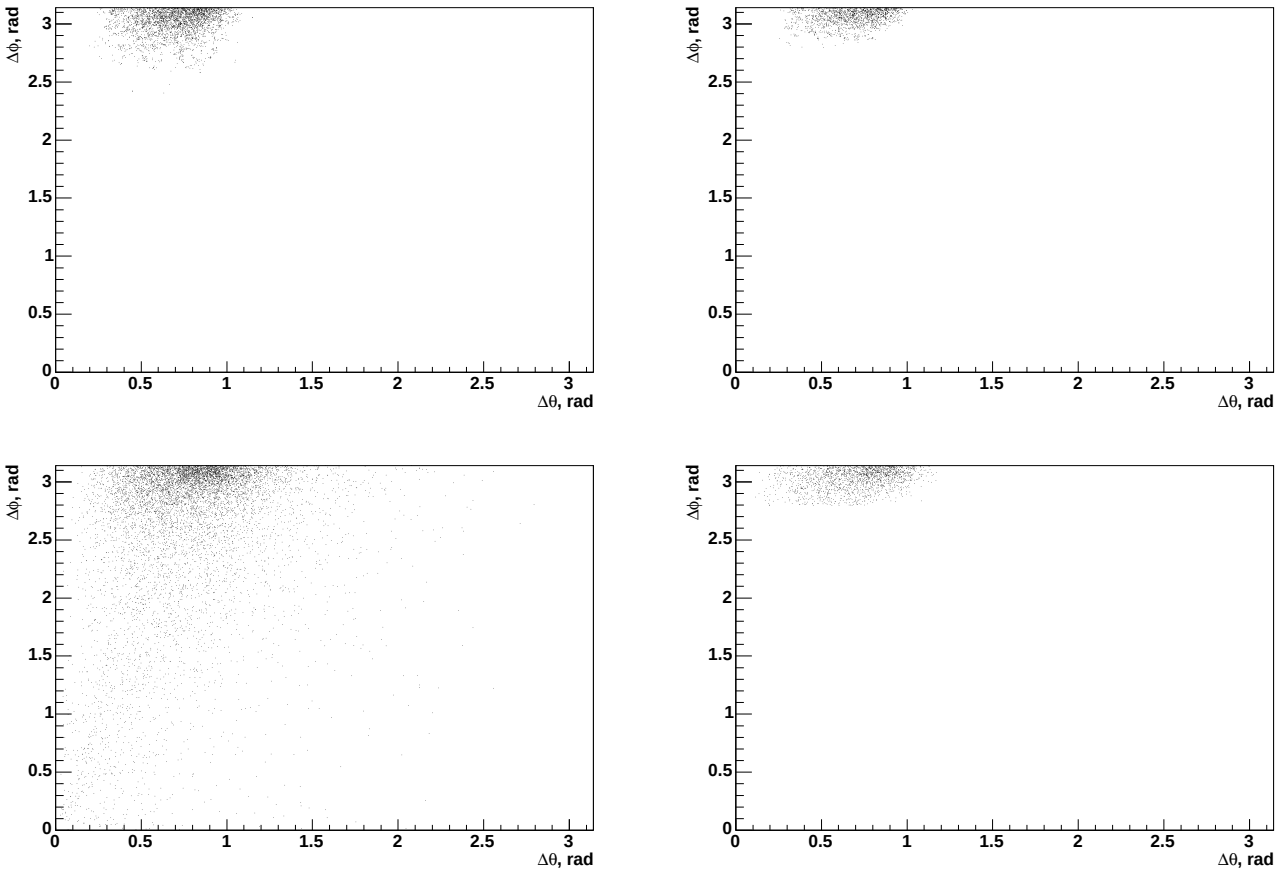

Figure 4.7: The azimuthal angle versus the opening angle between $\pi^0\pi^0$-pair and deuteron. The top row shows the MC simulated events, whereas the bottom row corresponds to the experimental data. The left histogram shows the situation before cut, while the right figure contains a cut condition $\Delta\phi > 2.8$ rad.

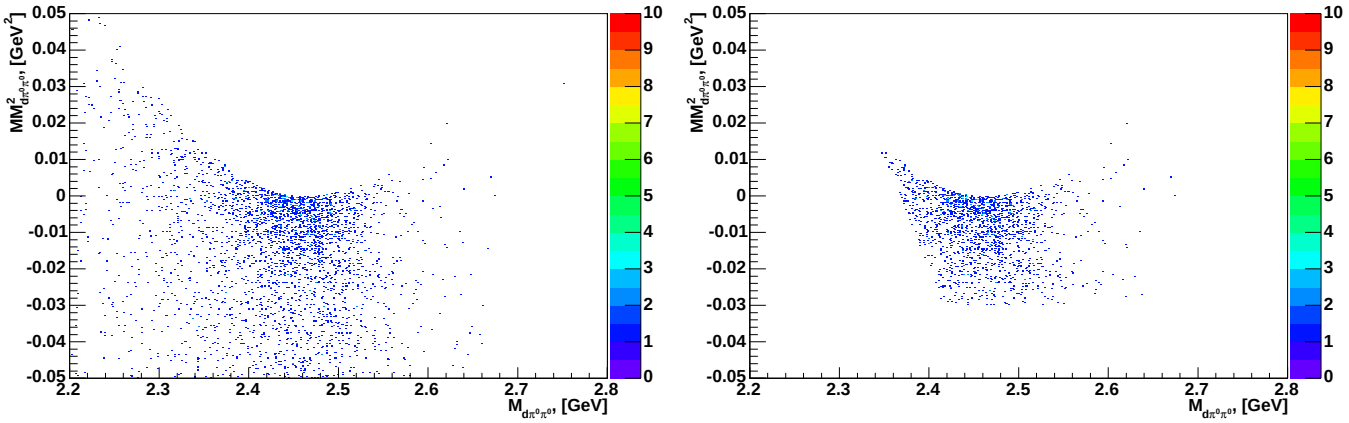

Figure 4.8: Missing mass squared $MM^2_{d\pi^0\pi^0}$ against the invariant mass $M_{d\pi^0\pi^0}$. Right plot shows the data after cut $MM^2_{d\pi^0\pi^0} \geq 1.42 - 0.6 \cdot M_{d\pi^0\pi^0}$ GeV and $-0.3\ GeV^2 \leq MM^2_{d\pi^0\pi^0} \leq 0.3$ GeV^2.

4.5 Reconstruction of the spectator-proton

Since we measured the quasi free reaction $pn \rightarrow d\pi^0\pi^0$ on the deuteron, the target neutron is not at rest, that means that due to Fermi motion the reconstructed relative momentum of the collision between proton beam and neutron target P_i is not a δ function distribution, but rather a distribution as one can see from Fig. 4.9.

Our aim is to analyse the full reaction $pd \rightarrow p_s d\pi^0\pi^0$. Therefore we assume that the proton in the deuteron is a spectator with very small momentum in the lab system, which influence the reaction only in the form of the Fermi motion of the bound neutron. Since we measured kinematically complete, we can reconstuct the spectator proton from energy and momentum conservation.

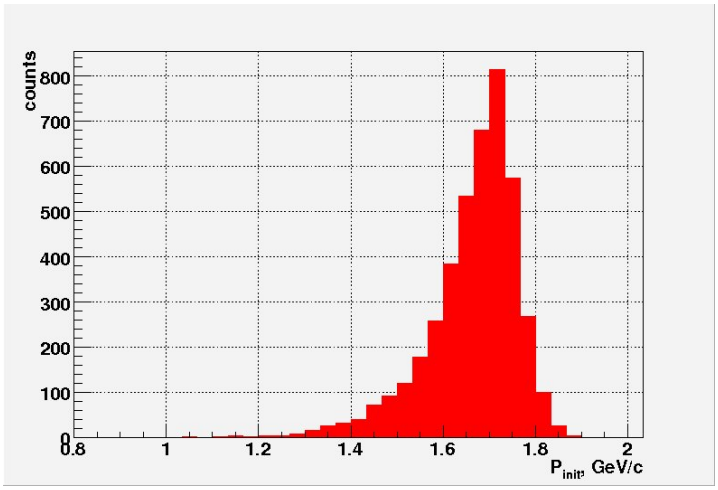

Figure 4.9: The momentum distribution of relative momentum of the collision between proton beam and neutron target in the reaction $pd \rightarrow p_s d\pi^0\pi^0$ at the beam energy $T_p = 1.03$GeV.

4.6 The kinematical fit - KFIT

Each experimental determination of the observables contains errors (uncertainties), which could lead to misidentification of the reaction of interest.

The kinematical fit is used for examination and improvement of values of measured variables by ensuring energy and momentum conservation for each event. The routine is using the method of Lagrangian multipliers. The WASA KFIT subroutine is written in FORTRAN language and uses CERNLIB subroutines.

The purpose of using a kinematical fit is to get rid of background reactions and to adjust the "good" events within defined errors intervals.

As input kinematical variables E_{kin}, θ, ϕ and m for each particle have been used. Each variable can be specified as measured, fixed or unmeasured. The incident

particles, i.e. beam and target, are always fixed. Additionally one can define a number of additional constraints.

In our case we have 6 particles in the outgoing channel: p, d and 4 $\gamma's$. For each particle 4 kinematical variables E_{kin}, θ, ϕ and m are available (altogether 24 variables). Since the proton spectator was not measured, but reconstructed, then only 20 variables were measured. But energy and momentum conservation yields four conditions. Hence the experiment is kinematically complete. Moreover we know the mass m_p of the proton spectator and we accept only events were the 4 γ's combine to two π^0 with known mass m_{π^0}. Therefore we end up with 3 overconstraints.

In order to fit the measured variables, which were measured with some uncertainties, we have to define expected errors. For the present reaction we used the following set of parameters:

- $\Delta E_d = |E_d| * 0.3$ [MeV]
- $\Delta\theta_d, \Delta\phi_d = 5^\circ$
- $\Delta E_{p_{spectator}} = |E_{p_{spectator}}| * 0.5$ [MeV]
- $\Delta\theta_{p_{spectator}}, \Delta\phi_{p_{spectator}} = 50^\circ$
- $\Delta E_{\gamma_1} = |E_{\gamma_1}| * 0.1$ [MeV]
- $\Delta\theta_{\gamma_1}, \Delta\phi_{\gamma_1} = 6^\circ$
- $\Delta E_{\gamma_2} = |E_{\gamma_2}| * 0.2$ [MeV]
- $\Delta\theta_{\gamma_2}, \Delta\phi_{\gamma_2} = 5^\circ$

As output of KFIT we get fitted values for each kinematical variable and χ^2-value. The χ^2 is given by:

$$\chi^2 = \sum_{k=1}^{N} \left[\frac{(f_f)^k - (f_{in})^k}{\Delta(f)^k} \right]^2 \tag{4.2}$$

where N is the number of events, $(f_{in})^k$ is the value of the observable before KFIT, $(f_f)^k$ is the value of the observable after KFIT and $\Delta(f)^k$ is the assumed error of this observable.

The best possible fit is when $\chi^2 \approx n$, where n is the number of effective degrees of freedom, provided that $\Delta(f)^k$ is chosen realistically. Since the measurements are always random processes and the results contain the uncertainties, the χ^2 distributions becomes broader. Fig. 4.10 shows an example of the χ^2 distribution.

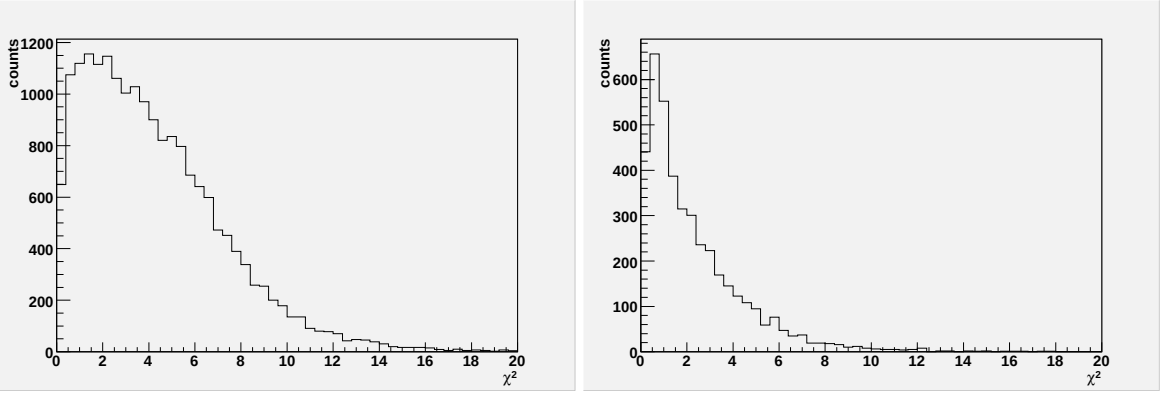

Figure 4.10: χ^2 distribution for the reaction $pn \rightarrow d\pi^0\pi^0$. The left plot shows the χ^2 for $T_p = 1.03$ GeV. The right histogram depicts the χ^2 for $T_p = 1.35$GeV.

We would like to have the χ^2 in a reasonable range, therefore we require $\chi^2 < 20$ for data at $T_p = 1.03$ GeV and $\chi^2 < 6.2$ for data at $T_p = 1.35$ GeV. This reduces the number of events from 4863 events to 4257 (13 % loss) events for $T_p = 1.03$ GeV and from 1815 events to 1633 (10 % loss) events for $T_p = 1.35$ GeV.

The same kinematical fit method with the same conditions has been applied to the Monte-Carlo simulated data.

4.7 Efficiency and Acceptance Corrections

At the end of the analysis the experimental data have been corrected using Monte-Carlo simulations. Since the probability of particle detection in a real detector is smaller than 100% and the solid angle is restricted by the detector design, we have to consider and correct it. The correction has been done in the way outlined in the histogram (see Fig. 4.11).

In order to apply the efficiency and acceptance corrections to the experimental data for each observable one needs 3 histograms:

- the first is for the model results without constraints by the detector; this is produced by the event generator
- the second is for the model results after event tracking through the detector and subsequent event analysis
- the third is for the analyzed experimental data

In order to correct an experimental histogram one has to multiply the histogram with experimental data by the quotient of the histogram for the simulated data including detector response and the histogram for the model without detector response. It is obvious that the result depends on the assumed reaction model.

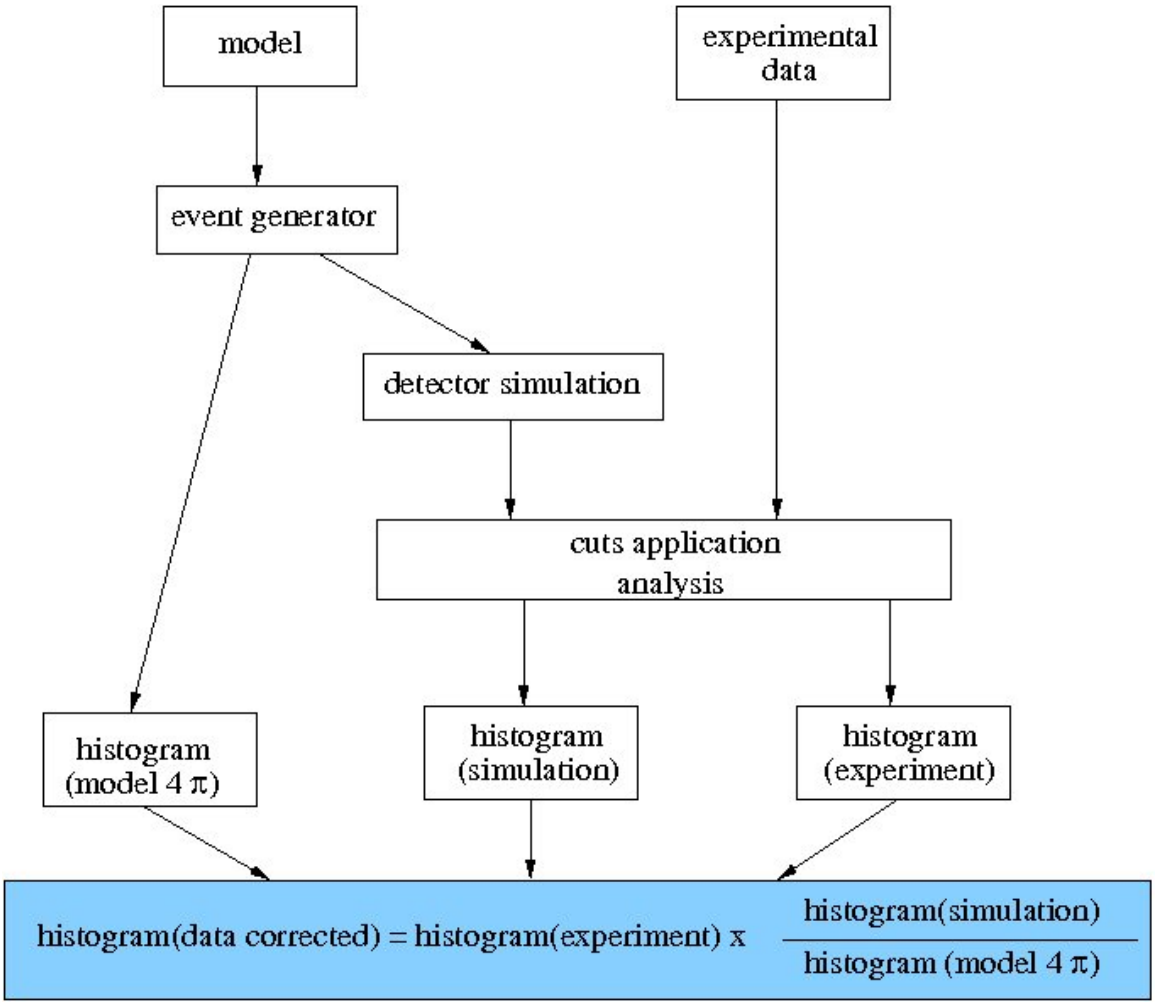

Figure 4.11: Scheme of efficiency and acceptance corrections. The correction function is calculated from the simulated histograms and then applied to the histogram of the experimental data.

The next two figures demonstrate the effect and model dependence of the correction method for two observables at $T_p = 1.03$ GeV. The first example shown in Fig. 4.12 is the invariant mass of two pions $M_{\pi^0\pi^0}$. The yellow area is the pure phase space, the black solid line corresponds to model calculation (see Chap. 5.4.3), which shows good agreement with the data. Despite the significant difference between the two models, the acceptance and efficiency corrected data display nearly the same result (see the right top histogram in Fig. 4.12). The ratio between two model corrections shows only some deviation from unity at low invariant masses.

The second example shown in Fig. 4.13 demonstrates the effect of the correction method of the pion polar angle $\theta_{\pi^0}^{d\pi^0}$ in the $d\pi^0$ subsystem. Here the model calculations before the detector simulation depict significant differences. But the situation changes after Monte Carlo simulation; here the distributions (middle picture in Fig. 4.13 in the first column) show nearly the same behavior.

Of course, for consistency reasons, only a model, which is in reasonable agree-

ment with the final results, gives reliable corrections.

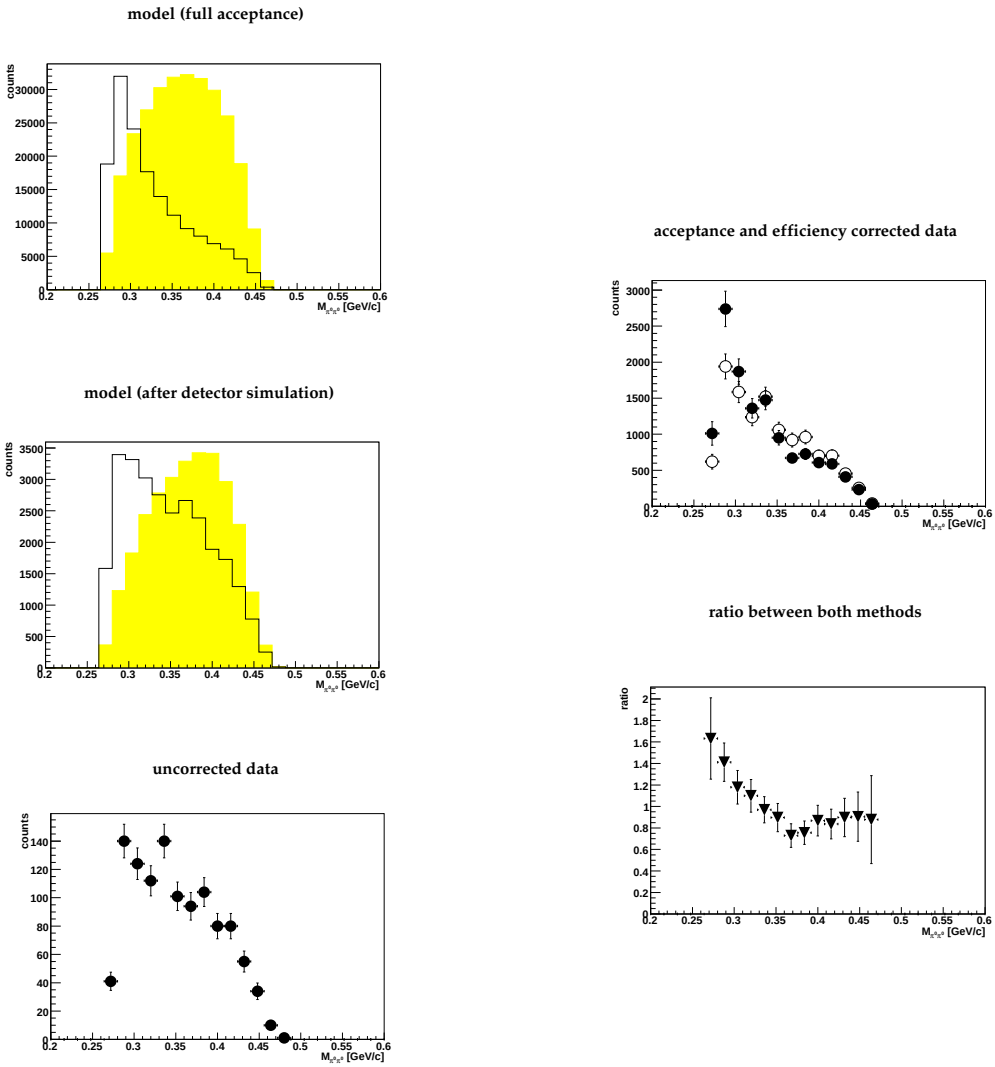

Figure 4.12: Acceptance and efficiency corrections for the invariant mass of two pions $M_{\pi^0\pi^0}$. Two different models were used. The yellow area is pure phase space, the black solid line depicts the model calculation presented in Chap. 5.4.3. The left column shows from the top to bottom: the generated model for the full 4π acceptance, the next is the histogram after detector simulation and analysis and finally the spectrum of uncorrected experimental data. On the right the top histogram shows the acceptance and efficiency corrected experimental data using corrections of both models (the black points corresponds to the model correction, while the open points to the phase space correction). The bottom figure shows the ratio between the both methods.

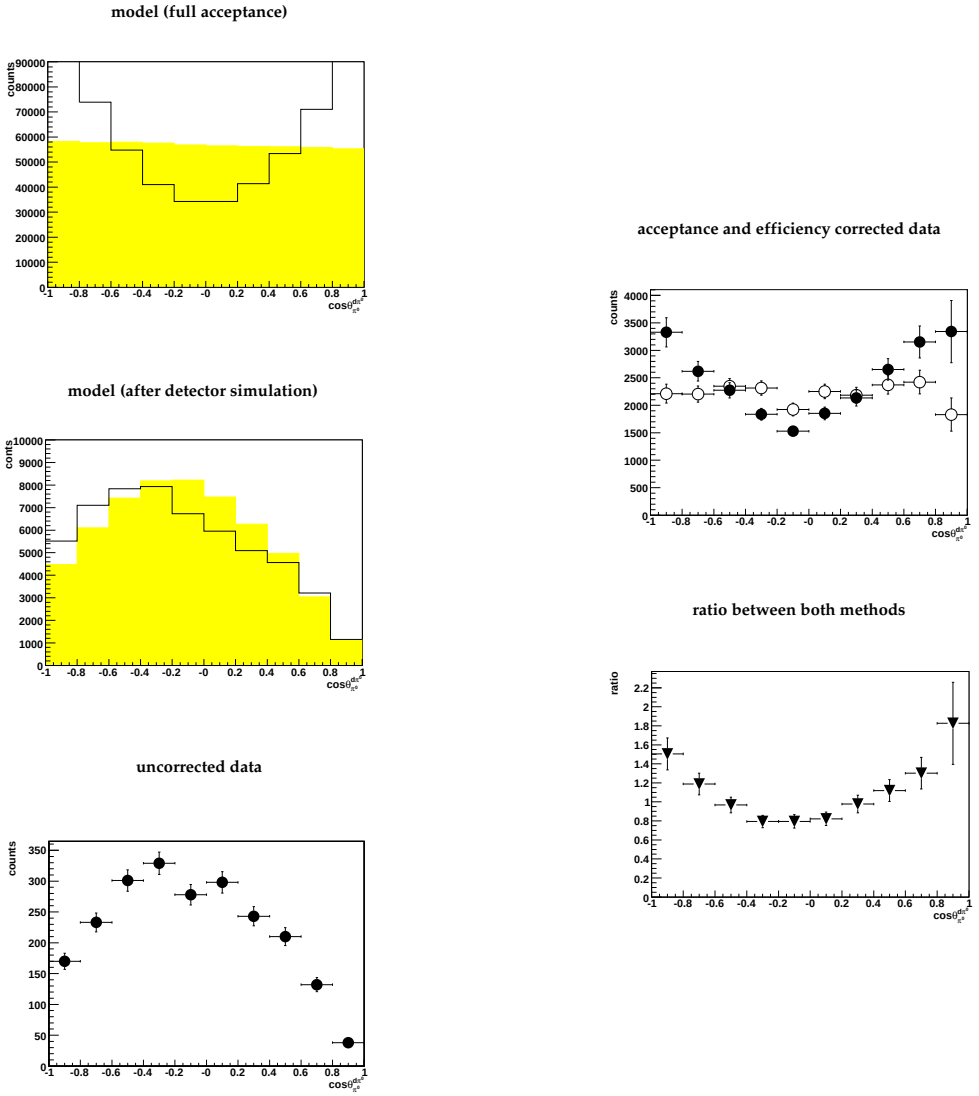

Figure 4.13: Acceptance and efficiency correction for the theta angle of pions $\theta_{\pi^0}^{d\pi^0}$ in $d\pi^0$ subsystem. Two different models were used. The yellow area is pure phase space, the black solid line depicts the model calculation presented in Chap. 5.4.3. The left column shows from the top to bottom: the generated model for the full 4π acceptance, the next is the histogram after the detector simulation and analysis and finally the spectrum from uncorrected experimental data. On the right the top histogram shows the acceptance and efficiency corrected experimental data using corrections of both models (the black points corresponds to the model correction, while the open points to the phase space correction). The bottom figure shows the ratio between the both methods.

Chapter 5

Results and Discussion

In this chapter the results of the analysis of the two pion production reaction $pn \rightarrow d\pi^0\pi^0$ at the two energies 1.03 and 1.35 GeV will be presented. The normalisation will be performed and the total cross section is determined. The experimental data will be compared to several theoretical models. A possible reaction mechanism for the description of the data will be discussed. The differential spectra for the raw (uncorrected) data can be found in Appendix B.

5.1 Normalisation and total cross section

In order to determine the total cross section for the reaction $pn \rightarrow d\pi^0\pi^0$ the analyzed data are normalised relative to a reaction with a well-known cross section. We used two possibilities: the first is to normalize with the quasi-free single pion production $pn \rightarrow d\pi^0$, and the second possiblity is to use the reaction $pn \rightarrow d\eta$. We tried both normalisation methods and achieved agreement within 10% for both methods.

The cross section is given by:

$$\sigma_{reaction} = \frac{N_{ex} \cdot f_{prescal}}{\int Ldt \cdot \epsilon_{DAQ} \cdot \epsilon_{acc}} \tag{5.1}$$

where N_{ex} is the number of measured events; $f_{prescal}$ is the trigger prescaling factor; $\int Ldt$ is the time integrated luminosity; ϵ_{DAQ} describes the data acquisition life time in percent and ϵ_{acc} is an acceptance correction factor.

In order to obtain an absolute normalisation according to this formula, we have to determine the integrated luminosity, the data acquisition life time and other parameters. We have to take into account all possible disturbances during the beam time, e.g. time without beam or target (accelerator duty factor), real data acquisition life time, etc. All this makes the normalisation complicated.

Therefore we chose a simple way to determine the total cross section by normalizing the two pion production relative to a single quasifree pion production $pn \to d\pi^0$.
The advantages of this method are:

- same beam time
- same trigger PT30
- same DAQ life time

The ratio of acceptance and efficiency corrected events for double and single pion production is equal to the ratio of their total cross sections:

$$\frac{N_{corr}(pn \to d\pi^0\pi^0)}{N_{corr}(pn \to d\pi^0)} = \frac{\sigma(pn \to d\pi^0\pi^0)}{\sigma(pn \to d\pi^0)} \tag{5.2}$$

where N_{corr} is the number of acceptance and efficiency corrected events.

Assuming isospin conservation the cross section for the single π^0 production has been obtained from π^+ production via the isospin relation:

$$\sigma(pp \to d\pi^+) = 2 \cdot \sigma(pn \to d\pi^0) \tag{5.3}$$

Fig. 5.1 shows the deuteron angular distribution in the $d\pi^0$ system for the reaction $pn \to d\pi^0$. The total cross section has been obtained by comparison of the experimental data (black dots) and the SAID prediction [SAID] (dashed line) for the $pp \to d\pi^+$ reaction.

As a result we obtain an absolute cross section of the $pn \to d\pi^0\pi^0$ reaction of 126 μb at $T_p = 1.03$ GeV and of 230 μb at $T_p = 1.35$ GeV. The value for the lower energy is in good agreement with the Dubna value [Abd79] for the $pn \to d\pi^+\pi^-$ cross section, which should be twice as large as in the $\pi^0\pi^0$ case due to the isospin relation for the isoscalar case, see Chap. 5.4.2. For the higher energy there are no data to directly compare with.

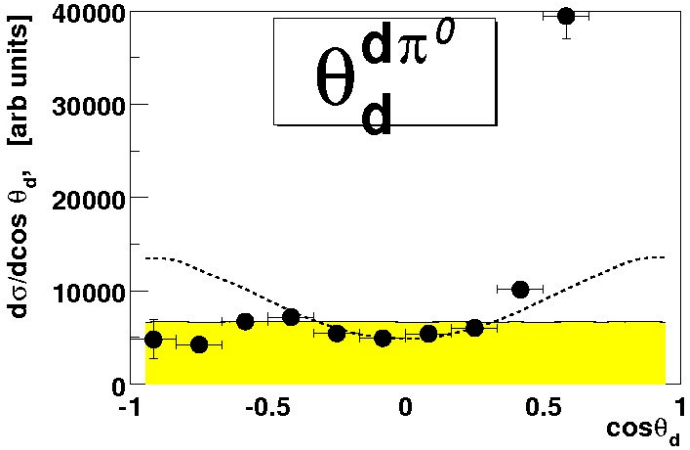

Figure 5.1: The deuteron angular distribution in $d\pi^0$ system for the reaction $pn \rightarrow d\pi^0$ at $T_p = 1.35$ GeV. The yellow area is the phase space, the dotted line represents the SAID prediction [SAID] and the black points are our data.

5.1.1 Summary of Errors

Statistical Errors

The random or statistical errors may occur from instrumental inaccuracy and from the statistical fluctuation of the phenomena which has been observed during the measurement.

The statistical percentage errors are given by:

$$\delta_N = \frac{1}{\sqrt{(N_{exp})}} \tag{5.4}$$

Since the number of the analysed events for $pn \rightarrow d\pi^0\pi^0$ at $T_p = 1.03$ GeV are 4257 and 1633 at $T_p = 1.35$ GeV, the statistical errors for the total cross sections were in the order of 1.5 to 2.5 % and are almost negligible.

Systematic Errors

The main source of the uncertainty in our experiment is due to systematic errors. The systematic errors are most important when groups of data points were collected under the same conditions. In each experiment the systematic uncertainty has to be considered individually.

In our experiment the following systematic errors have been taken into account:

- the estimated uncertainty of the beam energy is $\delta_{beam} \approx 0.8$ %. This energy shift has to be taken into account in the Monte Carlo simulation

- as shown in Chap. 4.7, corrections of data for efficiency and acceptance are model dependent. The difference between the pure phase space and model calculations (see Chaps. 5.4.1,5.4.3) leads to an upper limit of systematic errors $\delta_{cor} \approx 20$ %
- the contributions from background reactions are expected to be tiny. Additionally, the application of several physical cuts and kinematical fit (KFIT) has removed most background events

Since all discussed errors were assumed to be uncorrelated, they were summed up quadratically:

$$\delta_{tot} = \sqrt{\delta_N^2 + \delta_{beam}^2 + \delta_{cor}^2} \tag{5.5}$$

For the data at both beam energies $T_p = 1.03$ GeV and $T_p = 1.35$ GeV the errors result in $\delta_{tot} \approx 20$ %.

Table 5.1 gives a summarized overview of the obtained values for total cross section and estimated errors.

Beam time	1.03 GeV	1.35 GeV
$\sigma_{d\pi^0}[\mu b]$	200	100
$N_{d\pi^0}$	$1.15 \cdot 10^5$	$5.0 \cdot 10^4$
$N_{d\pi^0\pi^0}$	$7.27 \cdot 10^4$	$2.7 \cdot 10^5$
$\sigma_{d\pi^0\pi^0}[\mu b]$	126	230
total errors [%]	20.1	20.2

Table 5.1 Summary of total cross sections and errors.

5.2 Differential cross sections

In the following section the distributions of the differential cross section for several observables at $T_p = 1.03$ GeV and at $T_p = 1.35$ GeV will be presented. The efficiency and acceptance corrected data will be compared to different models: phase space, which is represented by the yellow filled area, a $\Delta\Delta$ calculation without the assumption of a bound $\Delta\Delta$ (blue dotted curves) and a $\Delta\Delta$ calculation with assumption of a s-channel resonance (red solid curves).

5.2.1 Definition and calculation of observables

Scattering angles, planarity and opening angles

Usually the spherical coordinate system for representing objects in three dimensions with three coordinates (r, θ, ϕ) is used. The polar angle θ is the scattering angle between the z-axis, which corresponds to the beam direction and the particle track with momentum $\mathbf{p} = (p_x, p_y, p_z)$. It is defined as:

$$\theta = arctan\frac{\sqrt{p_x^2 + p_y^2}}{p_z}; \qquad [0, \pi] \tag{5.6}$$

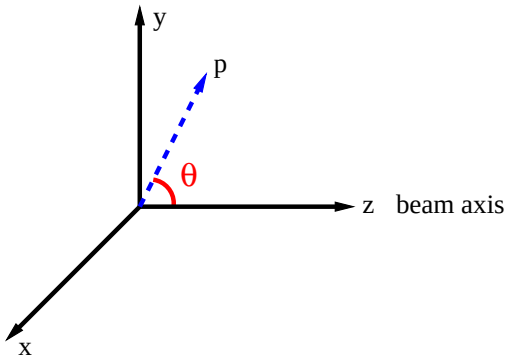

ϕ is referred to as the azimuthal angle and measured between the x-axis and the projection of the particle track onto the xy-plane:

$$\phi = arctan\frac{p_y}{p_x}; \qquad [0, 2\pi] \tag{5.7}$$

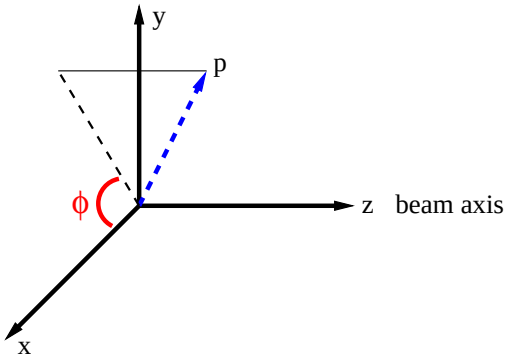

The planarity angle $\Delta\phi$ is calculated as the difference in ϕ for two particle tracks and is given by:

$$\Delta\phi = acos\frac{p_{1_x}p_{2_x} + p_{1_y}p_{2_y}}{\sqrt{p_{1_x}^2 + p_{1_y}^2} \cdot \sqrt{p_{2_x}^2 + p_{2_y}^2}} \tag{5.8}$$

The opening angle δ between two particles is calculated according to:

$$\delta_{12} = acos\frac{\mathbf{p_1} \cdot \mathbf{p_2}}{|\mathbf{p_1}||\mathbf{p_2}|} \tag{5.9}$$

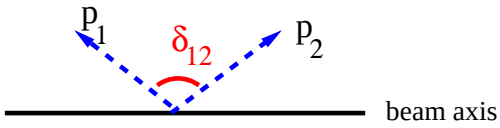

Subsystem scattering angles

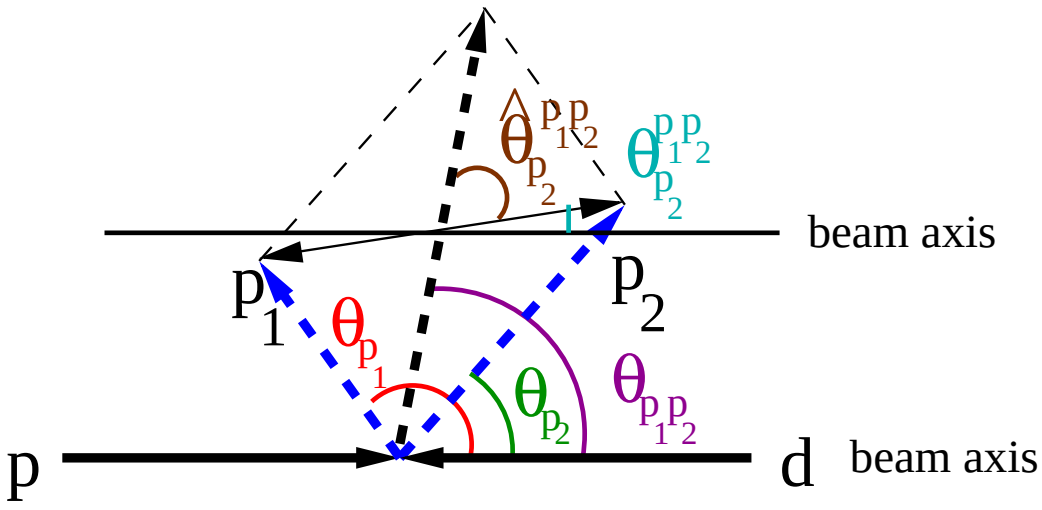

Figure 5.2: Definition of different scattering angles in the subsystem of particles, here for two particles p1 and p2. The sketch shows a non-relativistic construction.

Fig. 5.2 shows the definition of the different scattering angles in the subsystem of particles. As example two particles are treated: p_1 and p_2. θ_{p_1} and θ_{p_2} are the scattering angles in the overall centre of mass system. $\theta_{p_1p_2}$ is the scattering angle of both particles p_1 and p_2 (sum vector) in the overall centre of mass system. $\theta_{p_2}^{p_1p_2}$ is defined as scattering angle of particle p_2 in the rest frame of p_1 and p_2 with respect to the beam axis. This system is often also called Jackson frame. $\hat{\theta}_{p_2}^{p_1p_2}$ is the scattering angle of particle p_2 in the rest frame of p_1 and p_2 with respect to the sum vector of the particles (helicity frame).

Missing mass

If of N particles in the exit channel only (N-1) are identified, the missing mass of the not-measured particle can be calculated based on energy and momentum conservation. The missing mass is calculated according to the equation:

$$MM = \sqrt{\left(m_t + \frac{E_b}{c^2} - \sum \frac{E_i}{c^2}\right)^2 - \left(\frac{\mathbf{p_b}}{c} - \sum \frac{\mathbf{p_i}}{c}\right)^2} \tag{5.10}$$

where t and b refer to the target and the beam, respectively.

5.2.2 Invariant masses

The invariant mass is Lorentz invariant. Therefore it should be the same in all coordinate systems. The invariant mass of a system is given by:

$$M^2c^4 = \left(\sum_i E_i\right)^2 - \left(\sum_i p_i\right)^2 c^2 \tag{5.11}$$

where E_i and p_i are energy and momentum of particle i.

In case of the reaction $pn \rightarrow d\pi^0\pi^0$ there are only two invariant mass distributions, since the two neutral pions are identical. The most elegant way to represent the invariant mass situation in case of a 3-body system is the socalled Dalitz-plot, a 2-dimensional plot of M^2_{xy} versus M^2_{yz} or M^2_{xz}. In case of a pure phase space distribution these Dalitz-plots are completely flat. For our reaction such Dalitz-plots are shown in Figs. 5.3 and 5.4. We see that these plots are far from being flat, i.e., far from being phase-space-like. They rather exhibit very pronounced enhancements in the region of the Δ resonance and at the low-mass kinematic limit of $M^2_{\pi^0\pi^0}$. This unusual phenomenon is known as the ABC effect. In the reaction $pn \rightarrow d\pi^0\pi^0$ the $\pi^0\pi^0$ channel is free of both isovector ($I = 1$) and isotensor ($I = 2$) contributions due to vanishing isospin coupling coefficients. Hence observation of the ABC effect here means that it must be of isoscalar ($I = 0$) character. Figs. 5.5 and 5.6 depict the Dalitz-plot projections, the spectra of invariant mass $M_{\pi^0\pi^0}$ and $M_{d\pi^0}$ for $T_p = 1.03$ GeV and $T_p = 1.35$ GeV, respectively. At both energies, low-mass $M_{\pi^0\pi^0}$ enhancement and Δ excitation, respectively, are the predominating structures.

Due to the trigger conditions we did not measure the channel with charged pions $\pi^+\pi^-$, where we could observe the two Δ's separately. However, the reaction $pd \rightarrow^3 He\pi^+\pi^-$, which also has been measured at WASA, shows this case [Bash06a].

The data are compared to the phase space and to the several calculations. The reaction mechanisms and their explanation by theoretical models will be discussed in Chap. 5.4.

To avoid the long tails due to Fermi motion, which appears as a long tail at high masses in the invariant mass distributions, we chose for the analysis an effective energy range between 1.00-1.03 GeV for the run at beam energy $T_p = 1.03$ GeV and 1.34-1.37 GeV for the run at beam energy $T_p = 1.35$ GeV, respectively. Figs. 5.7 and 5.8 depict the spectra of invariant masses within this energy region.

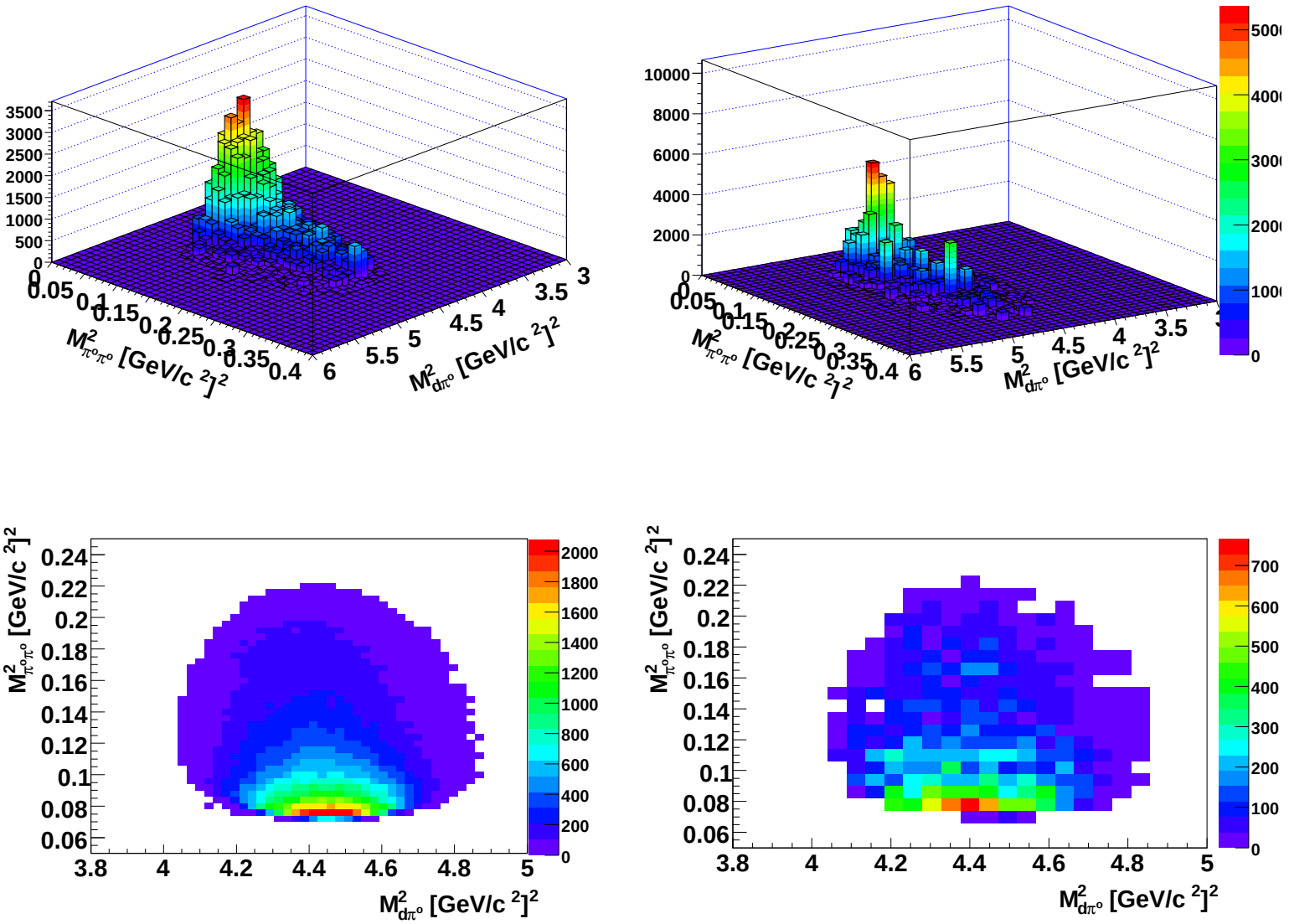

Figure 5.3: Dalitz plot of the invariant mass distributions of the quasifree reaction $pn \rightarrow d\pi^0\pi^0$ in the range 1.00-1.03 GeV of effective collision energies. Left: MC generated events, right: data; top: Lego plot (3D representation), bottom: scatterplot (2D representation).

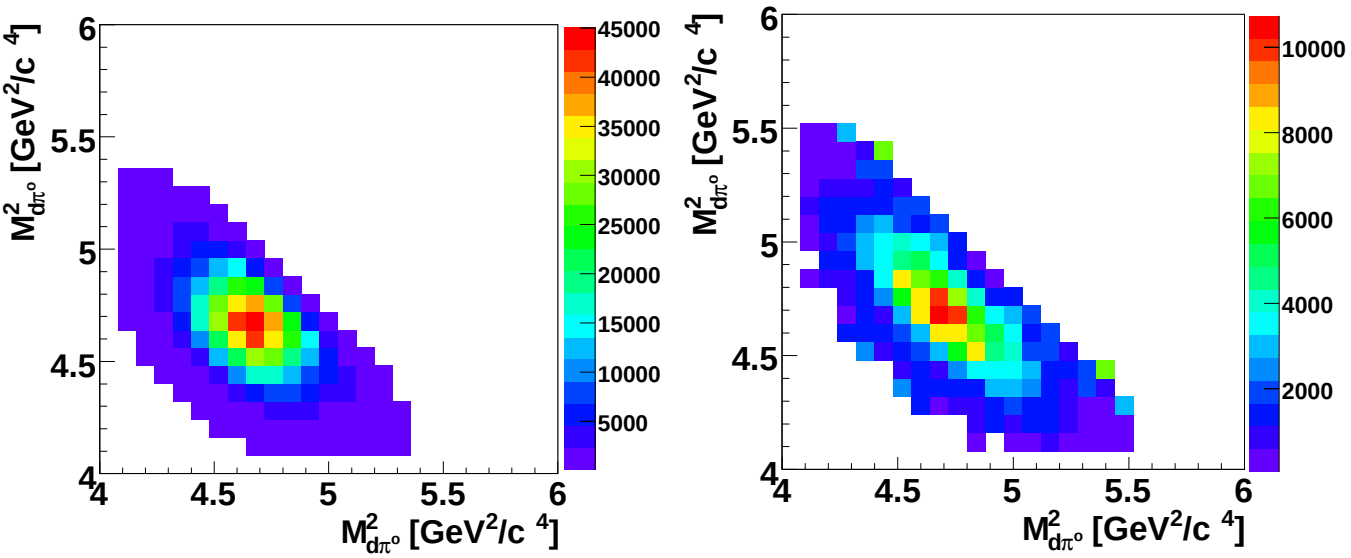

Figure 5.4: Dalitz plot of the invariant mass distributions for $M^2_{d\pi^0}$ versus $M^2_{d\pi^0}$ for the quasifree reaction $pn \rightarrow d\pi^0\pi^0$ in the range 1.27-1.37 GeV of effective collision energies. Left: MC generated events; right: data.

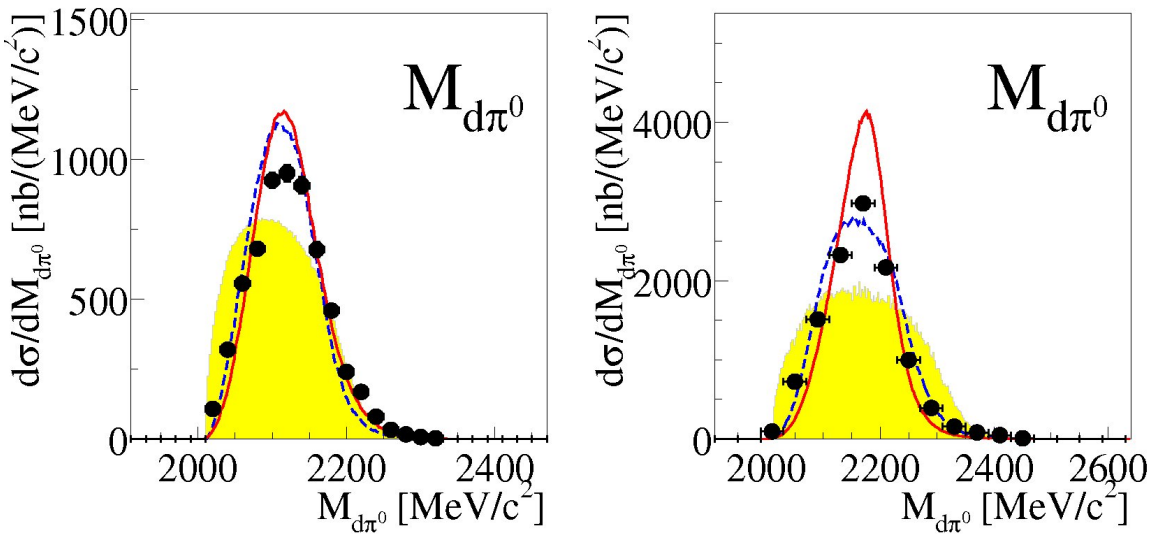

Figure 5.5: Invariant mass distributions of $M_{d\pi^0}$ at $T_p = 1.03$ GeV (left) and $T_p = 1.35$ GeV (right). The dashed areas show pure phase-space distributions. Solid and dotted curves give $\Delta\Delta$ calculations with and without the assumption of an s-channel resonance, respectively. All curves are normalized to the experimental integral cross section.

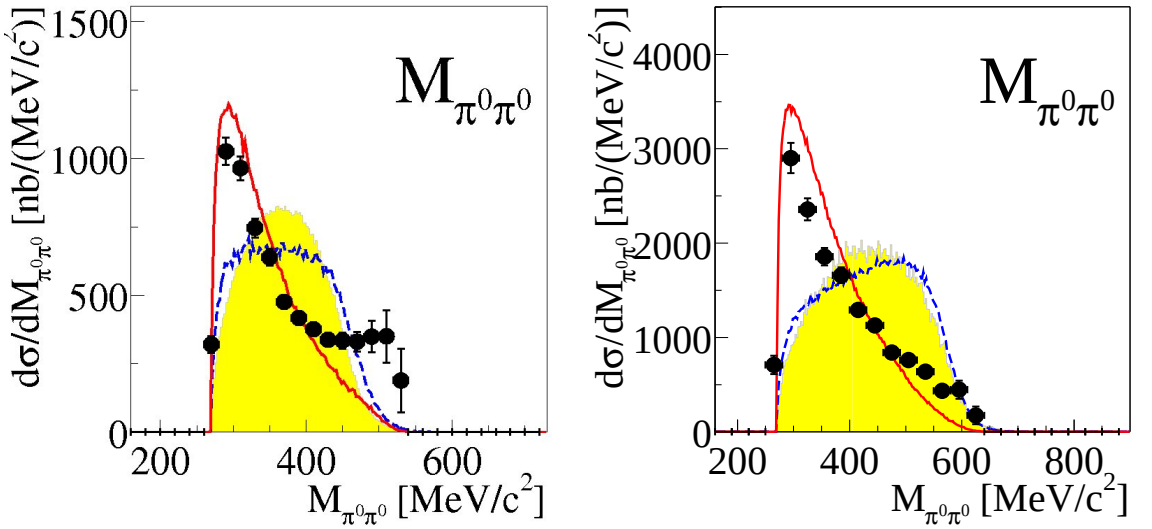

Figure 5.6: Distributions of the invariant masses $M_{\pi^0\pi^0}$ at $T_p = 1.03$ GeV (left) and $T_p = 1.35$ GeV (right). For the meaning of curves and symbols see Fig. 5.5.

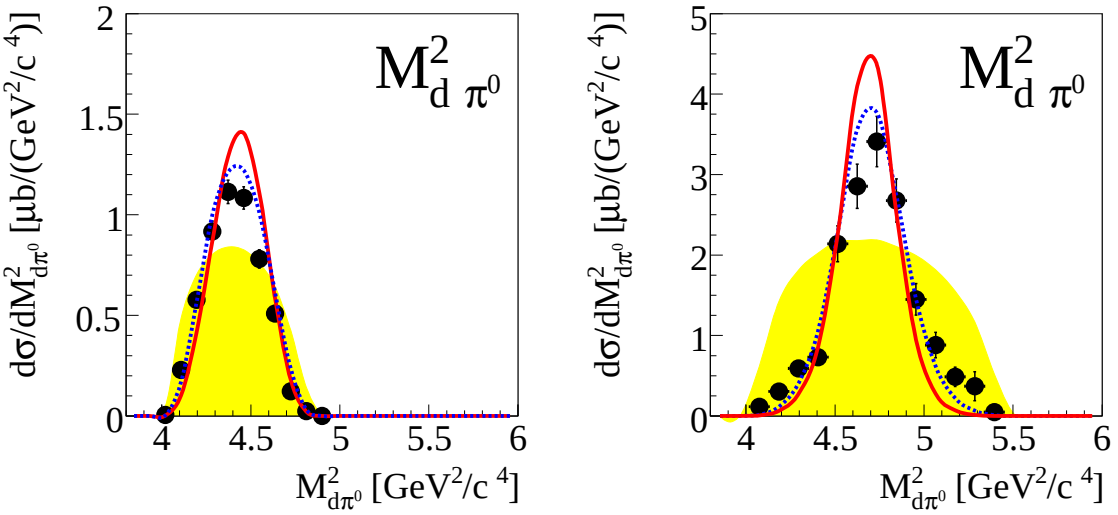

Figure 5.7: Invariant mass distributions $M^2_{d\pi^0}$ at two energy ranges T_p = 1.00-1.03 GeV (left) and T_p = 1.34-1.37 GeV (right). The dashed areas show pure phase-space distributions. Solid and dotted curves give $\Delta\Delta$ calculations with and without the assumption of an s-channel resonance, respectively. All curves are normalized to the experimental integral cross section.

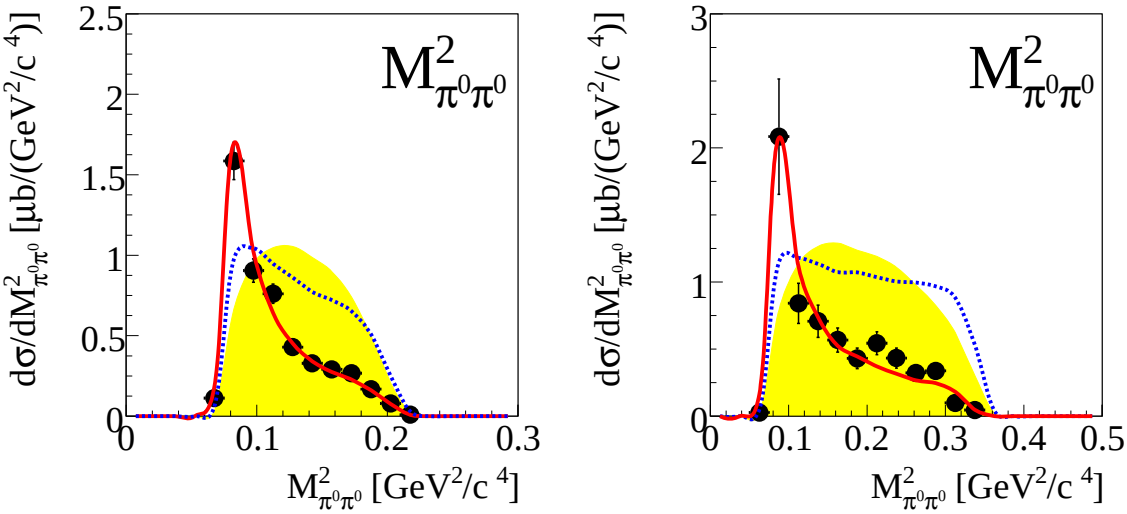

Figure 5.8: Distributions of the invariant masses $M^2_{\pi^0\pi^0}$ at two energy ranges T_p = 1.00-1.03 GeV (left) and T_p = 1.34-1.37 GeV (right). For the meaning of curves and symbols see Fig. 5.7.

5.2.3 Angular distributions

Since we performed an exclusive measurement, we have full kinematic information on this reaction and hence can plot all kinds of angular distributions. In this section, only the most interesting distributions will be discussed.

Figs. 5.10 and 5.11 display the angular distributions in the reaction $pn \to d\pi^0\pi^0$ at beam energies of $T_p = 1.03$ GeV and $T_p = 1.35$ GeV, respectively. The definition of the angles was given in Chap. 5.2.1.

In all angular distributions the yellow area is pure phase space, the black points correspond to the data, the open squares represent the data at $M_{\pi^0\pi^0} \leq 0.32$ GeV/c^2 (region of the low mass enhancement).

On the top left of Fig. 5.10 the distribution of the opening angle $\delta^{d\pi^0\pi^0}_{\pi^0\pi^0}$ between the two pions in the $d\pi^0\pi^0$ (or, equivalently, pn) center-of-mass (c.m.) system is displayed. It shows a strong deviation from the phase space at small angles, in particular if we select events $M_{\pi^0\pi^0} \leq 0.32$ GeV/c^2 (see upper left plot in Figs. 5.10 and 5.11). This means that the pions prefer to fly in parallel with small relative momentum. This feature is assosiated with the low $\pi^0\pi^0$ mass-enhancement.

The distributions of the deuteron polar angle $\theta^{d\pi^0\pi^0}_d$ in the $d\pi^0\pi^0$ c.m. system (top right in Fig. 5.10), of the pion polar angles $\theta^{d\pi^0}_{\pi^0}$ (bottom left in Fig. 5.10) and $\theta^{\pi^0\pi^0}_{\pi^0}$ in the $d\pi^0$ and $\pi^0\pi^0$ subsystems, respectively, are anisotropic and essentially symmetric about 90°. The anisotropy observed for the $\theta^{d\pi^0}_{\pi^0}$ corresponds just to the one expected from Δ decay. The anisotropy in the π^0 angular distribution in the $\pi\pi$ subsystem signals some d-wave admixture. It vanishes, if we consider only data with $M_{\pi^0\pi^0} \leq 0.32$ GeV/c^2, i.e., in the region of the low-mass enhancement. From this we deduce that the enhancement is of scalar nature, i.e., in total of scalar-isoscalar nature.

Fig. 5.9 shows the 3D lego plot of $M^2_{\pi^0\pi^0}$ versus $\theta^{\pi^0\pi^0}_{\pi^0}$. Here one can see the mentioned feature. At low invariant mass the pion angular distribution is almost flat, while at high invariant mass it shows some statistical fluctuations.

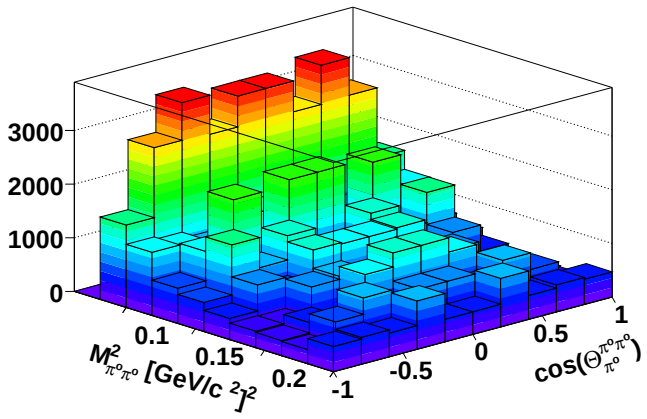

Figure 5.9: 3-dimensional lego plot of $M^2_{\pi^0\pi^0}$ versus $\theta^{\pi^0\pi^0}_{\pi^0}$ for the reaction $pn \to d\pi^0\pi^0$ at $T_p = 1.35$ GeV.

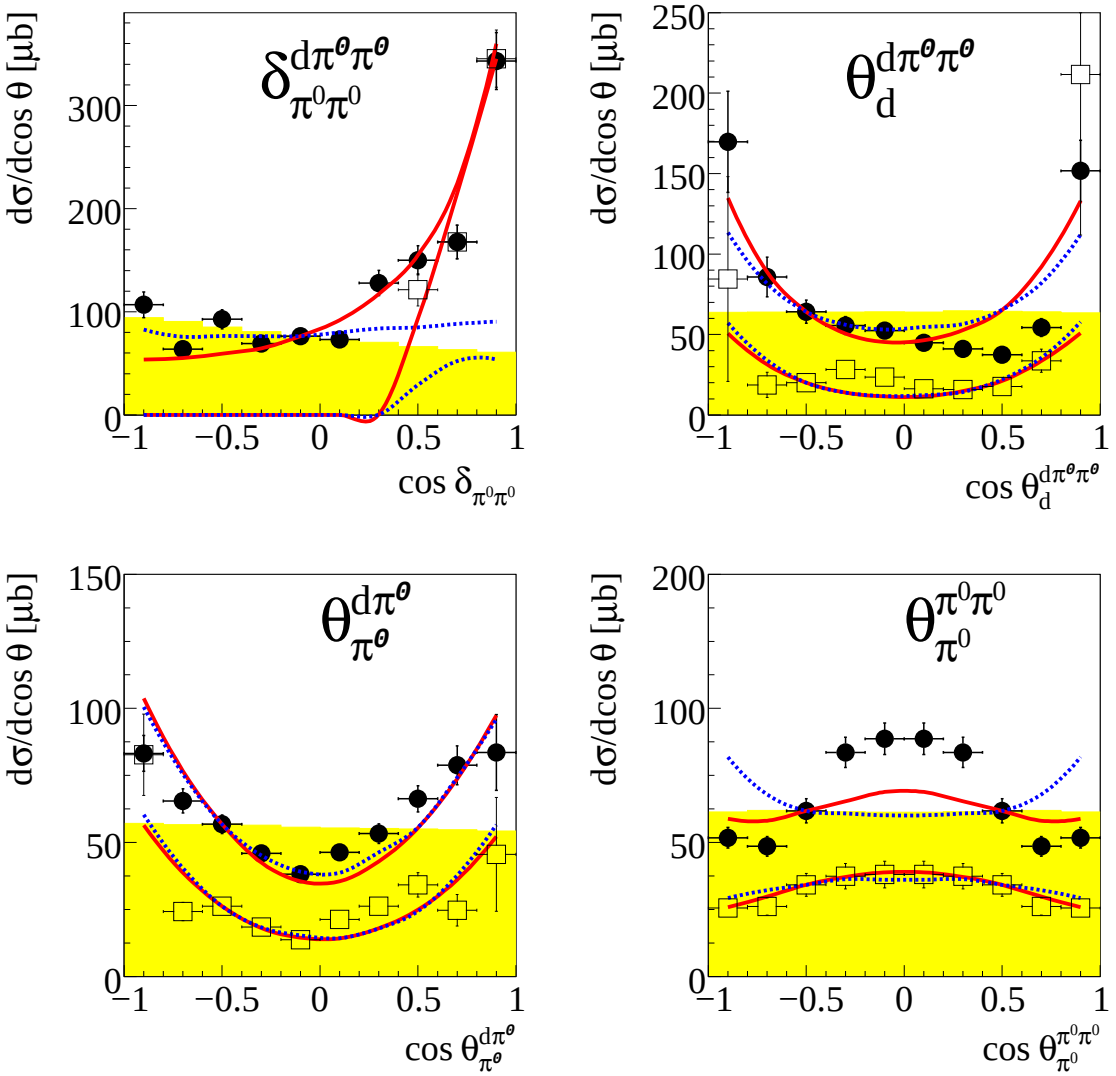

Figure 5.10: Angular distributions in the reaction $pn \to d\pi^0\pi^0$ at a beam energy of $T_p = 1.03$ GeV .
The first row: the opening angle $\delta_{\pi^0\pi^0}$ between the two pions (left), the angle of deuteron $\theta_d^{d\pi^0\pi^0}$ in the overall centre of mass system (right).
The second row: the polar angle of pion $\theta_{\pi^0}^{d\pi^0}$ (left), the angle of pion $\theta_{\pi^0}^{\pi^0\pi^0}$ in $\pi\pi$ subsystem (Jackson frame) (right). The yellow area corresponds to the pure phase space. The dashed blue line represents the $\Delta\Delta$ calculation without assumption of a resonance between two deltas. The red line shows the $\Delta\Delta$ calculation, if one assumes a s-channel resonance in the $\Delta\Delta$ system. The black points represent data at the full region, while the open squares show the data with the constraint $M_{\pi^0\pi^0} \leq 0.32$ GeV/c^2. All curves are normalized to the experimental integral cross section.

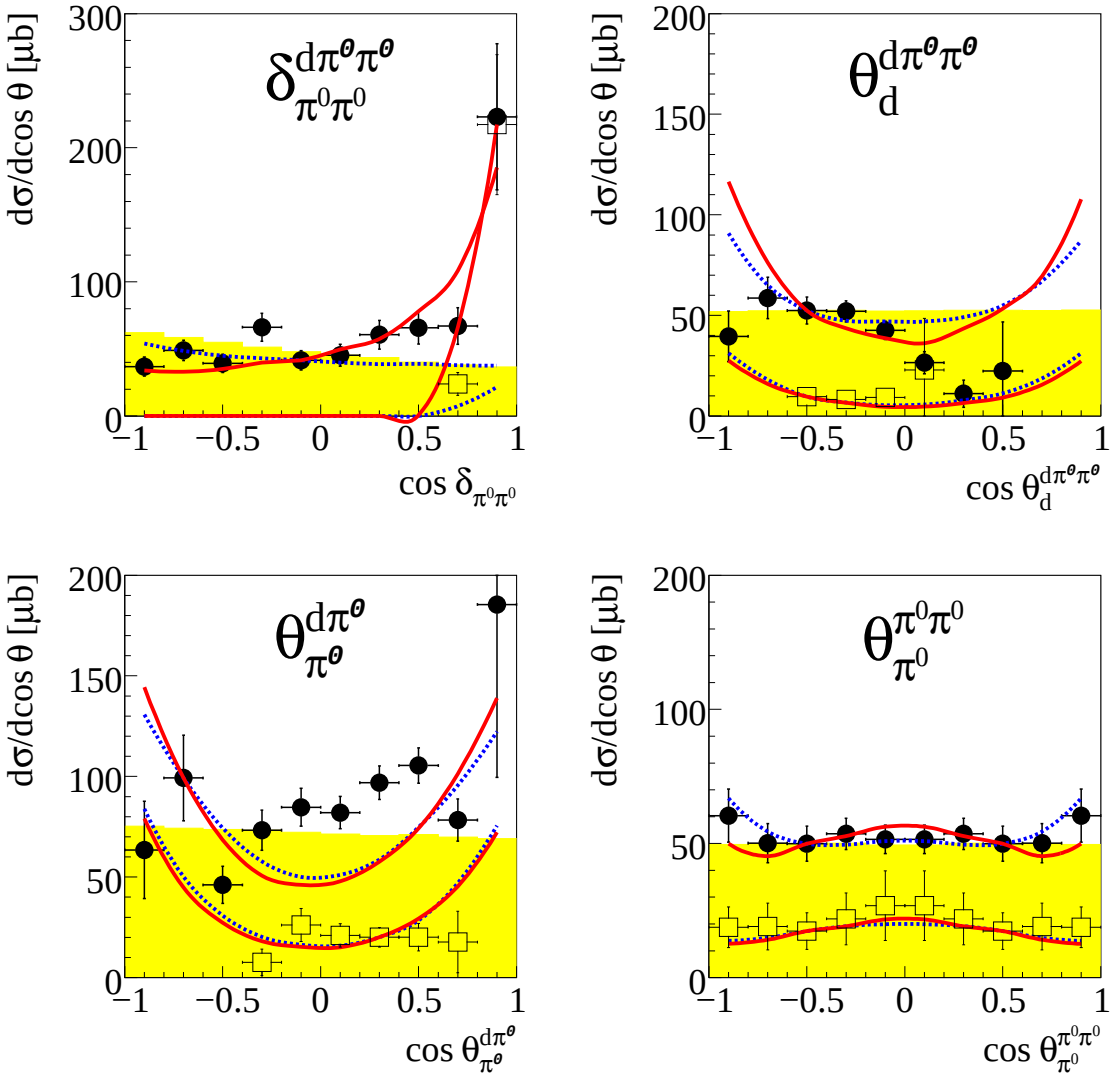

Figure 5.11: Angular distributions in the reaction $pn \to d\pi^0\pi^0$ at a beam energy of $T_p = 1.35$ GeV .
The first row: the opening angle $\delta_{\pi^0\pi^0}$ between the two pions (left), the angle of deuteron $\theta_d^{d\pi^0\pi^0}$ in the overall centre of mass system (right).
The second row: the polar angle of pion $\theta_{\pi^0}^{d\pi^0}$ (left), the angle of pion $\theta_{\pi^0}^{\pi^0\pi^0}$ in $\pi\pi$ subsystem (Jackson frame) (right). The yellow area corresponds to the pure phase space. The dashed blue line represents the $\Delta\Delta$ calculation without assumption of a resonance between two deltas. The red line shows the $\Delta\Delta$ calculation, if one assumes a s-channel resonance in the $\Delta\Delta$ system. The black points represent data at the full region, while the open squares show the data with the constraint $M_{\pi^0\pi^0} \leq 0.32$ GeV/c^2. All curves are normalized to the experimental integral cross section.

5.3 Fermi smearing in the total cross section

The advantage of measuring the quasifree reaction is that due to Fermi motion one measures at several energies instead of only one. The Fermi momentum inside the target leads to a spread distribution in the invariant mass $M_{d\pi^0\pi^0}$ (see Fig. 5.12), which is equivalent to the total energy in center-of-mass system (CMS) $\sqrt{s}$.

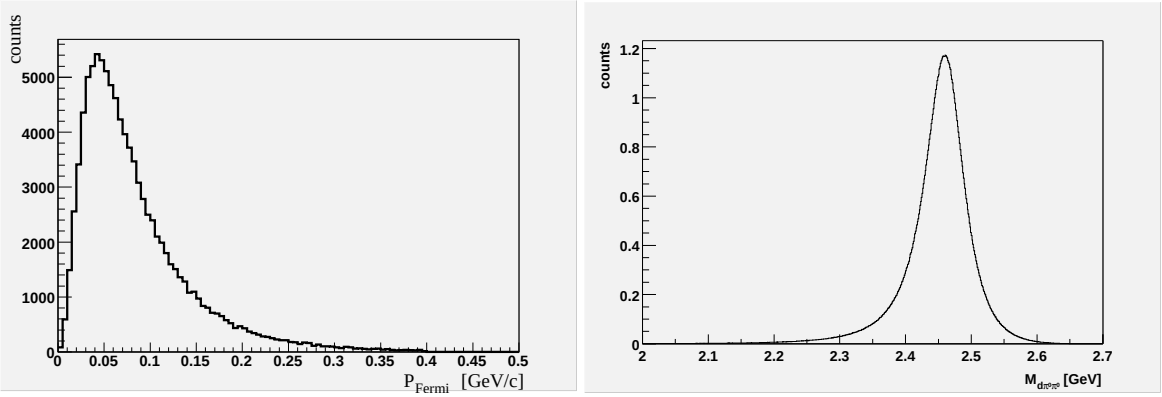

Figure 5.12: Left: Theoretically calculated Fermi momentum of the nucleons inside the target deuteron. Right: Invariant mass $M_{d\pi^0\pi^0}$ distribution (MC).

In order to extract the energy dependence in the total cross section, we divided event-by-event the measured experimental total CMS energy by the generated total CMS energy distribution (see Fig. 5.12 right). The thus obtained data have been binned into small ranges of effective beam energy. For the beam energies of $T_p = 1.03$ GeV and $T_p = 1.35$ GeV the $\sqrt{s}$ distribution was divided into 4 bins. The resulting data are shown by the open blue dots in Fig. 5.17.

5.4 Theoretical models

5.4.1 Conventional $\Delta\Delta$ calculation

Since the ABC enhancement occurs at center of mass energies $\sqrt{s} \approx 2M_\Delta$, it is tempting to describe the two pion production via a double Δ excitation as first suggested by T. Risser and M.D. Shuster [Ris73] and later used and partly improved by others [Alv98, Bar73, Mos99]. The graph for a such a t-channel $\Delta\Delta$ excitation is depicted in Fig. 5.13.

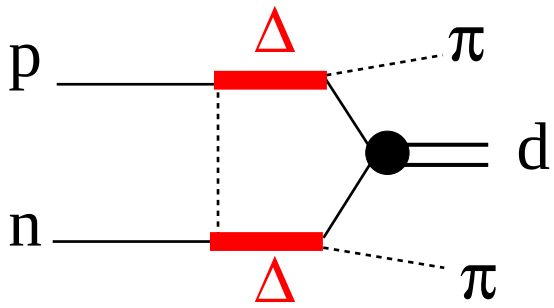

Figure 5.13: Diagram of the $pn \rightarrow d\pi^0\pi^0$ process via the t-channel $\Delta\Delta$ excitation.

In such a calculation the cross section for the reaction $pn \rightarrow d\pi^0\pi^0$ is given by:

$$\sigma \sim |\Delta_1 \cdot \Delta_2|^2 \cdot (1 + 2cos(\theta^{d\pi^0_1}_{\pi^0_1})) \cdot (1 + 2cos(\theta^{d\pi^0_2}_{\pi^0_2})) \cdot PhaseSpace \tag{5.12}$$

where $\theta^{d\pi^0_1}_{\pi^0_1}$ and $\theta^{d\pi^0_2}_{\pi^0_2}$ are the angles of the first and the second pion in the deuteron-pion system, respectively.

Note that in equation 5.12 instead of the term $3cos\theta$ the term $2cos\theta$ is used, because a better description of the data has been obtained by this choice.

The relativistic Breit-Wigner squared amplitude is given by:

$$|\Delta|^2 = \frac{\Gamma^2 / {P^{d\pi}_\pi}^2}{(M^2_{d\pi} - M^2_\Delta)^2 + M^2_\Delta \cdot \Gamma^2} \tag{5.13}$$

here $P^{d\pi}_\pi$ is the momentum of the pion in the deuteron-pion system, the resonance mass is $M_\Delta = 1.23$ GeV and the width:

$$\Gamma = \frac{\gamma \cdot R^2 \cdot (P^{d\pi}_\pi)^2}{1 + R^2 \cdot (P^{d\pi}_\pi)^2} \tag{5.14}$$

where $\gamma = 0.74$ and $R = 6.3$ (GeV/c)$^{-1}$, taken from [Ris73].

The results of this calculation (blue curve in Fig. 5.14) are compared to the phase space (yellow area).

The calculation shows two enhancements at low and at high invariant masses relative to the phase space. As mentioned in Chap. 1.2, the peak at low $\pi\pi$ invariant masses corresponds to the case, where two pions move in parallel in the $\Delta\Delta$ system with small relative momentum $q_{\Delta\Delta}$, whereas the high -mass enhancement results, when the pions fly antiparallel in the $\Delta\Delta$ system with large $q_{\Delta\Delta}$.

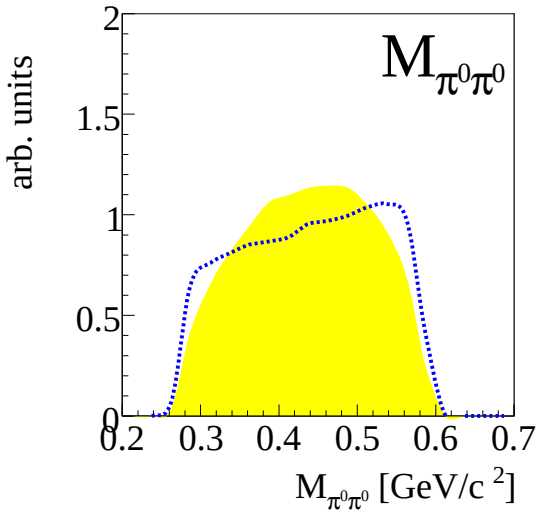

Figure 5.14: Distribution of invariant mass $M^0_\pi\pi^0$. The yellow area corresponds to the phase space, the blue line depicts the result of $\Delta\Delta$ calculation according to the formula 5.12.

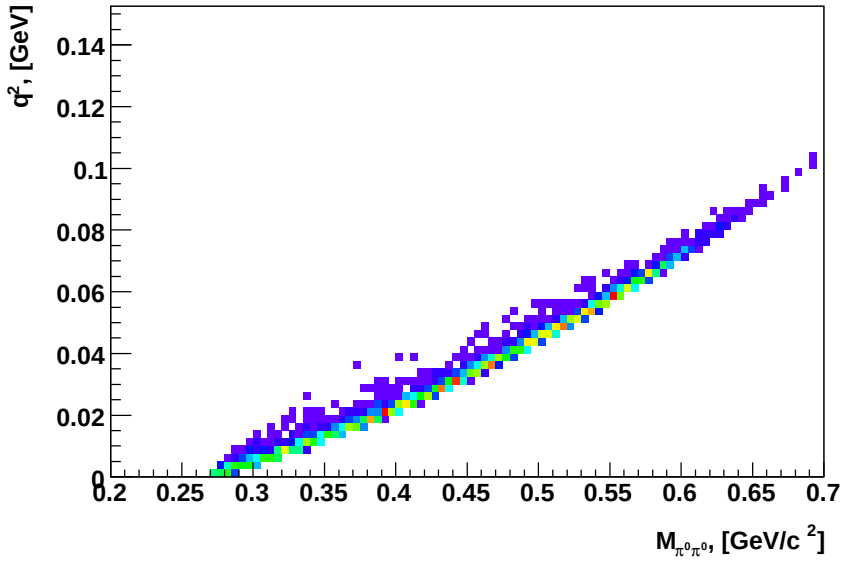

Figure 5.15: MC simulation of the $pn \rightarrow d\pi^0\pi^0$ reaction at $T_p = 1.35$ GeV according to the equation 5.12. The xy-plane represents the invariant mass $M_{\pi^0\pi^0}$ against the relative momentum $q_{\Delta\Delta}$ in the $\Delta\Delta$ system. The z-axis corresponds to the differential cross section.

Fig. 5.15 shows the connection between relative $\Delta\Delta$ momentum $q_{\Delta\Delta}$ and invariant mass of two pions $M_{\pi^0\pi^0}$. We see a clear correlation in the differential cross section between $M_{\pi^0\pi^0}$ and $\Delta\Delta$ relative momentum $q_{\Delta\Delta}$ with low-mass enhancement with small relative momentum of $\Delta\Delta$ pair and high-mass enhancement with large $q_{\Delta\Delta}$.

If we compare with our exclusively measured data, we see a large deviation from this $\Delta\Delta$ calculation. All available $\Delta\Delta$ calculations [Bar73, Mos99] which give a reasonable description of the inclusive data, fail badly in the case of exclusively measured data, since they predicted a double-hump structure for the $M_{\pi^0\pi^0}$ spectrum.

5.4.2 Isospin decomposition for $\pi\pi$ channels

Although conventional $\Delta\Delta$ models are not able to describe the differential cross sections exclusively measured at CELSIUS/WASA, the data nevertheless show a double Δ excitation in the invariant mass $M_{d\pi^0}$ (Figs. 5.5, 5.7).

Fig. 5.16 depicts the dependence of the cross section on the total mass of the full system $M_{d\pi^0\pi^0} = \sqrt{s}$ and the invariant pion-pion mass $M_{\pi^0\pi^0}$ at $T_p = 1.03$ GeV (left) and at $T_p = 1.35$ GeV (right) respectively. Here we see a strong correlation between the enhancement at low $\pi\pi$ invariant mass and the peak in the $\sqrt{s}$ distribution. That means that the ABC effect is related to a resonance in the total cross section as evident in Fig. 5.17, which displays the energy dependence of the total cross section.

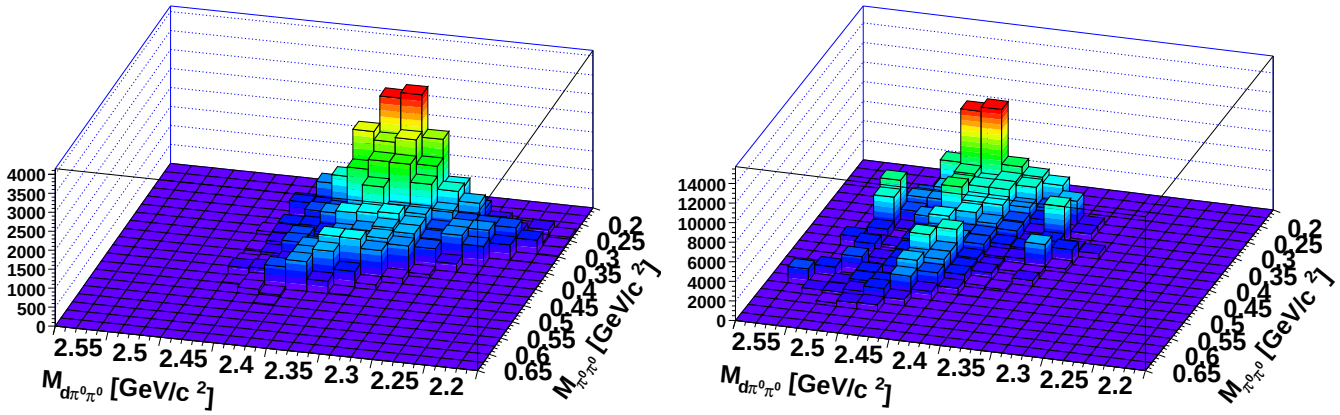

Figure 5.16: 3-dimensional lego plot of the $M_{d\pi^0\pi^0}$ versus $M_{\pi^0\pi^0}$. The left distribution corresponds to the beam energy $T_p = 1.03$ GeV, while the right plot to $T_p = 1.35$ GeV. The low $\pi\pi$ mass enhancement matches the resonance in the total cross section.

Next we look at the isospin relations in $NN \to d\pi\pi$ reactions:

- in the $pp \to d\pi^+\pi^0$ reaction the $\pi^+\pi^0$ pair has only an isovector part $I = 1$
- in the $pn \to d\pi^+\pi^-$ reaction the $\pi^+\pi^-$ pair may have $I = 0$ and $I = 1$
- in the $pn \to d\pi^0\pi^0$ reaction the $\pi^0\pi^0$ pair is in a pure isoscalar state $I = 0$

The cross sections of these reactions based on the mechanism shown in Fig. 5.13 in terms of the isospin amplitudes are as follows [Dak83]:

$$\begin{aligned}
\sigma(pp \to d\pi^+\pi^0) &= \tfrac{1}{4}|M_{011}|^2 := \sigma_1 \\
\sigma(pn \to d\pi^0\pi^0) &= \tfrac{1}{24}|M_{000}|^2 := \sigma_0 \\
\sigma(pn \to d\pi^+\pi^-) &= \tfrac{1}{12}|M_{000}|^2 + \tfrac{1}{8}|M_{011}|^2 := 2\sigma_0 + \tfrac{1}{2}\sigma_1
\end{aligned} \tag{5.15}$$

where $M_{I_f^{NN} I_{\pi\pi} I_i^{NN}}$ are the reduced isospin matrix elements of the transition from the initial to the final state. I_f^{NN} is the isospin of the NN system in the final state, $I_{\pi\pi}$ is the isospin of the $\pi\pi$ system and I_i^{NN} is the isospin of the NN system in the initial state.

From (5.15) we obtain the relation:

$$\sigma(pp \to d\pi^+\pi^0) + 4\sigma(pn \to d\pi^0\pi^0) = 2\sigma(pn \to d\pi^+\pi^-) \tag{5.16}$$

If one assumes that the reactions proceed via *the same reaction mechanism*, i.e. in our case via t-channel $\Delta\Delta$ excitation, then the matrix elements are related to each other by isospin recoupling coefficients [Clem, Edm64], i.e.:

$$\begin{aligned}
&M_{I_f^{NN} I_{\pi\pi} I_i^{NN}} = M_{\Delta_1} M_{\Delta_2} \\
&\times((I_{N_1} I_{\pi_1}) I_{\Delta_1}, (I_{N_2} I_{\pi_2}) I_{\Delta_2}, I_{\Delta\Delta} m | (I_{N_1} I_{N_2}) I_f^{NN}, (I_{\pi_1} I_{\pi_2}) I_{\pi\pi}, I_{\Delta\Delta} m) = \\
&= M_{\Delta_1} M_{\Delta_2} \sqrt{(2I_{\Delta_1}+1)(2I_{\Delta_2}+1)(2I_f^{NN}+1)(2I_{\pi\pi}+1)} \begin{Bmatrix} I_{N_1} & I_{\pi_1} & I_{\Delta_1} \\ I_{N_2} & I_{\pi_2} & I_{\Delta_2} \\ I_f^{NN} & I_{\pi\pi} & I_{\Delta\Delta} \end{Bmatrix}
\end{aligned} \tag{5.17}$$

with $I_{\Delta\Delta} = I_i^{NN}$ and M_{Δ_1} and M_{Δ_2} being the reduced Matrixelements for Δ-excitation in each of the participating nucleons (see [Edm64] eq. 7.1.5).

From this we obtain:

$$
\begin{aligned}
M_{111}^{\Delta\Delta} &= 0 \\
M_{000}^{\Delta\Delta} &= -3M_{121}^{\Delta\Delta} \\
M_{101}^{\Delta\Delta} &= -\sqrt{5}M_{121}^{\Delta\Delta} \\
M_{011}^{\Delta\Delta} &= \sqrt{\tfrac{15}{2}}M_{121}^{\Delta\Delta} \\
M_{110}^{\Delta\Delta} &= \tfrac{3}{\sqrt{2}}M_{121}^{\Delta\Delta}
\end{aligned}
\tag{5.18}
$$

From the relations (5.18) follows:

$$
M_{000}^{\Delta\Delta} = -\sqrt{\frac{6}{5}}M_{011}^{\Delta\Delta} \tag{5.19}
$$

Since the cross section of the reaction $pp \to d\pi^+\pi^0$ is known and well described by the conventional $\Delta\Delta$ t-channel calculation [Kre08], the isoscalar part of such an excitation mechanism can be derived. The relevant relation between the corresponding total cross sections is then:

$$
\sigma(pn \to \Delta\Delta \to d\pi^0\pi^0) = \frac{1}{5}\sigma(pp \to \Delta\Delta \to d\pi^+\pi^0) \tag{5.20}
$$

From (5.16) and (5.20) we also obtain:

$$
\sigma(pn \to \Delta\Delta \to d\pi^+\pi^-) = \frac{9}{10}\sigma(pp \to \Delta\Delta \to d\pi^+\pi^0) \tag{5.21}
$$

Fig. 5.17 displays the energy dependence of the total cross sections of these reactions. The picture depicts the result of this work for the $pn \to d\pi^0\pi^0$ reaction in comparison with the the data of the $pn \to d\pi^+\pi^-$ reaction [Abd79] and with results of the $pp \to d\pi^+\pi^0$ reaction [Bys87]. As mentioned above in the reaction $pp \to d\pi^+\pi^0$ only isospin $I = 1$ contributes. This isovector part σ_1 is shown in Fig. 5.17 by the dotted black line by use of the conventional t-channel $\Delta\Delta$ calculation adjusted in height to the $pp \to d\pi^+\pi^0$ data.

The obtained isoscalar component σ_0 is shown by the dotted blue line in Fig. 5.17, while the noninterfering sum of scalar σ_0 and isovector σ_1 parts are given by the dashed red line. Indeed, the $\pi^+\pi^-$ data are in reasonable agreement with this sum for $\sqrt{s} \geq$2.5 GeV. At lower energies, however, the measured cross section is much larger than expected from conventional $\Delta\Delta$ process.

Since the $\pi^0\pi^0$ channel is purely isoscalar, one should compare the data to the dotted blue line, which containes only $I = 0$. However, one can see the large

discrepancy between both, in particular for $\sqrt{s}$ ≤2.5 GeV. Our data show a behavoir, which is much larger and narrower than expected from the conventional ΔΔ calculation. Also the peak position in the cross section is shifted below the nominal ΔΔ threshold.

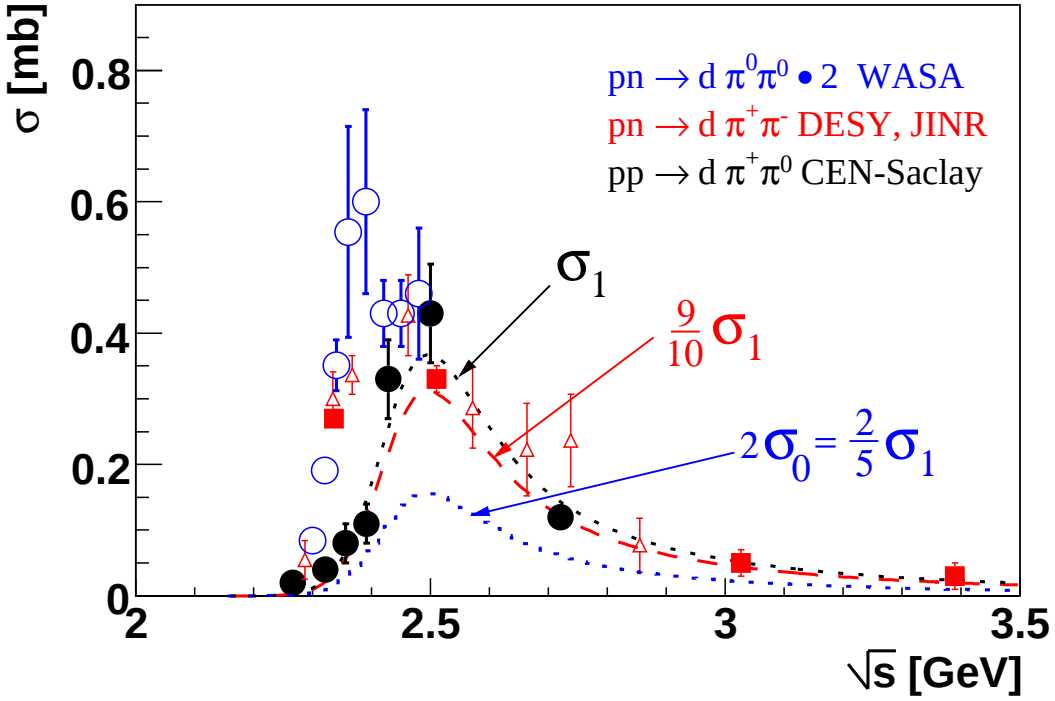

Figure 5.17: Energy dependence of the total cross section for $pn \rightarrow d\pi^+\pi^-$ reaction. The red squares is a result from [Abd79], while the red open triangles depicts the result from [Bar73]. The CELSIUS/WASA data are shown by open blue dots. Due to the isospin relation the $\pi^0\pi^0$ channel is scaled by a isospin factor of 2. The dashed curves (in the corresponding colors) represent the calculation based on the conventional t-channel ΔΔ model [Ris73] normalized according to the isospin relations described above.

5.4.3 An s-channel resonance model

In order to describe our experimental data, we use the following Breit-Wigner ansatz for a resonance amplitude:

$$A_R \sim F(q_{\Delta\Delta}) \cdot D_R \cdot D_{\Delta_1} \cdot D_{\Delta_2} \tag{5.22}$$

where D_{Δ_1} and D_{Δ_2} are Δ_1 and Δ_2 propagators (see equation 5.13) and D_R corresponds to the s-channel resonance (see Fig. 5.18, left) and is given by:

$$D_R = \frac{1}{(M_{\Delta\Delta} - M_R) - i\frac{\Gamma_R}{2}} \tag{5.23}$$

with a mass $M_R \approx 2M_\Delta - 2 \cdot (34MeV) \approx 2.36$ GeV/c^2 and a width $\Gamma_R \approx 80$ MeV, both obtained by a fit to the data.

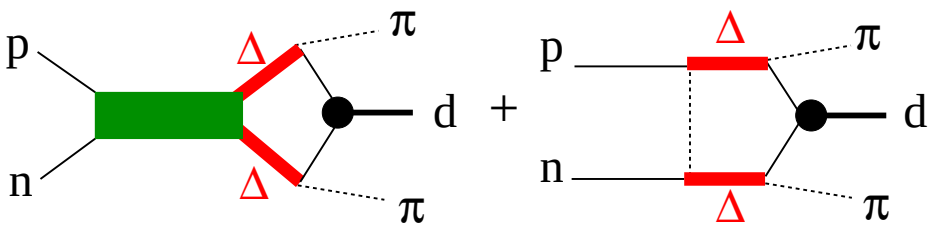

Figure 5.18: Diagrams of the $pn \rightarrow d\pi^0\pi^0$ process. The left diagram corresponds to the s-channel resonance, whereas the right diagram depicts the conventional t-channel $\Delta\Delta$ excitation.

The form factor $F(q_{\Delta\Delta})$ of the $\Delta\Delta$ vertex depends on the relative momentum $q_{\Delta\Delta}$ between $\Delta\Delta$ and is defined as:

$$F\left(q_{\vec{\Delta\Delta}}\right) = \frac{\Lambda^2_{\Delta\Delta}}{\Lambda^2_{\Delta\Delta} + q^{\vec{2}}_{\Delta\Delta}} \tag{5.24}$$

The obtained cutoff parameter $\Lambda_{\Delta\Delta}$ of the monopole formfactor was fitted to the data in the invariant mass $M_{\pi\pi}$ spectra and results in $\Lambda_{\Delta\Delta} \approx 0.2$ GeV/c.

If we omit the Fermi motion of the nucleons, then:

$$q_{\Delta\Delta} = (\vec{p_n} + \vec{p_{\pi_1}}) - (\vec{p_p} + \vec{p_{\pi_2}}) \approx p_{\pi_1} - p_{\pi_2} = q_{\pi\pi} \tag{5.25}$$

As mentioned in the previous Chap. 5.4.1 the correlation between the relative momentum $q_{\Delta\Delta}$ and invariant mass of two pions $M_{\pi\pi}$ shows that low-mass enhancement corresponds to small relative momentum $q_{\Delta\Delta}$, whereas the high-mass peak corresponds to large relative momentum $q_{\Delta\Delta}$ (see Fig. 5.15).

Hence, in order to describe the experimental data one has to enhance the case with small relative momentum and low invariant mass and suppress the configuration with large relative momentum and high invariant mass. The formfactor given in the equation (5.24) just provides such a tool. The result of the Monte Carlo simulation based on the equations (5.22)-(5.24) is shown in Fig. 5.19.

By comparing Fig. 5.14 and Fig. 5.21, one sees that in the last case only the low invariant mass peak is present, while the enhancement at high invariant mass is absent.

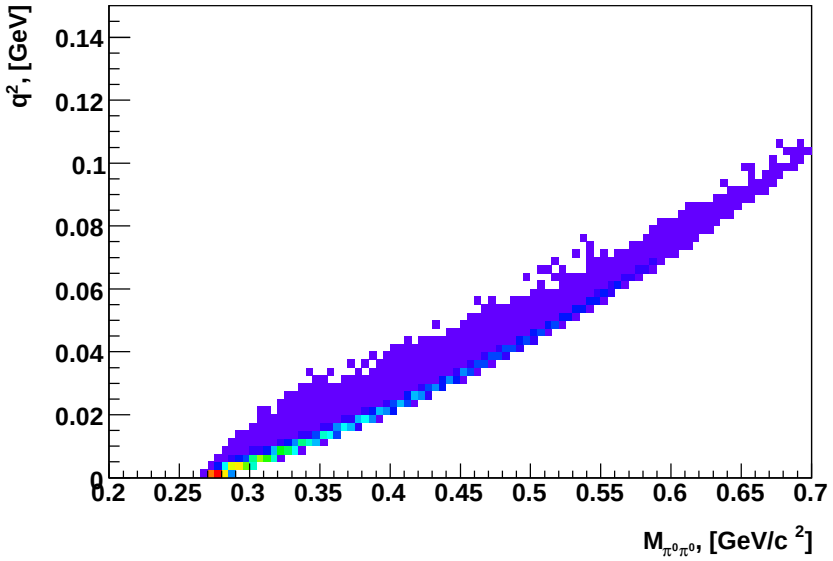

Figure 5.19: Simulated cross section of the $pn \to d\pi^0\pi^0$ reaction at $T_p = 1.35$ GeV according to the equations (5.22)-(5.24) in a $M_{\pi\pi}$-q^2 plane.

The result of the calculation is shown in Fig. 5.20 by the solid blue line. With such a simple ansatz, we achieve a good description of $pn \to d\pi^0\pi^0$ data in the total cross section as well as in the differential spectra. Fig. 5.21 shows the invariant mass of two pions $M_{\pi^0\pi^0}$. The solid red curve represents the $\Delta\Delta$ calculation including a s-channel resonance, which provides a good agreement with experimental data.

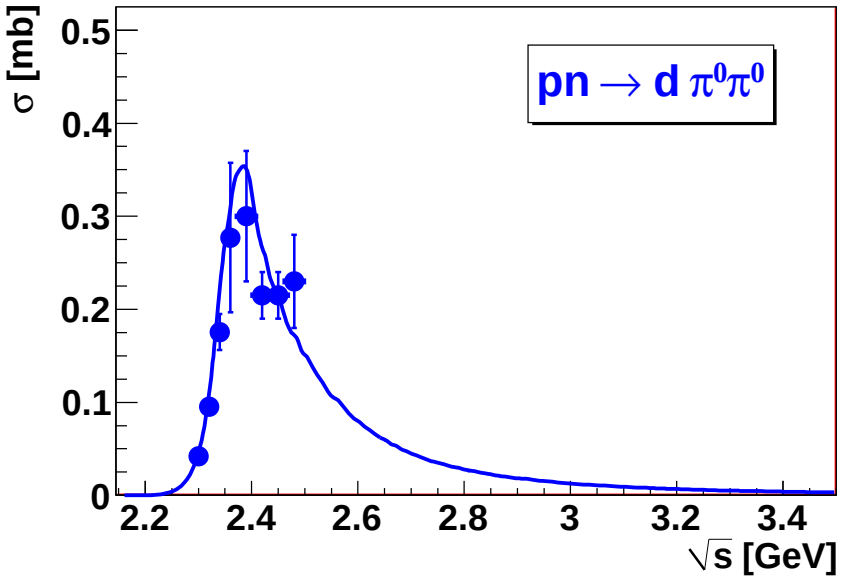

Figure 5.20: Energy dependence of the total cross section for $pn \rightarrow d\pi^0\pi^0$ reaction. The CELSIUS/WASA data are shown by solid blue dots. The solid blue curve is including the both mechanisms shown in Fig. 5.18.

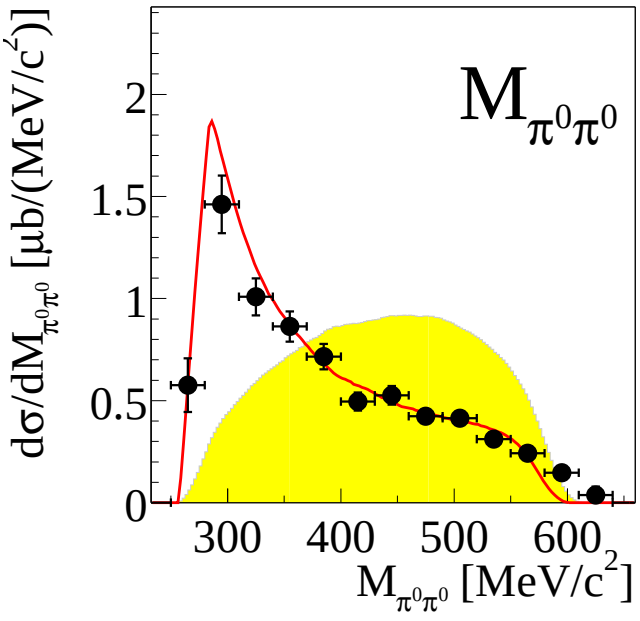

Figure 5.21: Distribution of invariant mass $M^0_\pi\pi^0$ at $T_p = 1.35$ GeV. The yellow area corresponds to the phase space, the red line includes the calculation of the s-channel resonance in the $\Delta\Delta$ system according to the equations (5.22)-(5.24).

Chapter 6

CELSIUS/WASA vs WASA@COSY

Meanwhile the CELSIUS/WASA experiment has been successfully completed and in 2005 the WASA Detector has found a new place in the COSY Ring in Jülich/Germany. After the successful movement and reassembly of the detector, the hard- and software got many updates.

6.1 COSY Ring

The COSY is an acronym for **CO**oler **SY**nchrotron, see Fig. 6.1. The COSY ring has a length of 184 m and consists of four types of magnets:

- 24 dipole magnets (red) and 56 quadrupole magnets (yellow), which focus the particle beam and keep it on its trajectory
- the sextupole magnets additionally correct the particle trajectory
- a fourth type of magnet, the "steerers", which are used for beam deflection in a controlled manner and guiding to the internal target

The COSY has many attractive features:

- good beam quality due to the following cooling methods:
  - electron cooling: the light electrons can be focused into a uniform beam much more easily than protons. They are inserted into the beam using magnetic field and afterwards transfer their disciplined behaviour to the beam particles and are extracted from the beam after having travelled for two meters. The disadvantage of this method is, that this process reaches a limit since protons are heavier than electrons, and electrons would need more energy to "cool" the protons further. If an electron beam will hit the vacuum wall, there would be a hole in the beam tube and the machine would be stopped automatically. A maximum of 300 kV has been achieved up to now.

  - stochastic cooling: used for high energy protons. The principle of this method is as follows: for a small fraction of high speed protons a signal pick-up probe measures the difference from the ideal value. The correction signal sent to the opposite side of the ring counteracts this deviation. The beam particles is brought back onto the right trajectory by a short electric "kick".

- a proton and a deuteron beams with high intensity
- spin polarized beams
- a beam also for external experiments

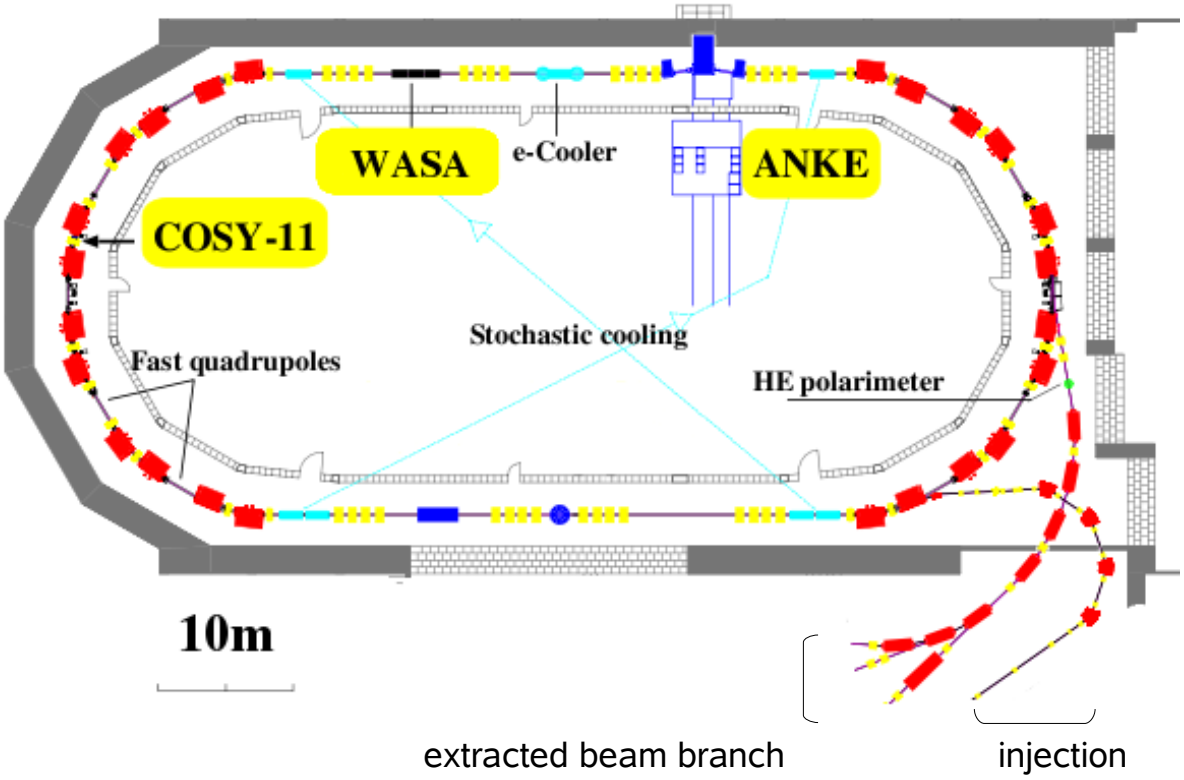

Figure 6.1: View of the COSY ring. Besides the internal experiments (in yellow) there are also a large number of the external experiments.

6.2 WASA@COSY

The WASA@COSY setup looks very similar to the previous CELSIUS/WASA detector, see Fig. 6.2. The central detector remains almost the same. The forward detector is somewhat different from to the prior setup.

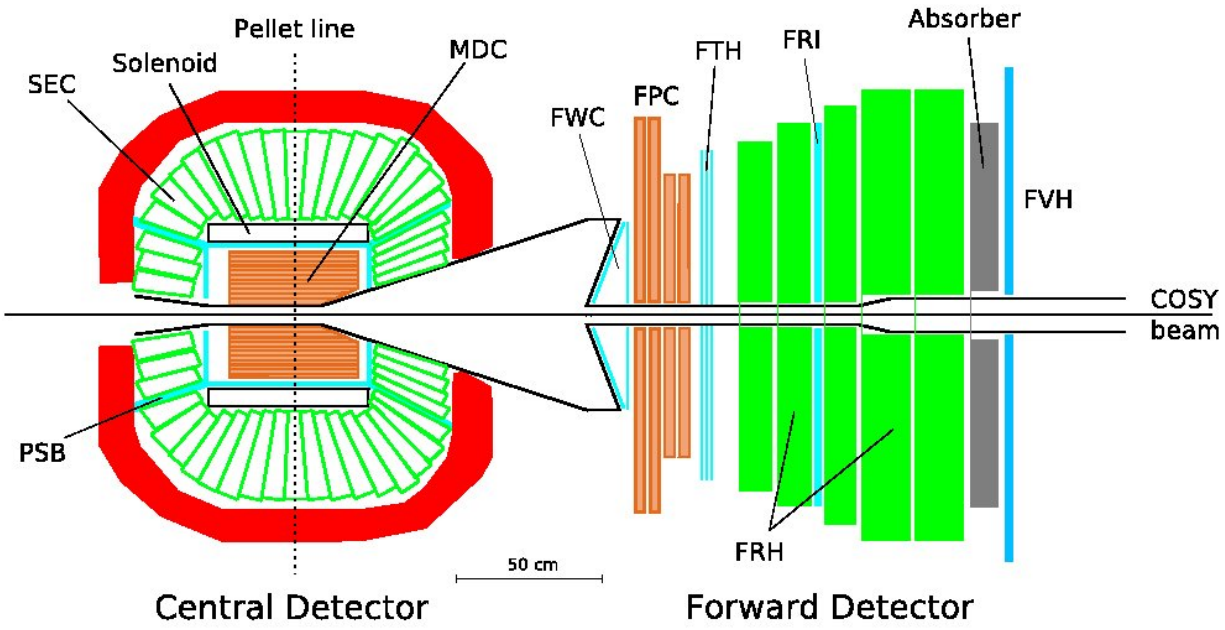

Figure 6.2: Schematic top view of the WASA@COSY detector setup.

6.2.1 DAQ and software

Since COSY has a higher intensity compared to CELSIUS, a higher particle flux and event rates are expected. Therefore the old DAQ has been replaced by a third generation DAQ at COSY. It was developed at ZEL (Zentrallabor für Elektronik) and is called EMS (Experimental Message Specification). The new DAQ system has many advantages:

- reduction of the dead time through multi-event-modus
- Gigabit LAN to readout-PC
- trigger-control-system using a star topology

Due to the change of the DAQ, i.e. the new data format, new software was required. The new analysis is based on the RootSorter software. RootSorter is an analysis framework based on ROOT. It allows parallel migration and code development for different detector components of WASA.

6.2.2 The New Forward Window Counter (FWC)

Since the old FWC detector no longer fulfilled the improved conditions at COSY, e.g. the strongly increased luminosities and particle flux, it was replaced by a newly designed detector with much higher granularity. A new forward window counter (FWC) was designed and built by the Tübingen group. It consists of two 3 mm thick layers with 24 elements each [Pri].

The first layer is conical and sitting just at the scattering chamber, while the second layer is planar and rotated by half an element relative to the first layer, see Figs. 6.3 and 6.4. For better light output, twisted adiabatic lightguides were designed. The installation of the new FWC has many advantages:

- improvement of homogeneity, ΔE resolution and also timing
- due to the higher granularity and a second layer it is possible to use the FWC for triggering, in particular for He particles
- it is also used as the start detector for Time-of-Flight measurements

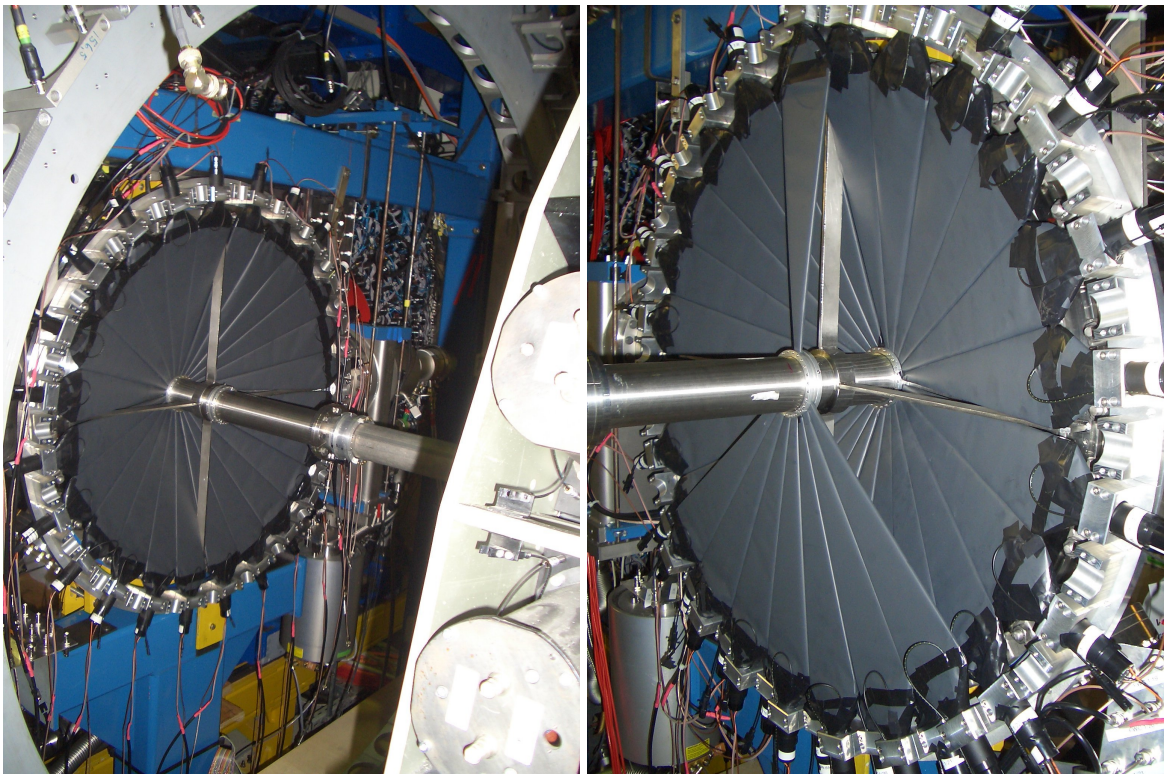

Figure 6.3: Photos of the installation of the Forward Window Counter. The left picture shows the first inclined layer consisting of 24 "pizza piece" elements. On the right photo the beginning of the installation of the second planar layer is shown.

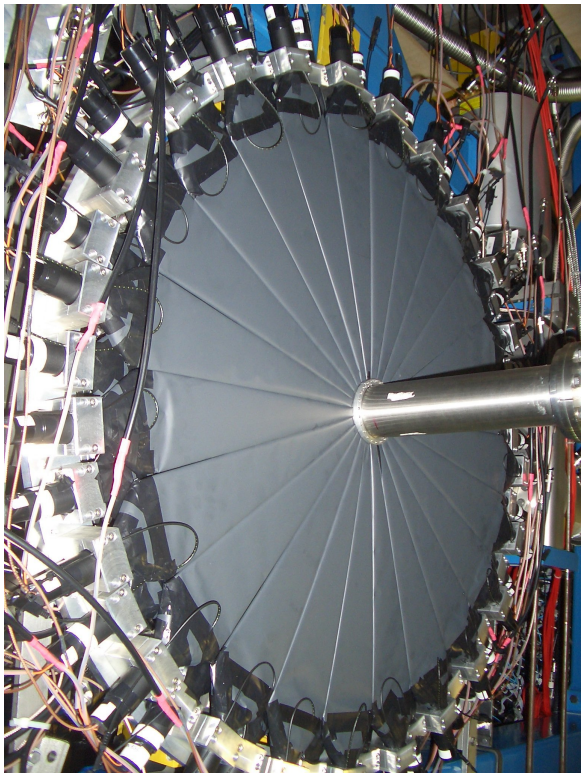

Figure 6.4: The second planar layer of the Forward Window Counter.

6.2.3 The New Forward Veto Hodoscope (FVH)

Due to installation of two additional layers into the Forward Range Hodoscope, each 15 cm thick and with a radius of 90 cm, the polar angle coverage and the distance between the FVH and the interaction point have been increased. This fact requires a new solution of the problem. Therefore, it was necessary to built a new, additional Forward Veto Hodoscope (FVH), which is larger than the previous one [Pri, Per].

The design is almost the same:

- it consists of a 20 + 2 rectangular vertical bars with double-sided readout
- 14 bars have a lenght of 2.5 m and 6 bars are 1.9 m long
- the middle element at the beampipe is composed of two halfbars, one above and one below the beampipe, with readout at both ends of the bars

Such arrangement has many advantages:

- decreasing of inhomogeneities at the beam pipe
- the overlap with the old FVH will give a x-y position
- improvement of the time resolution

- in combination with the new Forward Window Counter the new FVH will be used for Time-of-Flight measurements

Fig. 6.5 shows the new design of the FVH.

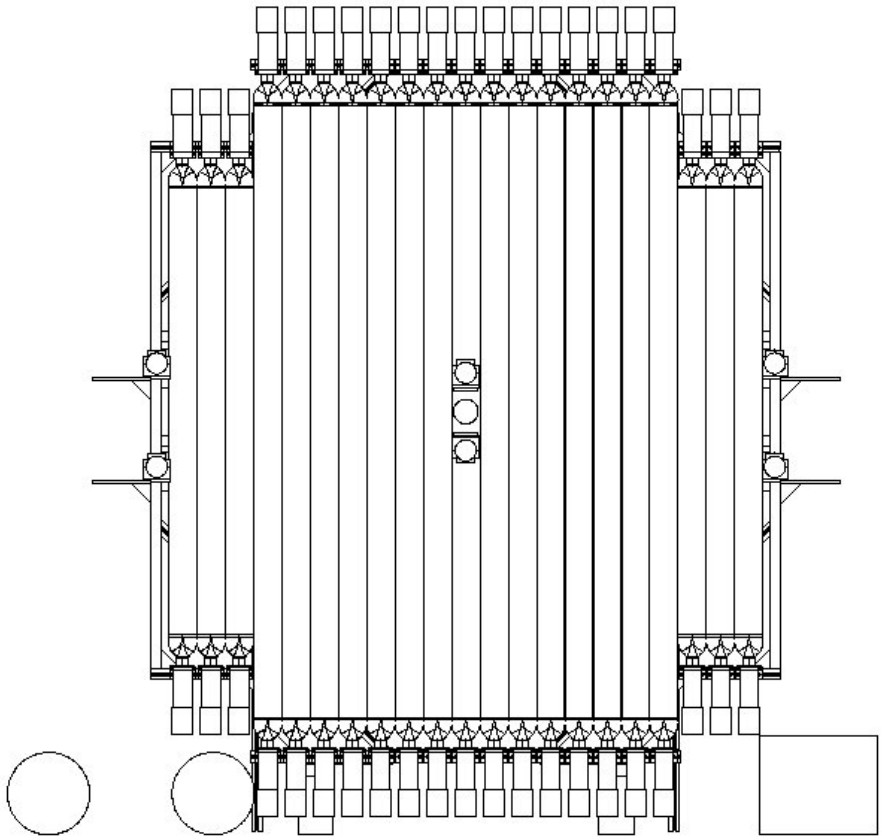

Figure 6.5: Schematic view of the new Forvard Veto Hodoscope.

The installation of the new FVH was done in summer 2008 by the Tübingen group. Some photos show the processes and their result.

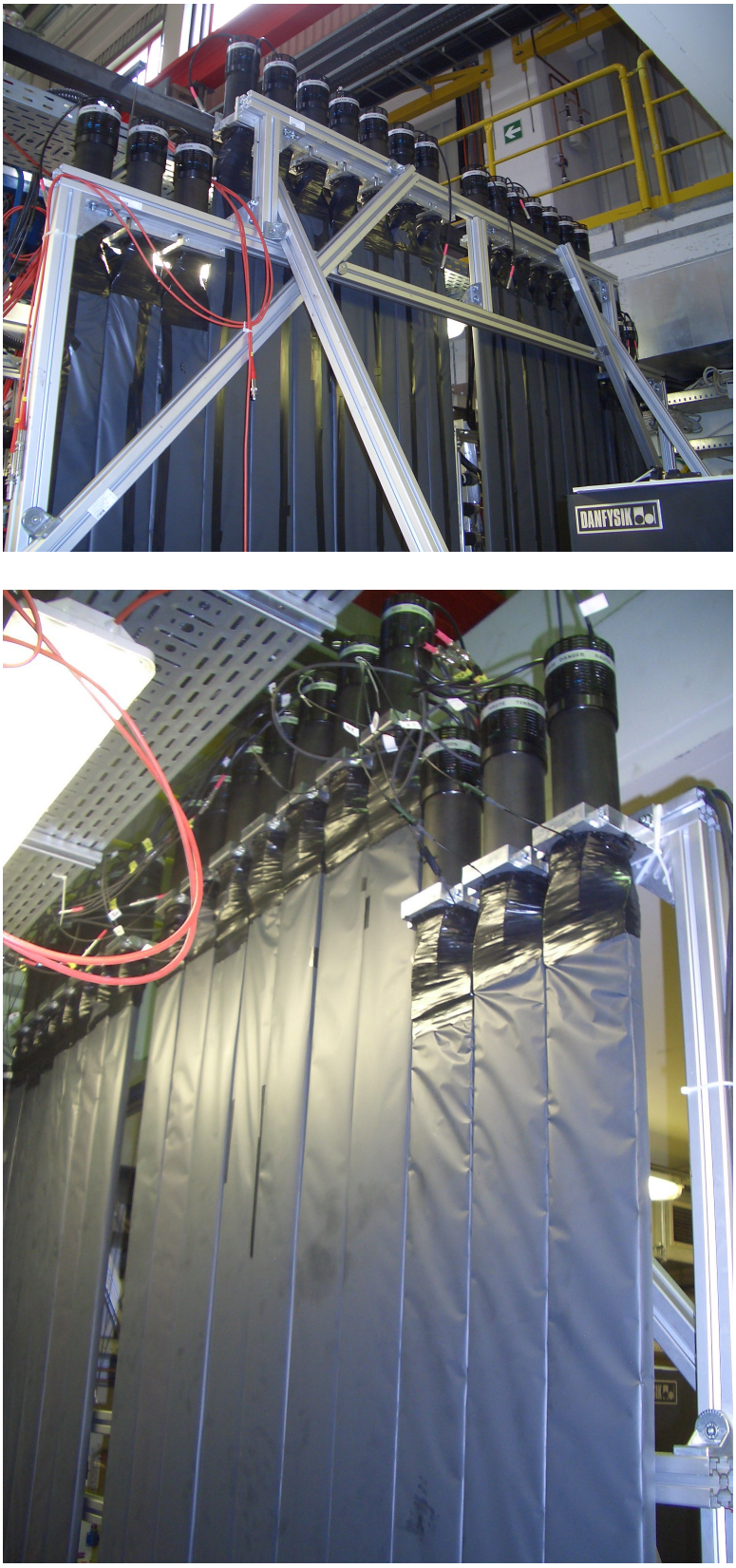

Figure 6.6: Installation of the new FVH. The top photo shows the installed bars with the supporting structure. On the bottom picture one can see the plastic scintillator bars together with light guides and photomultiplier tubes.

Chapter 7

Summary

The first exclusive and kinematically complete measurements of the most basic fusion reaction $pn \rightarrow d\pi^0\pi^0$ at two energies $T_p = 1.03$ GeV and $T_p = 1.35$ GeV are presented. Contrary to the inclusive measurements our data show a large enhancement only at low $\pi\pi$ invariant mass and do not exhibit any high-mass enhancement.

The observed $\pi^0\pi^0$ low-mass enhancement is much larger than predicted in previous $\Delta\Delta$ calculations. The conventional $\Delta\Delta$ calculations, which show good agreement with inclusively measured data, are not able to describe the exclusive data.

The total cross section distribution indicates a resonance-like structure, which is much larger and narrower than expected from the conventional $\Delta\Delta$ excitation.

Hence for the explanation of the data a s-channel resonance with mass $M_R \approx 2.36$ GeV and width $\Gamma \approx 80$ MeV is proposed. With this ansatz we obtain a good description of the $pn \rightarrow d\pi^0\pi^0$ total cross section as well as of the differential cross sections.

With the WASA Detector meanwhile the ABC effect has been observed in the double-pionic fusion reactions: $pn \rightarrow d\pi^0\pi^0$, $pd \rightarrow {}^3He\pi^0\pi^0$ and $dd \rightarrow {}^4He\pi^0\pi^0$.

Since inclusive measurements of the double-pionic fusion to ${}^3He$ and ${}^4He$ [Ban73a, Ban76] also indicate a resonance-like structure in the energy dependance of the ABC-effect, there is evidence that this resonance is robust enough to persist also in heavy nuclei.

The energy dependence of these double-pionic fusion reactions has meanwhile been measured at WASA@COSY with high accuracy. The analysis of these data is subject of the dissertations of A. Pricking and E. Perez del Rio [Pri, Per].

Chapter 8

Outlook

After the movement of the WASA Detector to the COSY Ring in Jülich and successfully mounting and update, a large amount of a new data has been taken.

In 2007 exclusive measurements at COSY of the reaction $pn \rightarrow d\pi^0\pi^0$ have been performed with two orders of magnitude higher statistics compared to the measurements at CELSIUS/WASA. The reaction was measured at 5 energies: 1.0-1.4 GeV to fullfill several conditions:

- cover the full resonance region of the CELSIUS/WASA data
- overlap between different energies due to Fermi motion
- reduce systematical errors

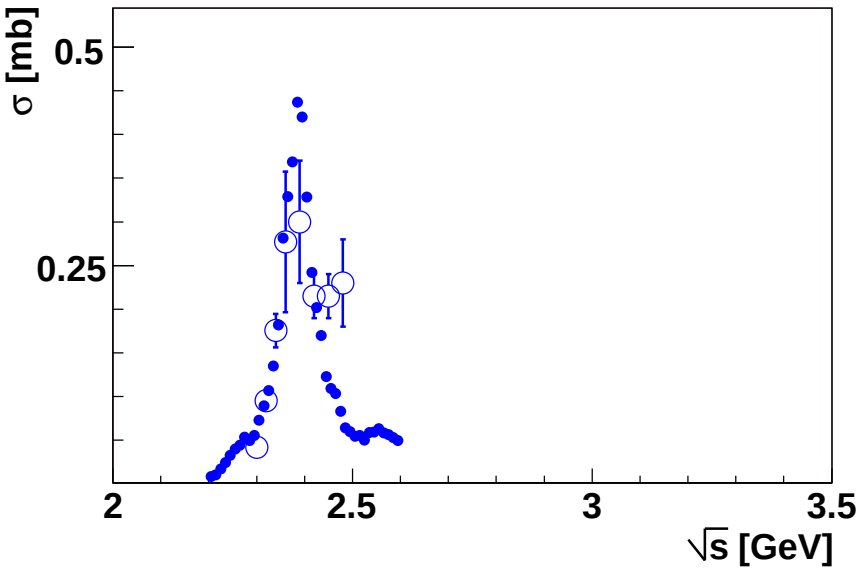

Figure 8.1: Energy dependence of the total cross section for the $pn \rightarrow d\pi^0\pi^0$ reaction. The CELSIUS/WASA data (blue open dots) are compared to the preliminary WASA@COSY data (blue solid dots).

The data at $T_p = 1.0$, 1.1 and 1.3 GeV were already analysed. Fig. 8.1 shows the energy dependence of the total cross section for the reaction $pn \to d\pi^0\pi^0$.

The results of CELSIUS/WASA data (blue open points) are compared to the preliminary results of WASA@COSY data (blue solid points) [Bash08d]. The WASA@COSY data are in a good agreement with the CELSIUS/WASA data. For $\sqrt{s} \approx 2.5$ GeV the CELSIUS/WASA data show some discrepancy between the WASA@COSY data, which might be associated with the low statistics of the CELSIUS data. For the future it will be also interesting to perform measurements with heavier nuclei in the final state, e.g. oxygen.

Chapter 9

Acknowledgments

At the end of this work I would like to thanks all people, who in some way or other helped me during my PhD time in Tübingen.

First of all I am grateful to my supervisor Prof. Heinz Clement for his great support, encouragement and patience in any situation, particular during the final period. For many stimulations and suggestions for analysis improvement at the weekly thursday meetings and detailed explanations in physics. For unforgettable conference trips.

I want to thank:

- TSL crew: Hans Calén, Andrzej Kupść, Kjell Fransson, Jósef Złomańczuk, Marek Jacewicz, Bo Höistad, Magnus Wolke and many others for the technical support during the beam times, interesting disscusions and good ideas concerning my analysis
- to Catharina Åsbjörk for always good organisation and pleasant stays in Uppsala
- to Mikhail Bashkanov, who had always time for me, Tatiana Skorodko and Eugeny Doroshkevich for helpful hints regarding this thesis and also for the russian cheerful atmosphere
- to Tübinger colleagues, especially to Prof. G.J. Wagner, Murat Kaskulov and all who helped my by the understanding and data analysis
- to our workgroup for giving me help by solvig a problems and making my time in Tübingen memorable
- to my mother who always trusted me during my university career

Appendix A

Acronyms

ADC	Analog-to-Digital Converter
CD	Central Detector
CDC	charged track in Central Detector
CDN	neutral track in Central Detector
CELSIUS	Colling with Electrons and Storing of Ions from Uppsala Synchrocyclotron
CERN	Conseil Europ*é*en pour la Recherche Nucl*é*aire
COSY	Cooler Synchrotron
DAQ	Data Acquisition System
FD	Forward Detector
FDC	charged track in Forward Detector
FHD	Forward Hodoscope
FDN	neutral track in Forward Detector
FPC	Forward Proportional Chamber
FRA	Forward Range Absorber
FRH	Forward Range Hodoscope
FRI	Forward Range Intermediate Hodoscope
FSI	Final State Interaction
FTH	Forward Trigger Hodoscope
FVH	Forward Veto Hodoscope
FWC	Forward Window Counter
FWHM	Full Width at Half Maximum
GEANT	GEometry ANd Tracking
IM	Invariant Mass
MM	Missing Mass
MDC	Mini Drift Chamber
PDG	Particle Data Group
PS	Phase Space
PM	Photomultiplier
PMT	Photomultiplier Tube
PS	Plastic Scintillator

PSB	Plastic Scintillator Barrel, backward part
PSC	Plastic Scintillator Barrel, central part
PSF	Plastic Scintillator Barrel, forward part
QCD	Quantum Chromo Dynamics
QDC	charge (Q) Analog-to-Digital Converter
SAID	Scattering Analysis Interactive Dialin
SM	Spectator Model
SCS	Superconducting Solenoid
SEB	Scintillator Electromagnetic Calorimeter, backward part
SEC	Scintillator Electromagnetic Calorimeter, central part
SEF	Scintillator Electromagnetic Calorimeter, forward part
TDC	Time-to-Digital Converter
TSL	The Svedberg Laboratory
WASA	Wide Angle Shower Apparatus
ZEL	Zentrallabor für Elektronik

Appendix B

Uncorrected differential cross sections

In this chapter the raw uncorrected differential cross section distributuions for reaction $pn \rightarrow d\pi^0\pi^0$ at $T_p = 1.03$ GeV and $T_p = 1.35$ GeV are presented. The experimental data, denoted by black points, are compared to the model calculations, which are passed through the simulated detector (MC simulation) and finally analysed with the same conditions as the real data. The describtion of the model calculation used for data comparison can be found in the Chap. 5.3.2.

B.1 Invariant masses

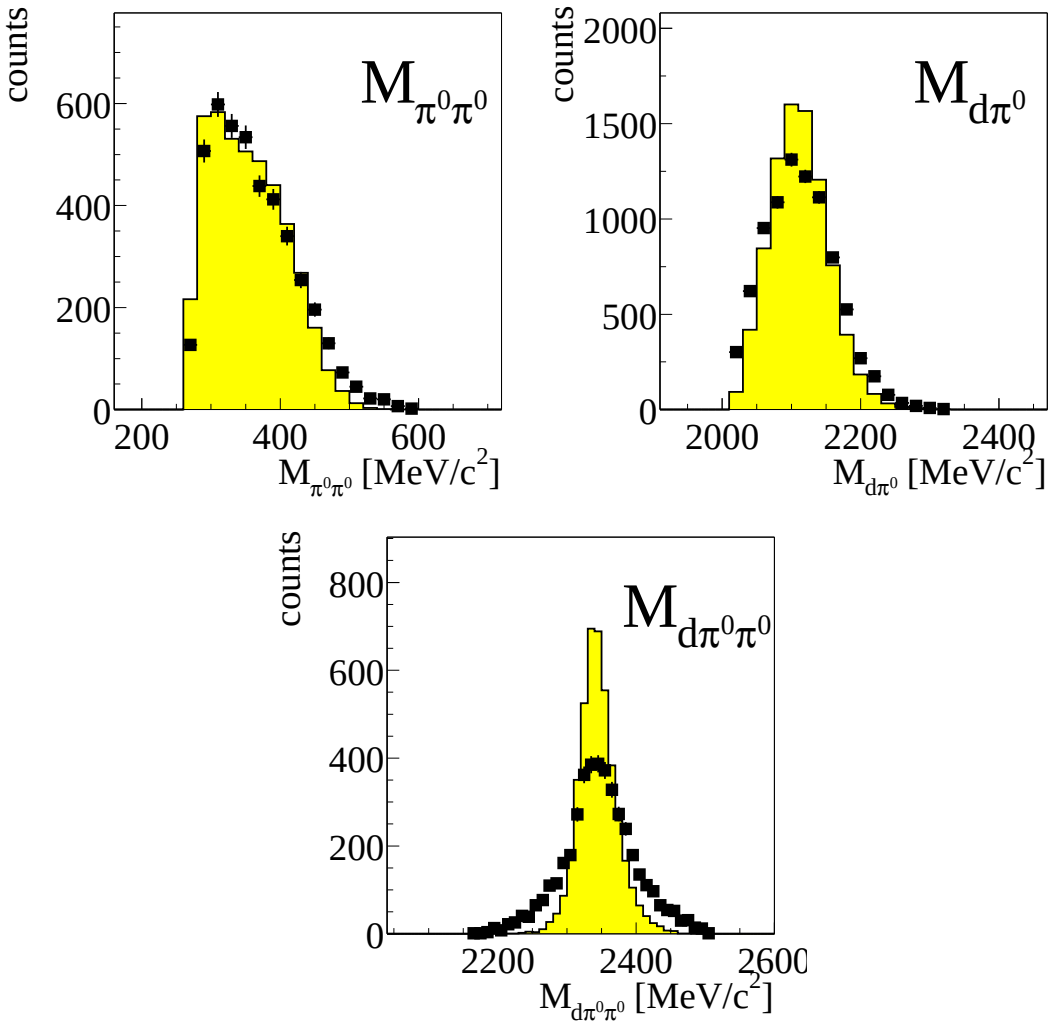

Figure B 1.1: Invariant masses $M_{\pi^0\pi^0}$, $M_{d\pi^0}$ and $M_{d\pi^0\pi^0}$ at $T_p = 1.03$ GeV. Uncorrected data (black points) are compared to the Monte Carlo through detector data (yellow filled area). Monte Carlo data are simulated according to the model described in Chap. 5.3.2.

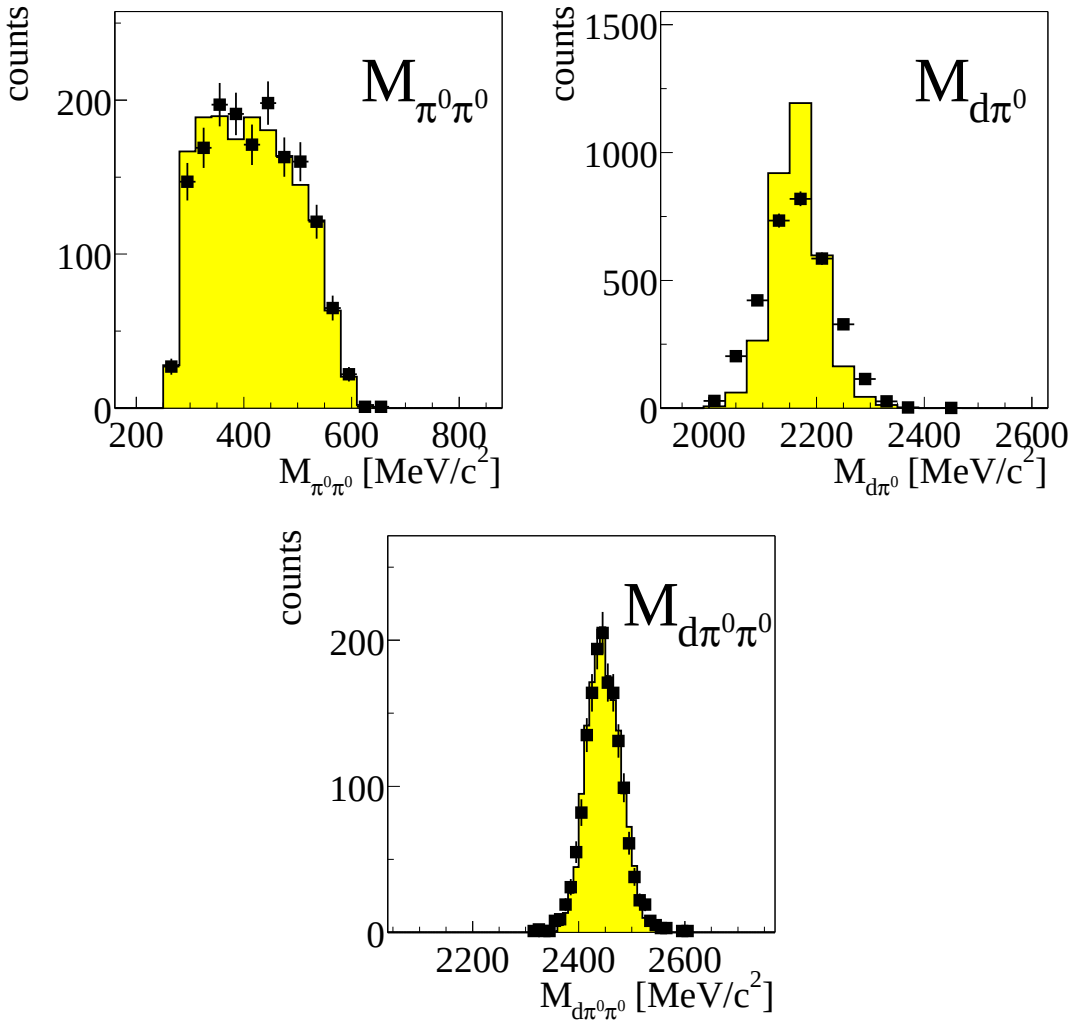

Figure B 1.2: Invariant masses $M_{\pi^0\pi^0}$, $M_{d\pi^0}$ and $M_{d\pi^0\pi^0}$ at $T_p = 1.35$ GeV. Uncorrected data (black points) are compared to the Monte Carlo through detector data (yellow filled area). Monte Carlo data are simulated according to the model described in Chap. 5.3.2.

B.2 Angular distributions

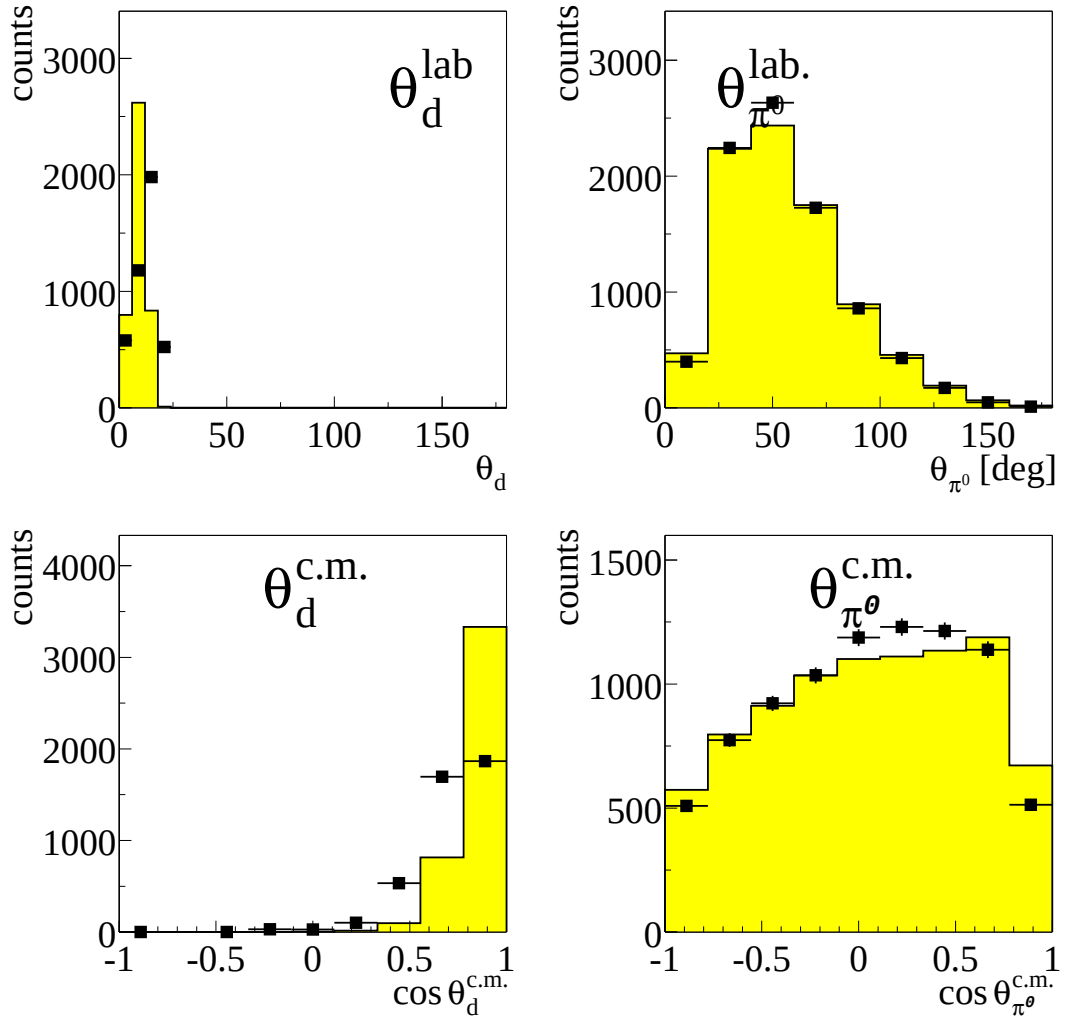

Figure B 2.1: Polar angles in labor and centre of mass systems at $T_p = 1.03$ GeV. Uncorrected data (black points) are compared to the Monte Carlo through detector data (yellow filled area). Monte Carlo data are simulated according to the model described in Chap. 5.3.2.

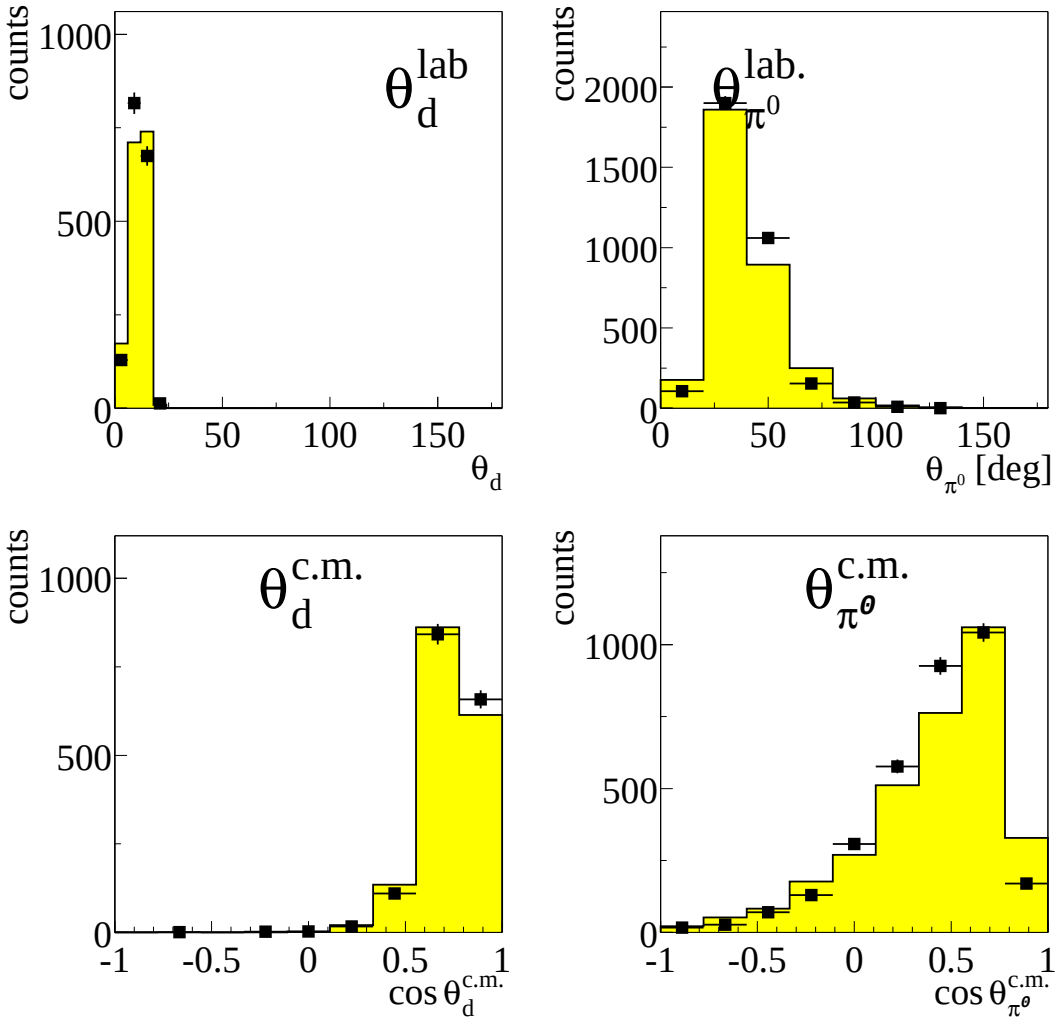

Figure B 2.2: Polar angles in labor and centre of mass systems at $T_p = 1.35$ GeV. Uncorrected data (black points) are compared to the Monte Carlo through detector data (yellow filled area). Monte Carlo data are simulated according to the model described in Chap. 5.3.2.

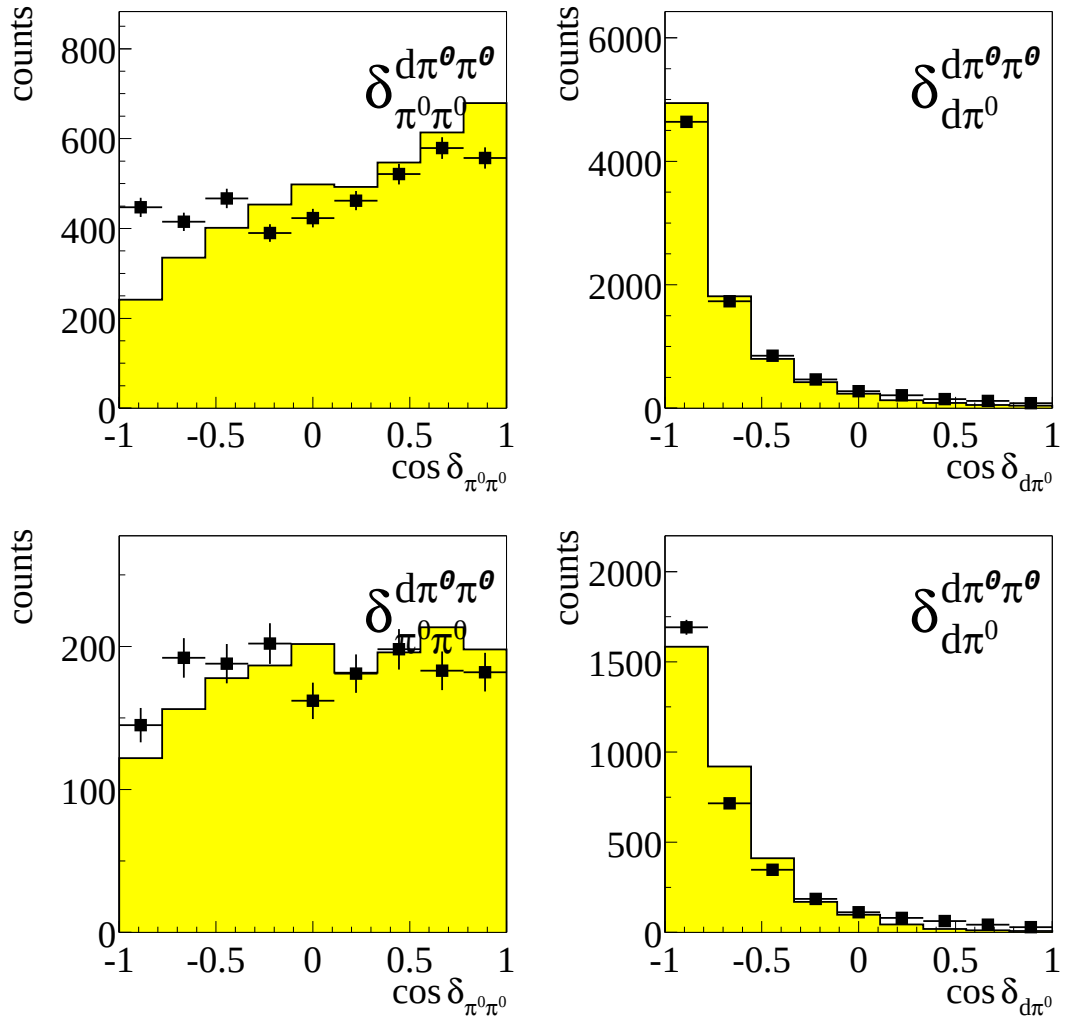

Figure B 2.3: Opening angles in $d\pi^0\pi^0$ system at $T_p = 1.03$ GeV (top row) and at $T_p = 1.35$ GeV (bottom row).
Uncorrected data (black points) are compared to the Monte Carlo through detector data (yellow filled area). Monte Carlo data are simulated according to the model described in Chap. 5.3.2.

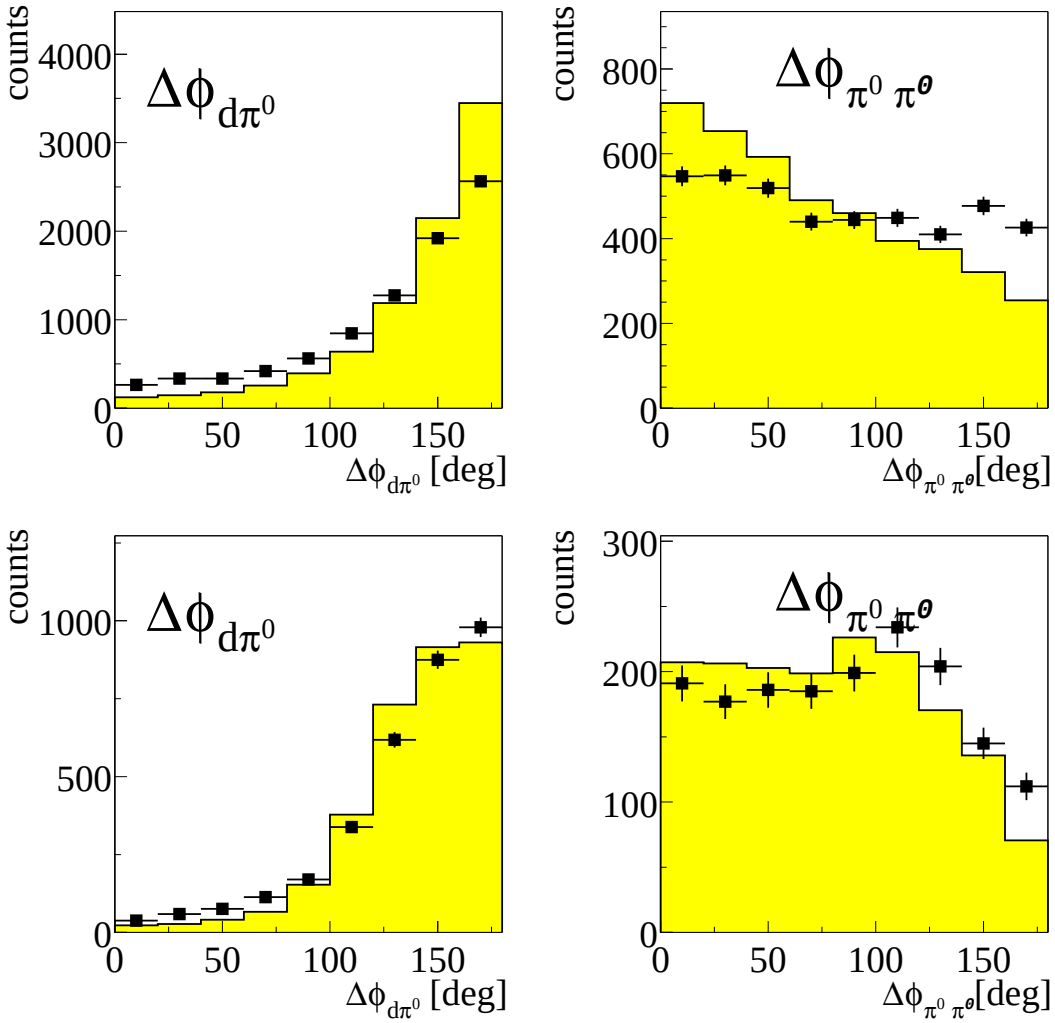

Figure B 2.4: Azimuthal angles for planarity between deuteron and pion (left) and between pions (rigtht) at $T_p = 1.03$ GeV (top row) and at $T_p = 1.35$ GeV (bottom row).
Uncorrected data (black points) are compared to the Monte Carlo through detector data (yellow filled area). Monte Carlo data are simulated according to the model described in Chap. 5.3.2.

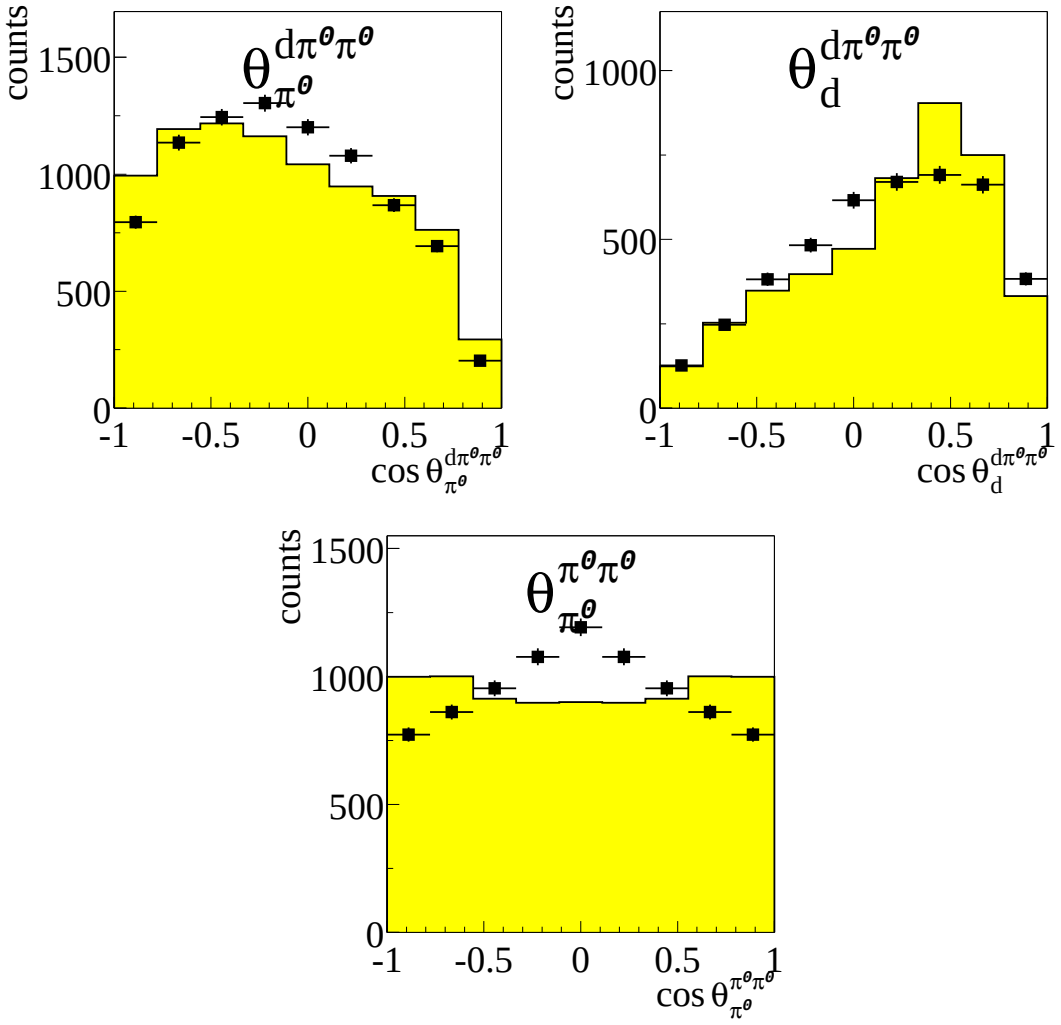

Figure B 2.5: Polar angles of deuteron and pions in different subsystems at $T_p = 1.03$ GeV.
Uncorrected data (black points) are compared to the Monte Carlo through detector data (yellow filled area). Monte Carlo data are simulated according to the model described in Chap. 5.3.2.

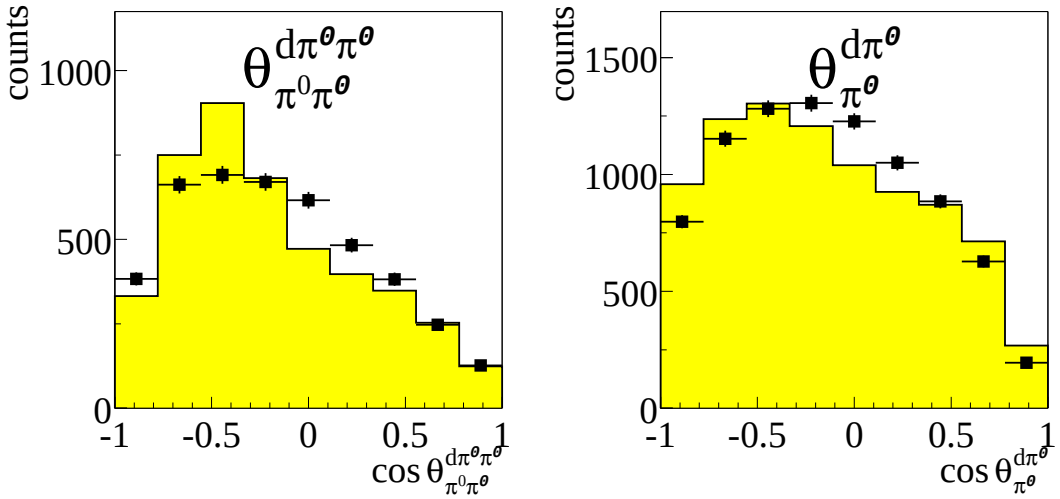

Figure B 2.6: Polar angles of deuteron and pions in different subsystems at $T_p = 1.03$ GeV.
Uncorrected data (black points) are compared to the Monte Carlo through detector data (yellow filled area). Monte Carlo data are simulated according to the model described in Chap. 5.3.2.

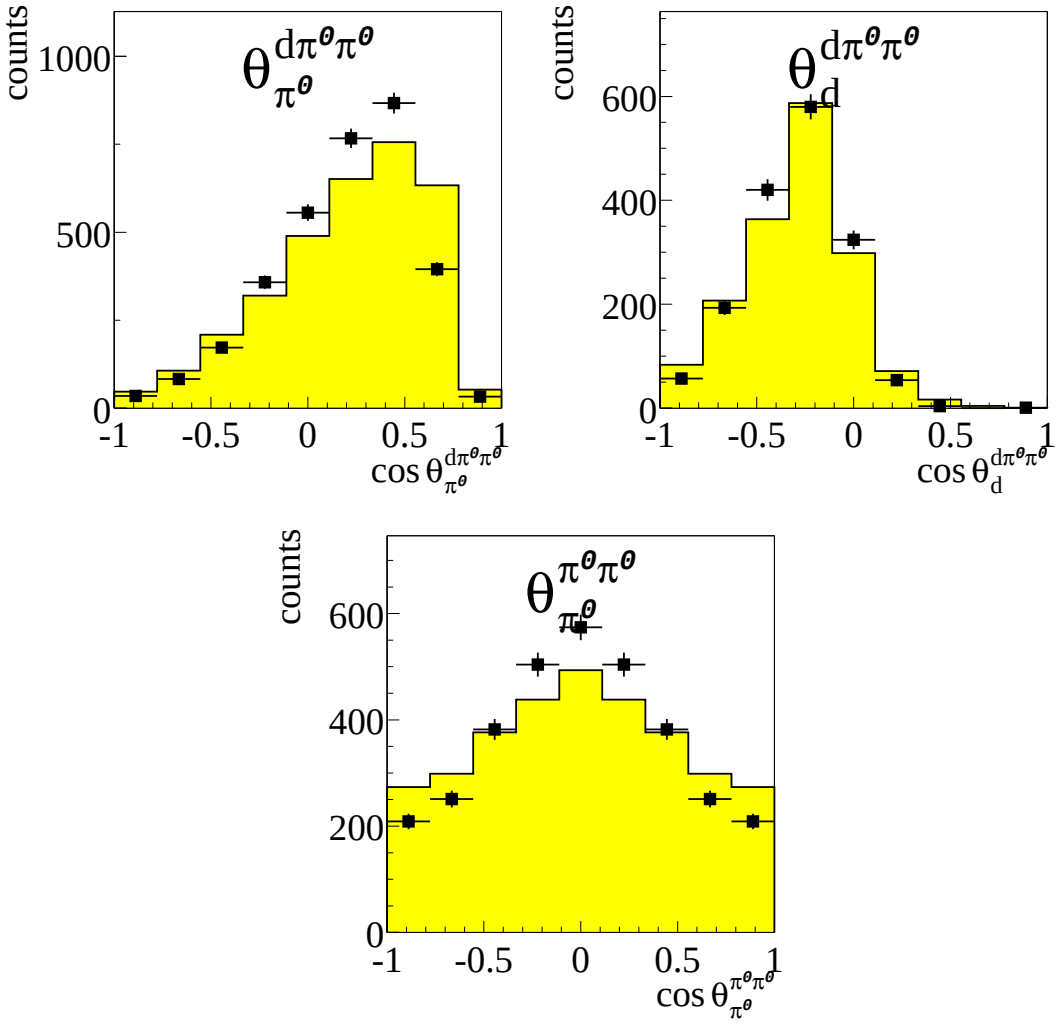

Figure B 2.7: Polar angles of deuteron and pions in different subsystems at $T_p = 1.35$ GeV.
Uncorrected data (black points) are compared to the Monte Carlo through detector data (yellow filled area). Monte Carlo data are simulated according to the model described in Chap. 5.3.2.

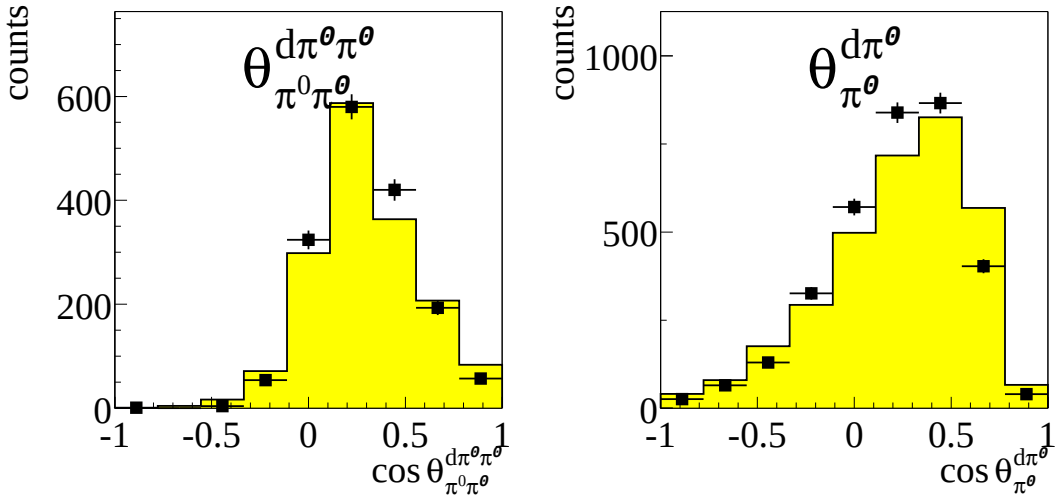

Figure B 2.8: Polar angles of deuteron and pions in different subsystems at $T_p = 1.35$ GeV.
Uncorrected data (black points) are compared to the Monte Carlo through detector data (yellow filled area). Monte Carlo data are simulated according to the model described in Chap. 5.3.2.

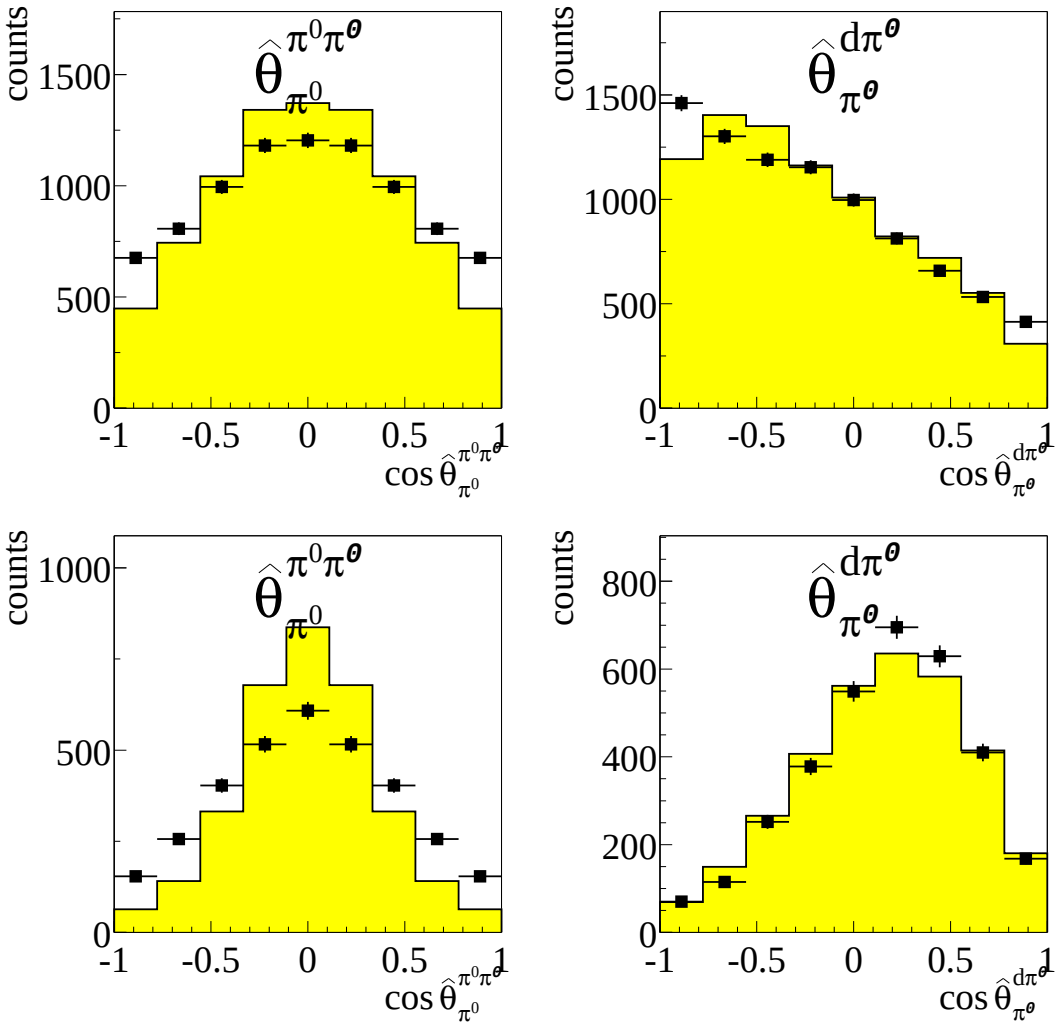

Figure B 2.9: Opening angles of pion in pion-pion and deuteron-pion subsystems at $T_p = 1.03$ GeV (top row) and at $T_p = 1.35$ GeV (bottom row).
Uncorrected data (black points) are compared to the Monte Carlo through detector data (yellow filled area). Monte Carlo data are simulated according to the model described in Chap. 5.3.2.

B.3 Energy distributions

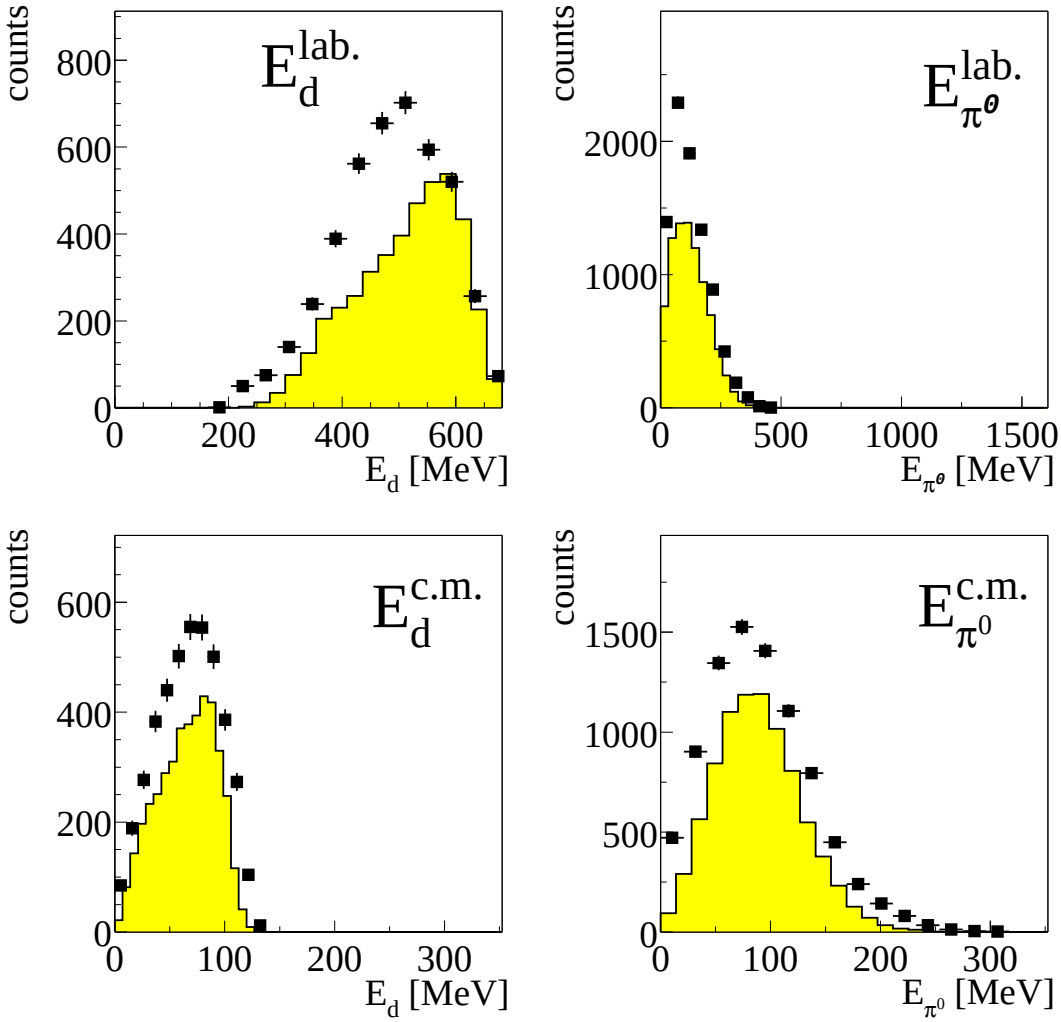

Figure B 3.1: Kinetic energy distributions of deuteron and pions in labor (top row) and centre of mass (bottom row) systems at $T_p = 1.03$ GeV.
Uncorrected data (black points) are compared to the Monte Carlo through detector data (yellow filled area). Monte Carlo data are simulated according to the model described in Chap. 5.3.2.

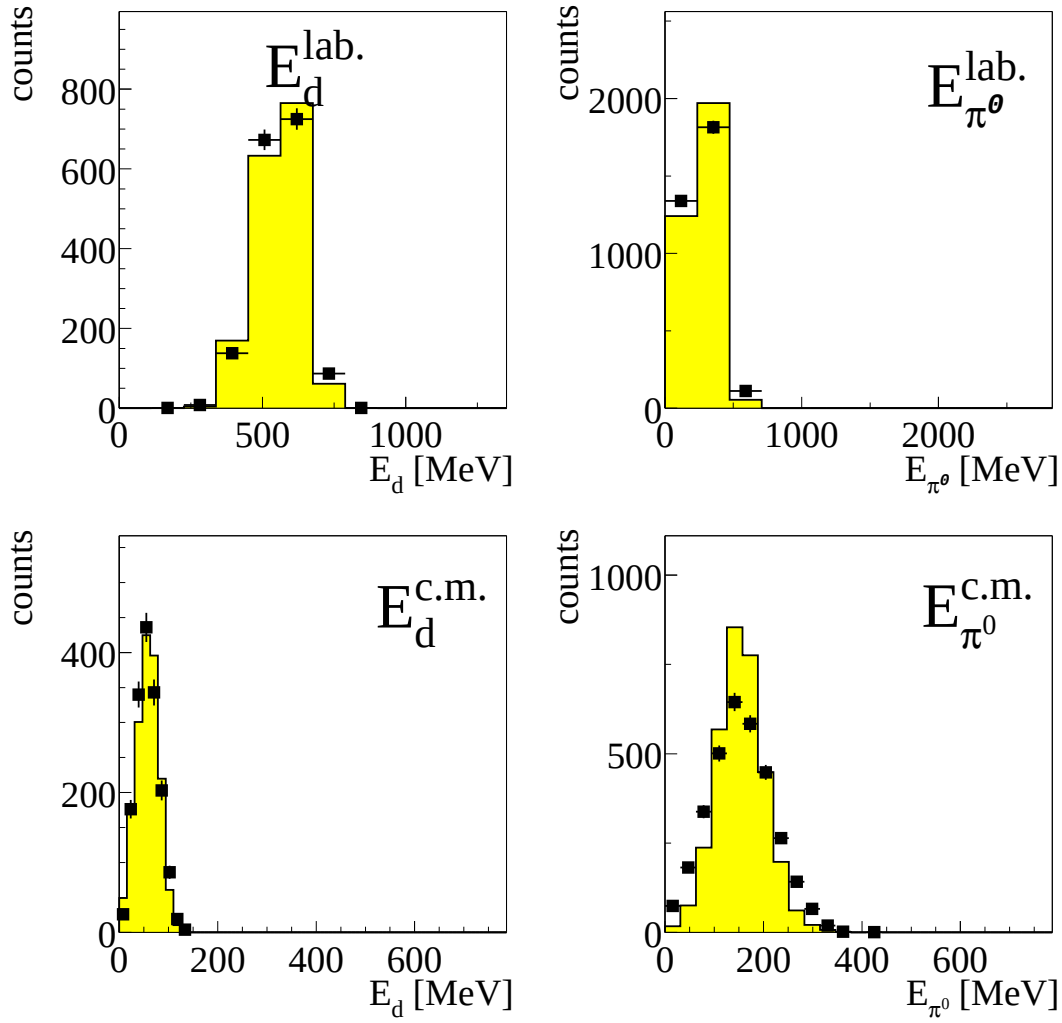

Figure B 3.2: Kinetic energy distributions of deuteron and pions in labor (top row) and centre of mass (bottom row) systems at $T_p = 1.35$ GeV.
Uncorrected data (black points) are compared to the Monte Carlo through detector data (yellow filled area). Monte Carlo data are simulated according to the model described in Chap. 5.3.2.

B.4 Energy and angle distributions of spectator proton

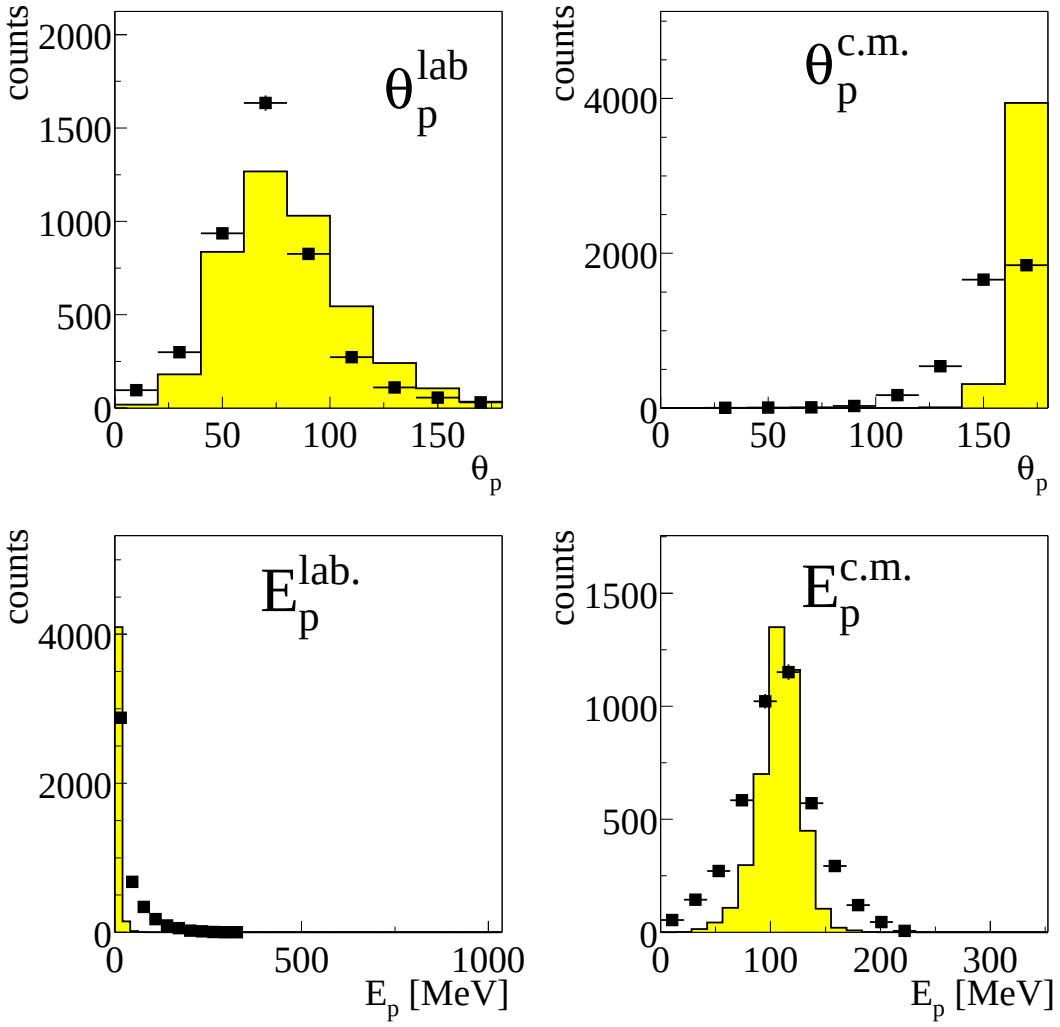

Figure B 4.1: Kinetic energy and angular distributions of spectator proton in labor and centre of mass systems at $T_p = 1.03$ GeV.
Uncorrected data (black points) are compared to the Monte Carlo through detector data (yellow filled area). Monte Carlo data are simulated according to the model described in Chap. 5.3.2.

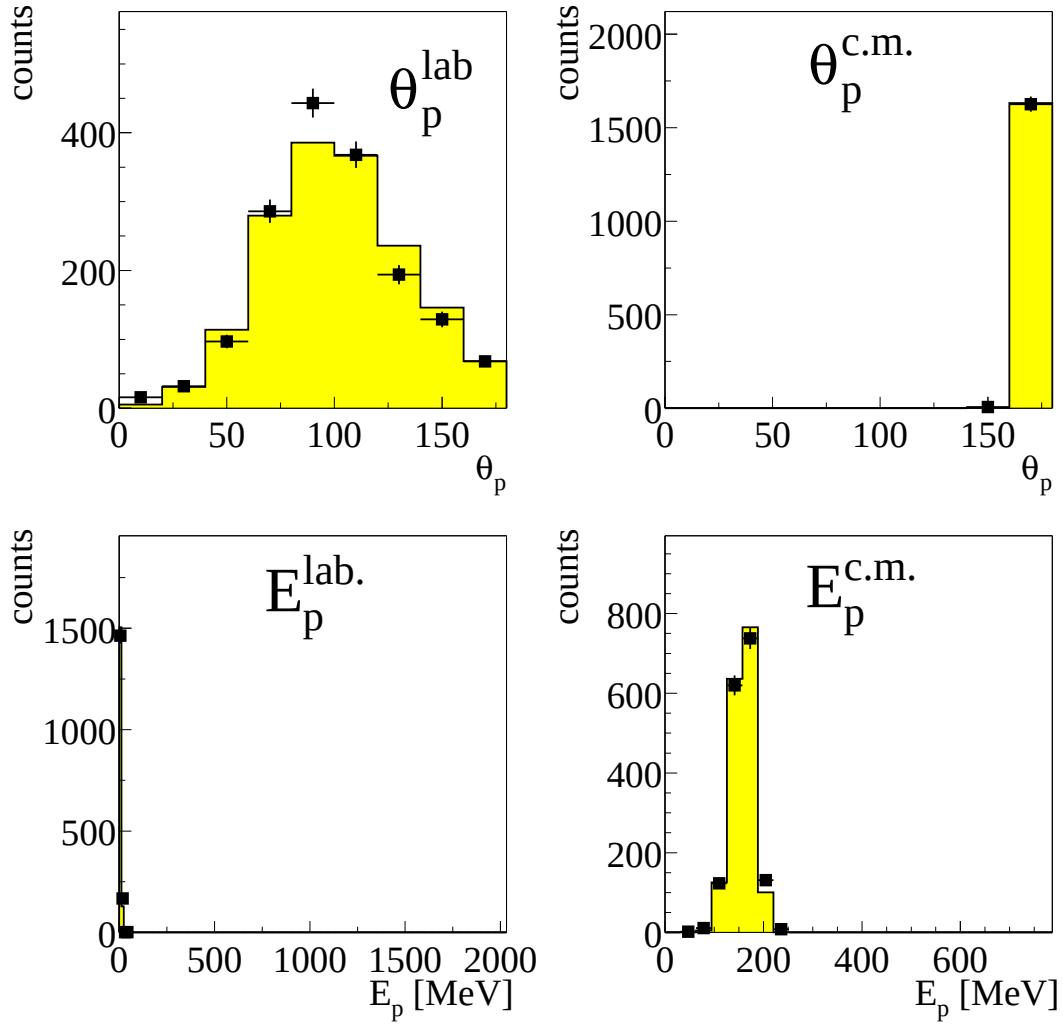

Figure B 4.2: Kinetic energy and angular distributions of spectator proton in labor and centre of mass systems at $T_p = 1.35$ GeV.
Uncorrected data (black points) are compared to the Monte Carlo through detector data (yellow filled area). Monte Carlo data are simulated according to the model described in Chap. 5.3.2.

Appendix C

Corrected differential cross sections

In this chapter the efficiency and acceptance corrected distributions are presented. The data correction was obtained according to the following method:

$$histogram(data\ \ corrected) = histogram(experiment) \cdot \frac{histogram(MC\ \ simulation)}{histogram(model)}$$

C.1 Invariant masses

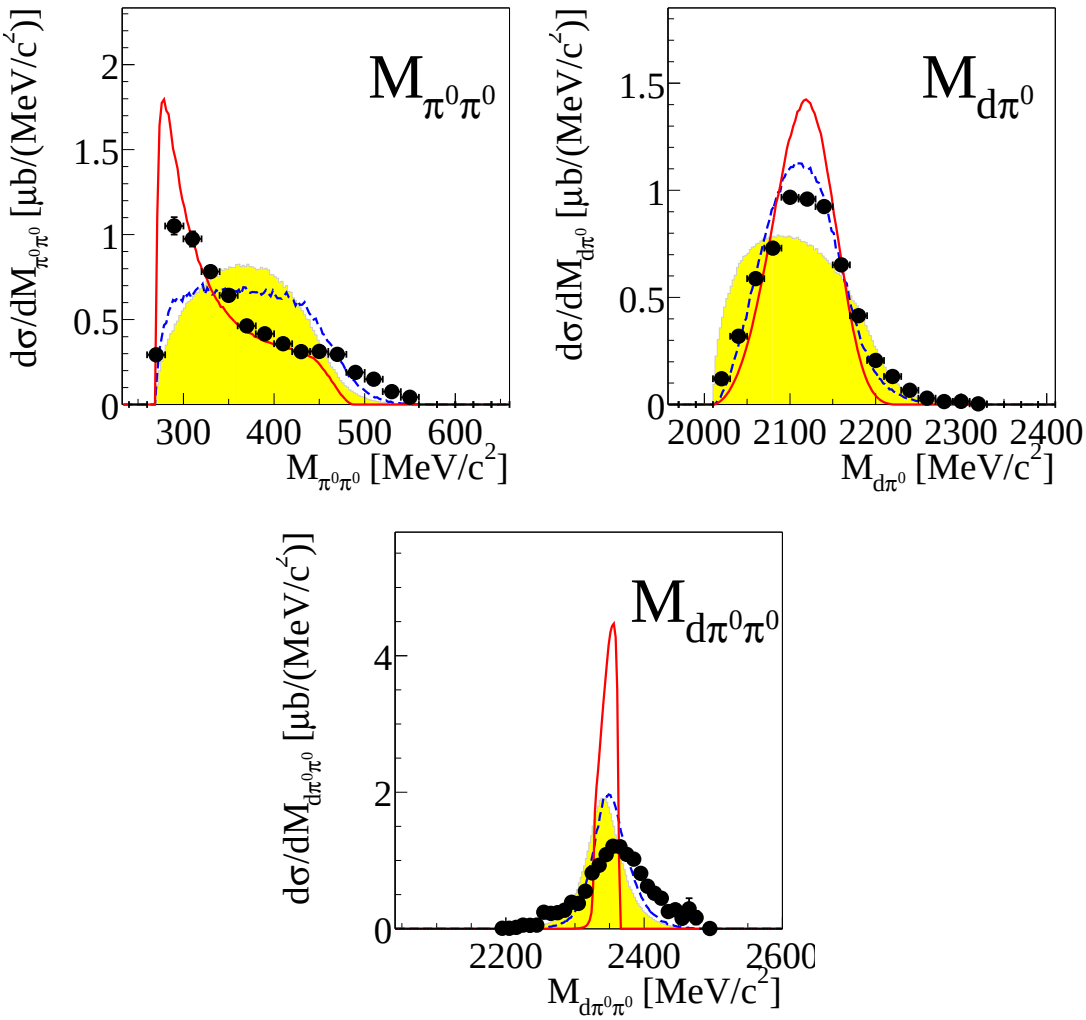

Figure C 1.1: Invariant masses $M_{\pi^0\pi^0}$, $M_{d\pi^0}$ and $M_{d\pi^0\pi^0}$ at $T_p = 1.03$ GeV. Uncorrected data (black points) are compared to the Monte Carlo through detector data (yellow filled area). Monte Carlo data are simulated according to the model described in Chap. 5.3.2.

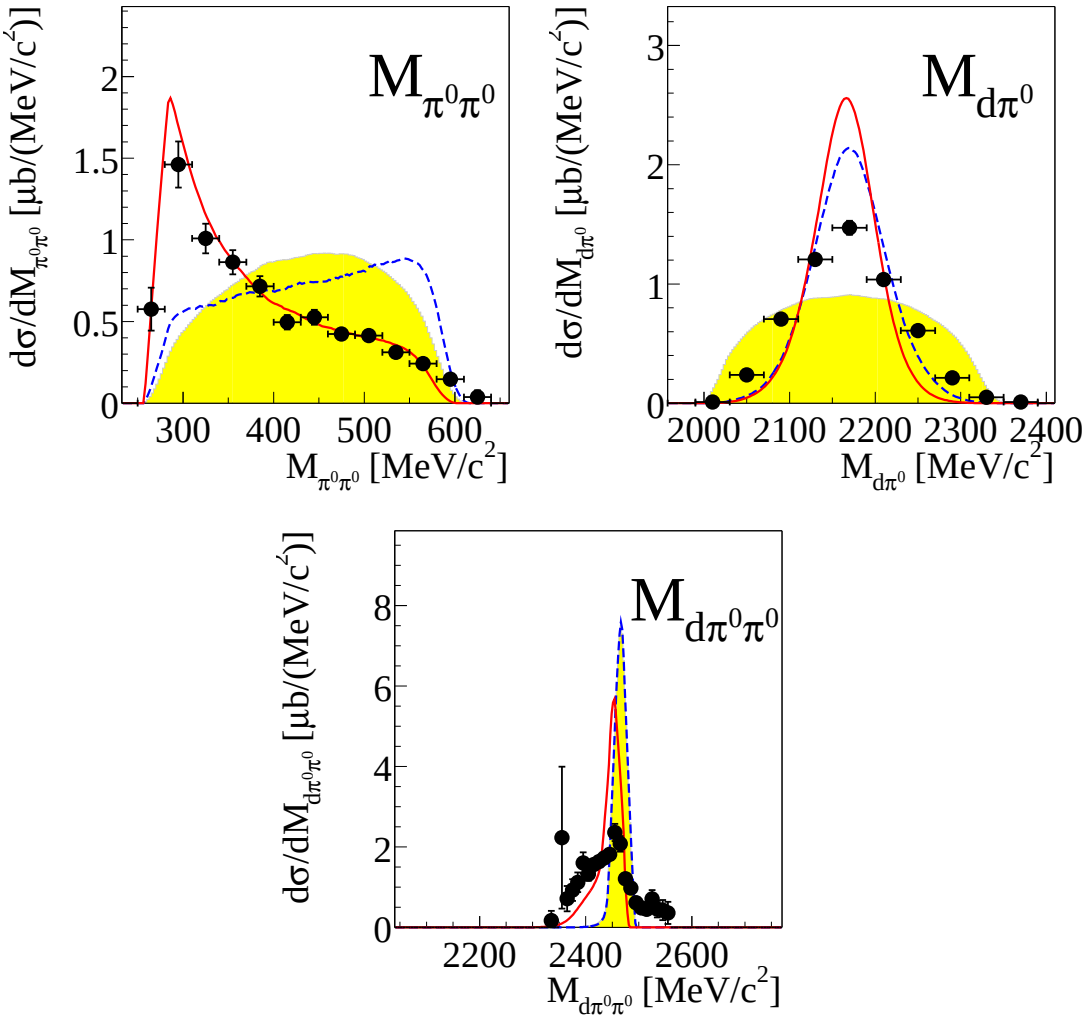

Figure C 1.2: Invariant masses $M_{\pi^0\pi^0}$, $M_{d\pi^0}$ and $M_{d\pi^0\pi^0}$ at $T_p = 1.35$ GeV. Uncorrected data (black points) are compared to the Monte Carlo through detector data (yellow filled area). Monte Carlo data are simulated according to the model described in Chap. 5.3.2.

C.2 Angular distributions

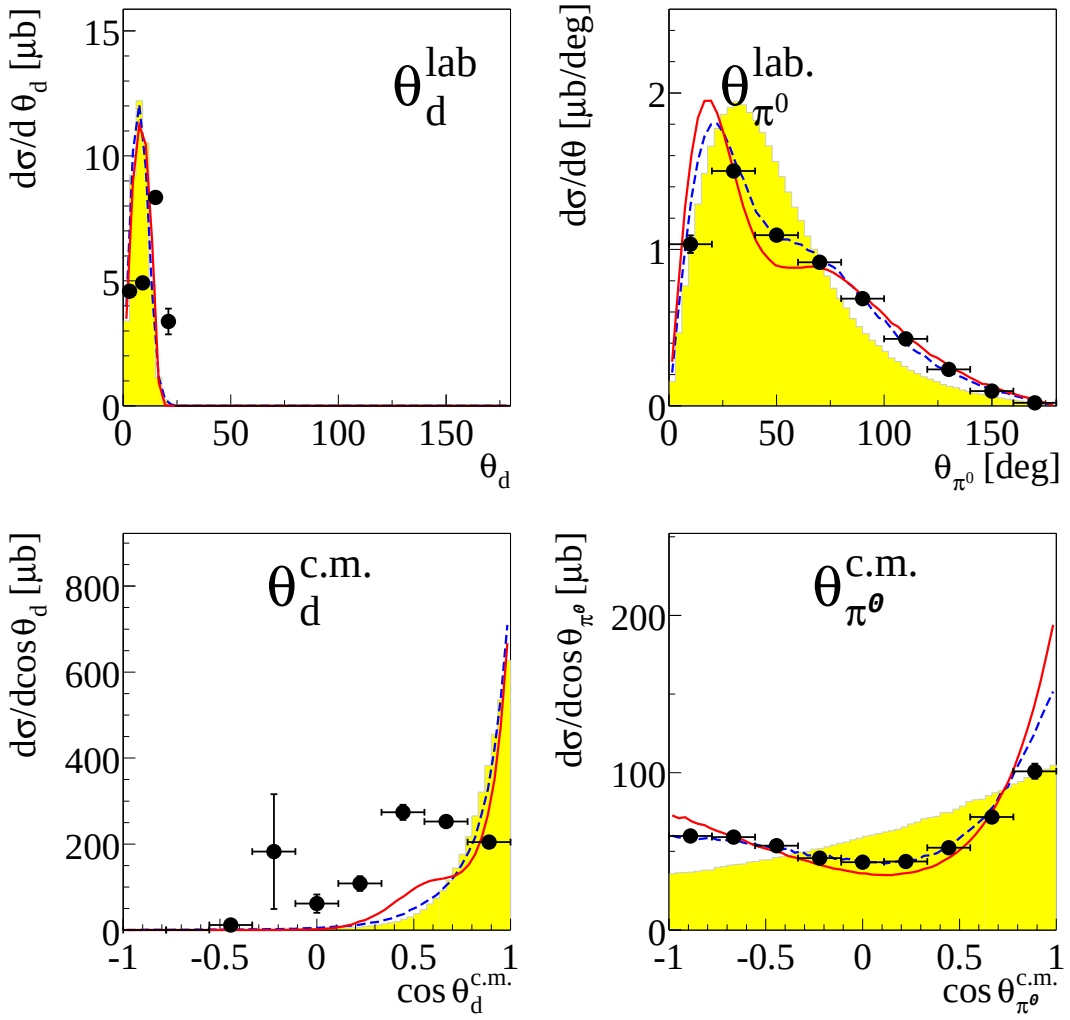

Figure C 2.1: Polar angles in labor and centre of mass systems at $T_p = 1.03$ GeV. Uncorrected data (black points) are compared to the Monte Carlo through detector data (yellow filled area). Monte Carlo data are simulated according to the model described in Chap. 5.3.2.

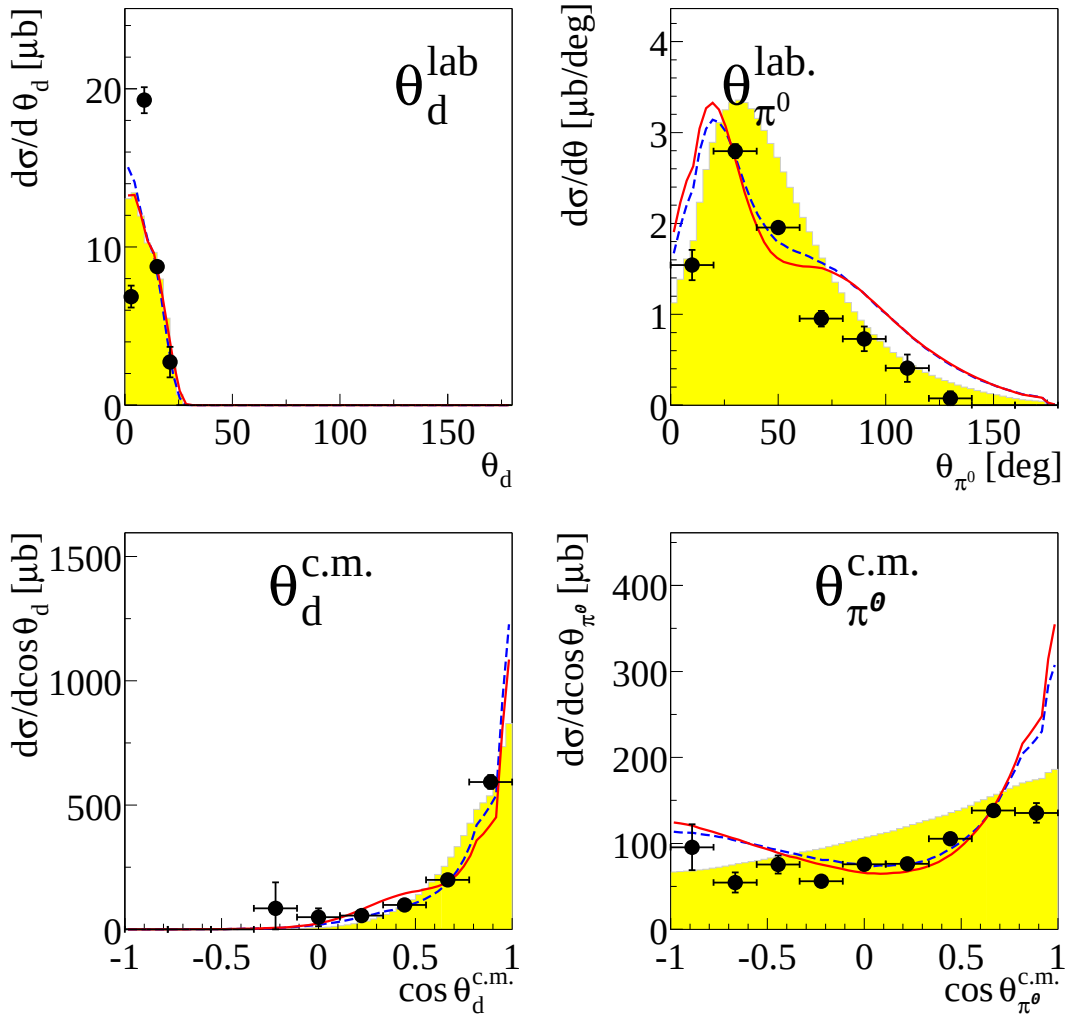

Figure C 2.2: Polar angles in labor and centre of mass systems at $T_p = 1.35$ GeV. Uncorrected data (black points) are compared to the Monte Carlo through detector data (yellow filled area). Monte Carlo data are simulated according to the model described in Chap. 5.3.2.

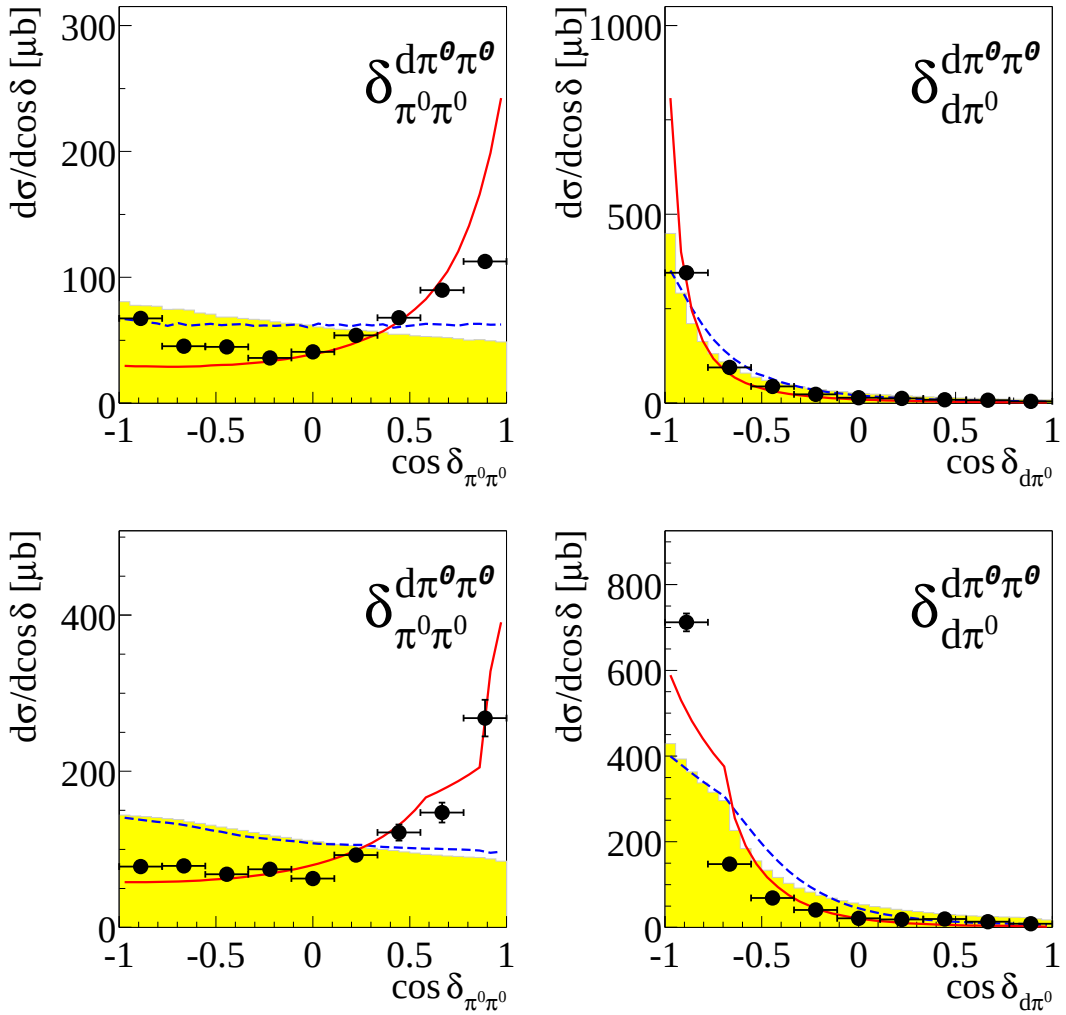

Figure C 2.3: Opening angles in $d\pi^0\pi^0$ system at $T_p = 1.03$ GeV (top row) and at $T_p = 1.35$ GeV (bottom row).
Uncorrected data (black points) are compared to the Monte Carlo through detector data (yellow filled area). Monte Carlo data are simulated according to the model described in Chap. 5.3.2.

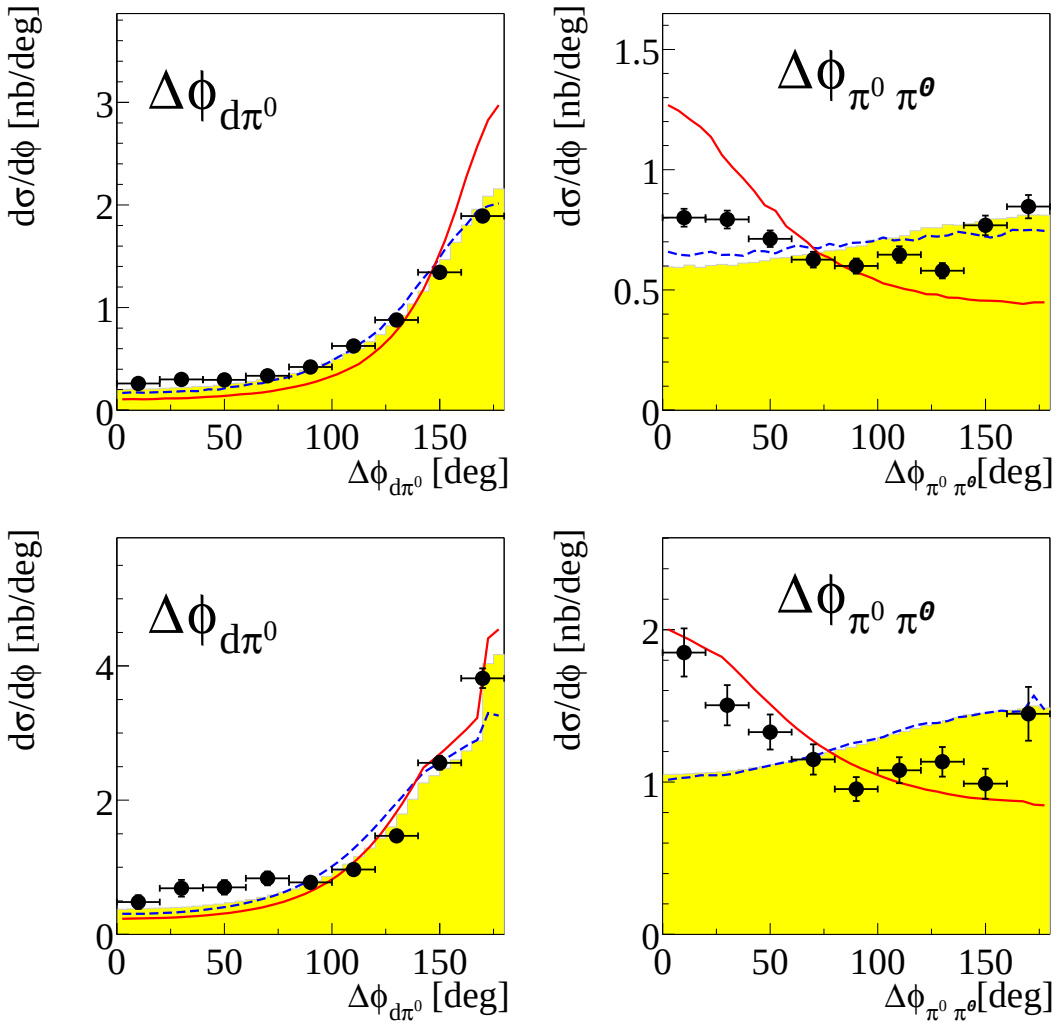

Figure C 2.4: Azimuthal angles for planarity between deuteron and pion (left) and between pions (rigtht) at $T_p = 1.03$ GeV (top row) and at $T_p = 1.35$ GeV (bottom row).
Uncorrected data (black points) are compared to the Monte Carlo through detector data (yellow filled area). Monte Carlo data are simulated according to the model described in Chap. 5.3.2.

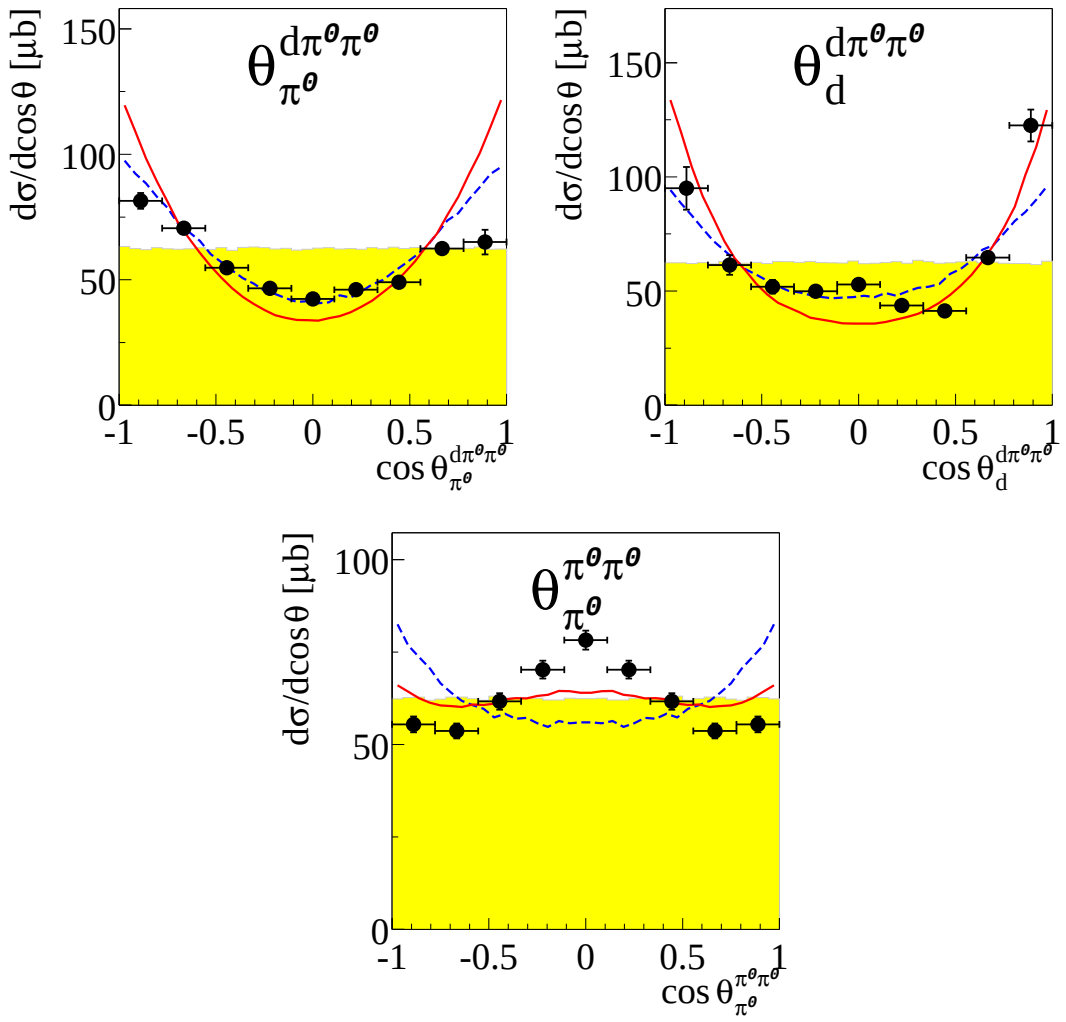

Figure C 2.5: Polar angles of deuteron and pions in different subsystems at $T_p = 1.03$ GeV.
Uncorrected data (black points) are compared to the Monte Carlo through detector data (yellow filled area). Monte Carlo data are simulated according to the model described in Chap. 5.3.2.

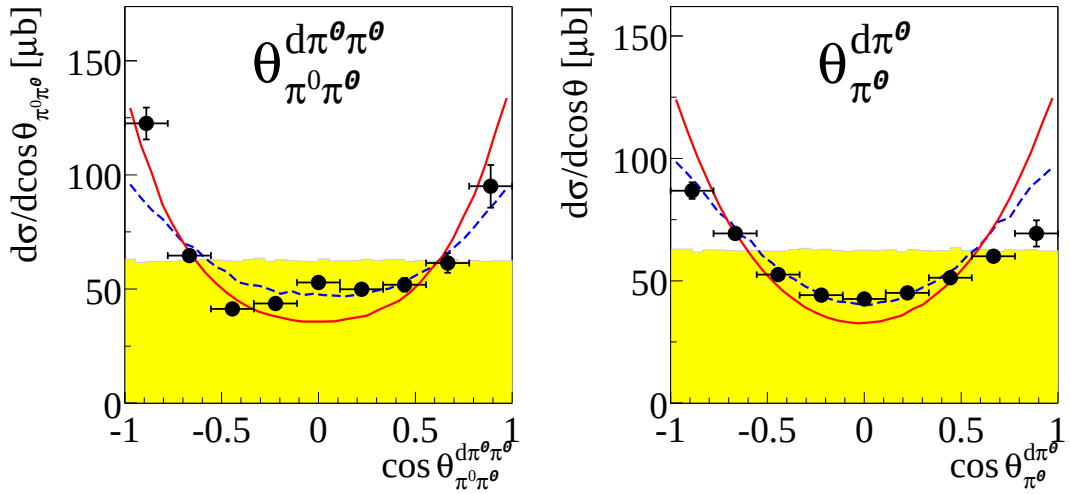

Figure C 2.6: Polar angles of deuteron and pions in different subsystems at $T_p = 1.03$ GeV.
Uncorrected data (black points) are compared to the Monte Carlo through detector data (yellow filled area). Monte Carlo data are simulated according to the model described in Chap. 5.3.2.

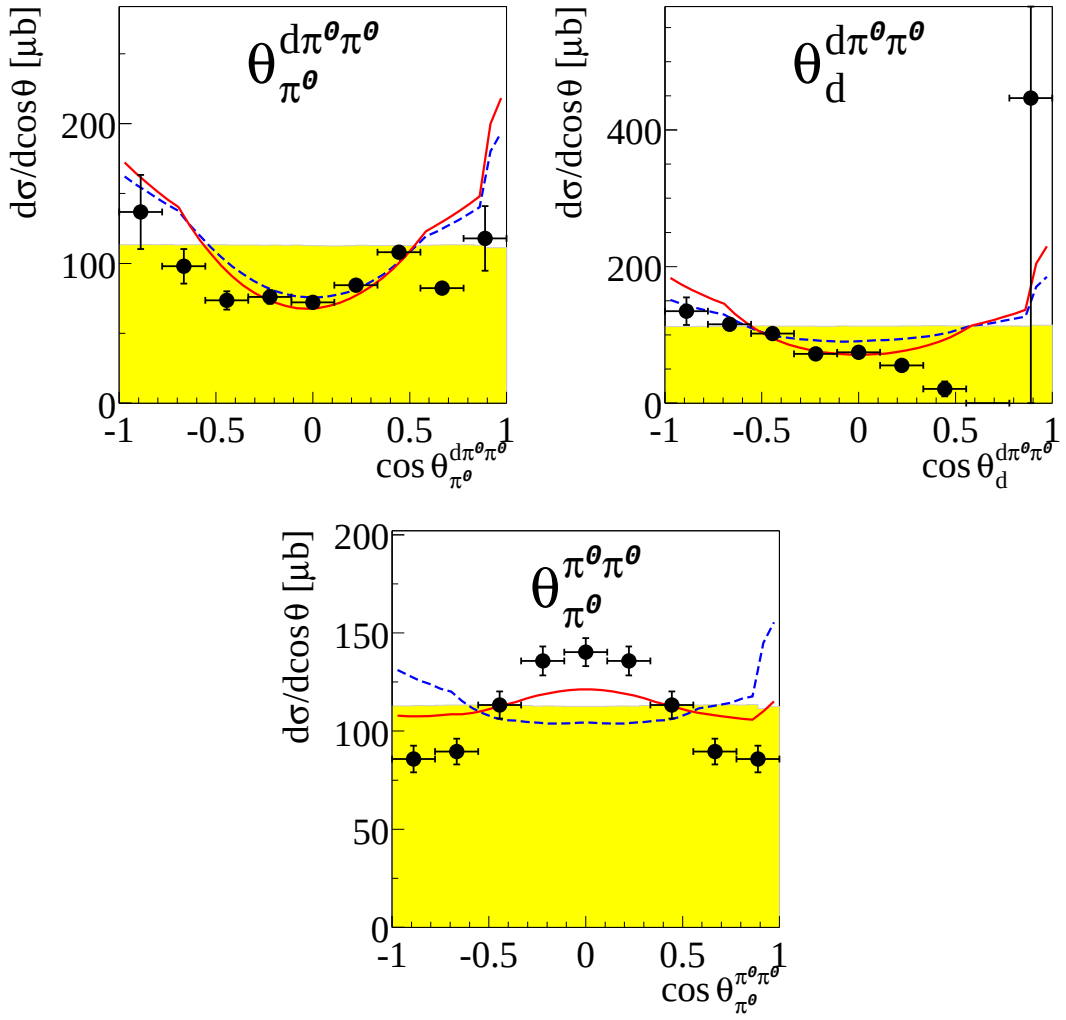

Figure C 2.7: Polar angles of deuteron and pions in different subsystems at $T_p = 1.35$ GeV.
Uncorrected data (black points) are compared to the Monte Carlo through detector data (yellow filled area). Monte Carlo data are simulated according to the model described in Chap. 5.3.2.

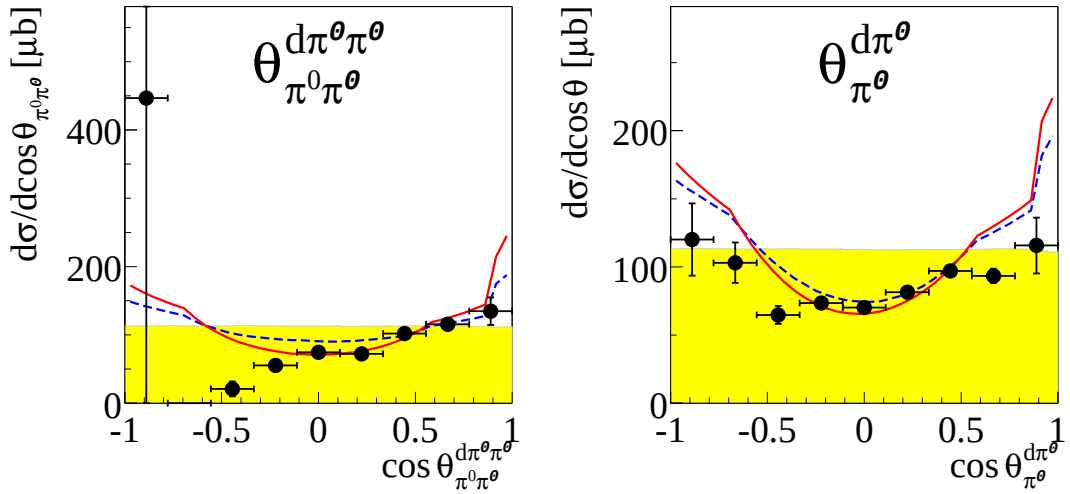

Figure C 2.8: Polar angles of deuteron and pions in different subsystems at $T_p = 1.35$ GeV.
Uncorrected data (black points) are compared to the Monte Carlo through detector data (yellow filled area). Monte Carlo data are simulated according to the model described in Chap. 5.3.2.

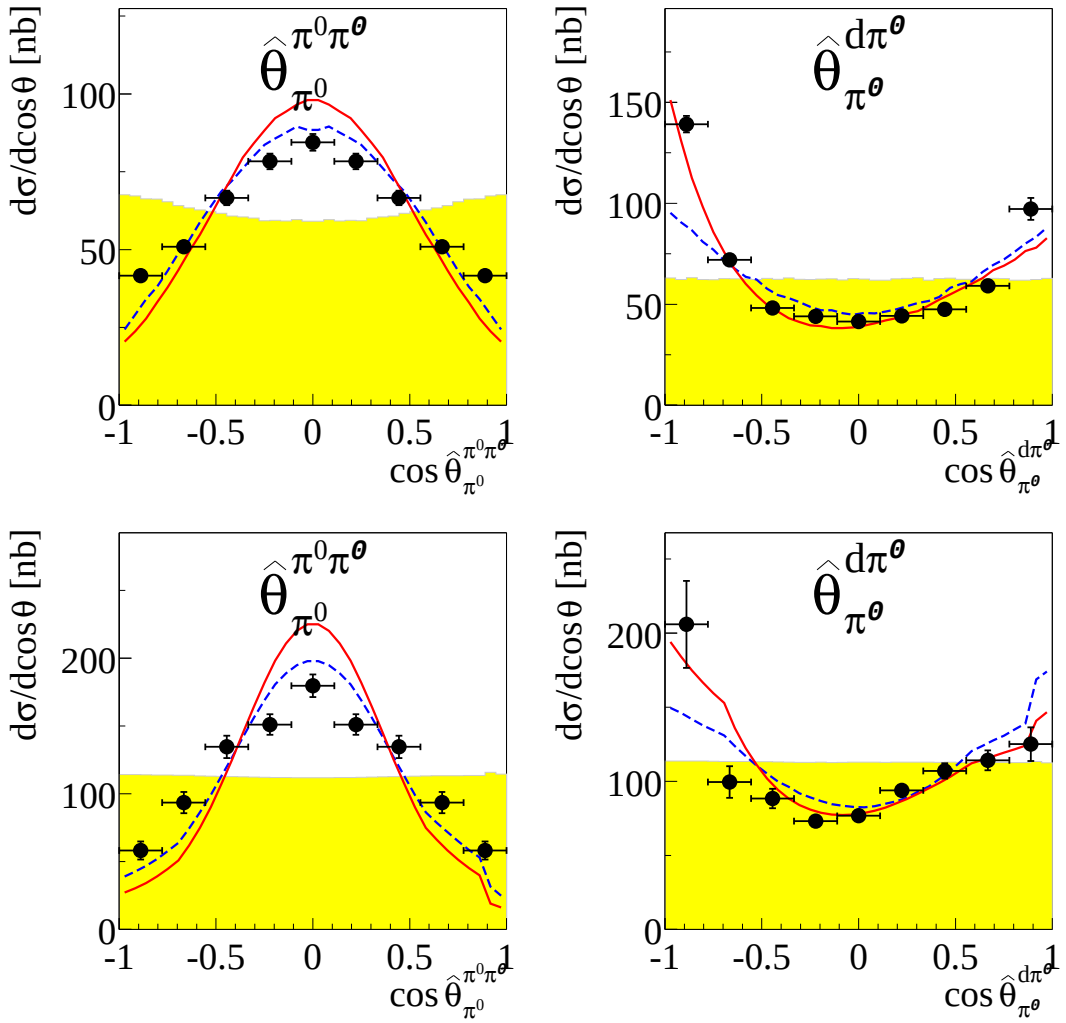

Figure C 2.9: Opening angles of pion in pion-pion and deuteron-pion subsystems at $T_p = 1.03$ GeV (top row) and at $T_p = 1.35$ GeV (bottom row).
Uncorrected data (black points) are compared to the Monte Carlo through detector data (yellow filled area). Monte Carlo data are simulated according to the model described in Chap. 5.3.2.

C.3 Energy distributions

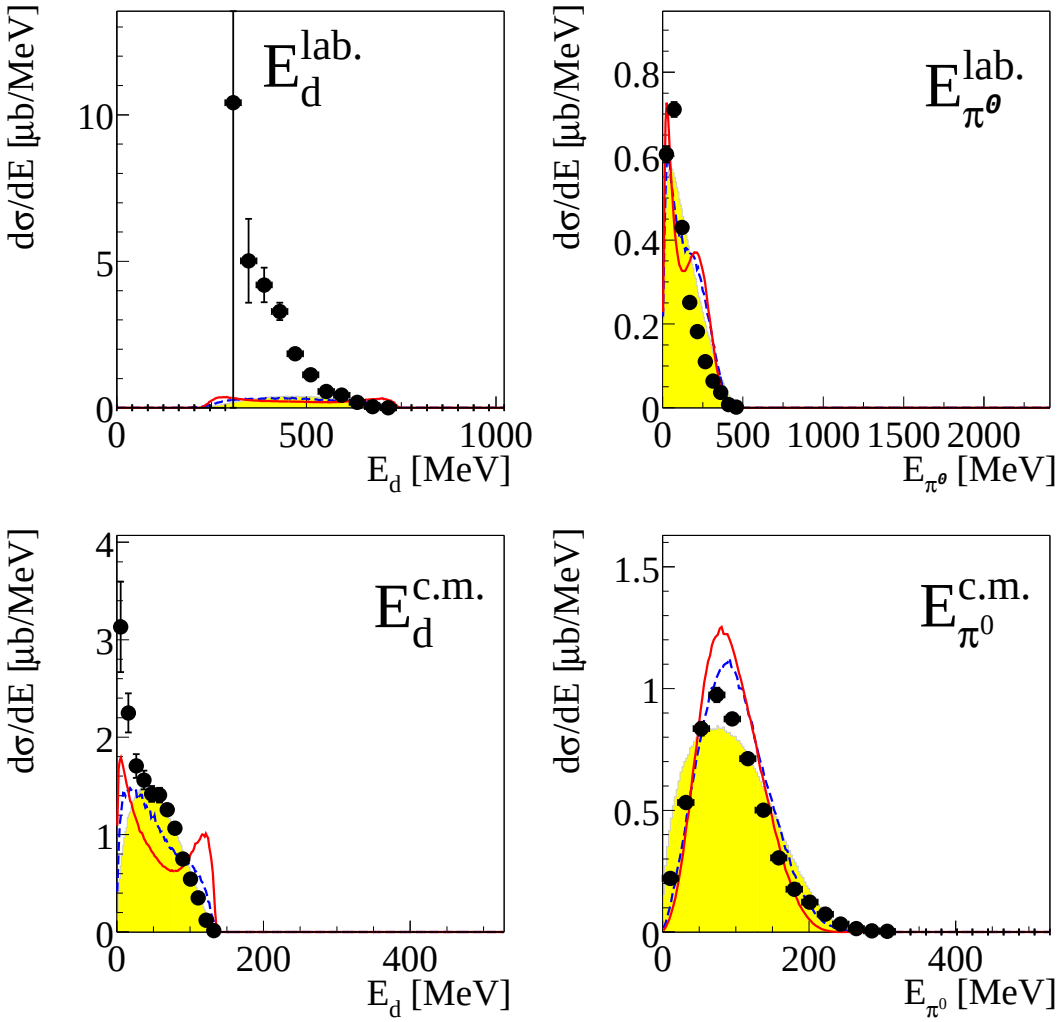

Figure C 3.1: Kinetic energy distributions of deuteron and pions in labor (top row) and centre of mass (bottom row) systems at $T_p = 1.03$ GeV.
Uncorrected data (black points) are compared to the Monte Carlo through detector data (yellow filled area). Monte Carlo data are simulated according to the model described in Chap. 5.3.2.

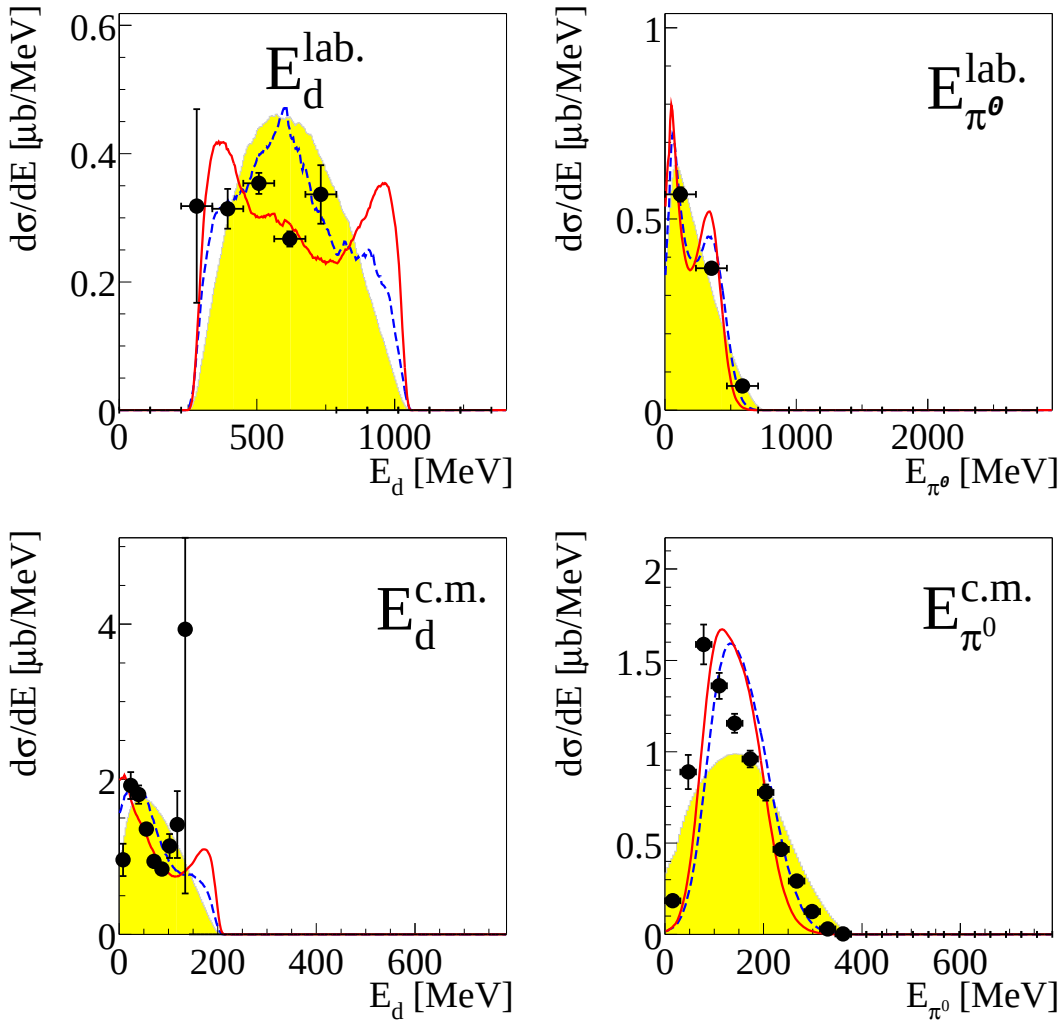

Figure C 3.2: Kinetic energy distributions of deuteron and pions in labor (top row) and centre of mass (bottom row) systems at $T_p = 1.35$ GeV.
Uncorrected data (black points) are compared to the Monte Carlo through detector data (yellow filled area). Monte Carlo data are simulated according to the model described in Chap. 5.3.2.

C.4 Energy and angle distributions of spectator proton

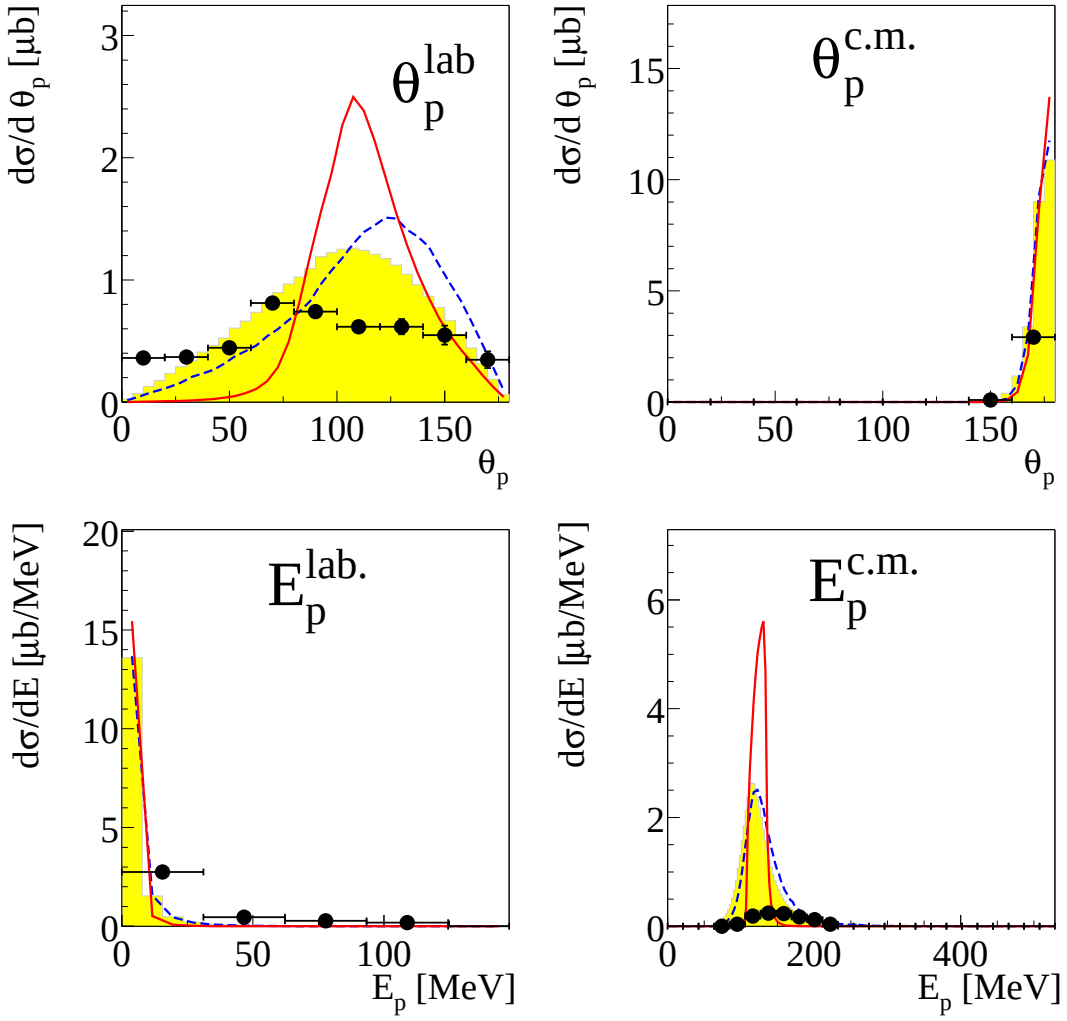

Figure C 4.1: Kinetic energy and angular distributions of spectator proton in labor and centre of mass systems at $T_p = 1.03$ GeV.
Uncorrected data (black points) are compared to the Monte Carlo through detector data (yellow filled area). Monte Carlo data are simulated according to the model described in Chap. 5.3.2.

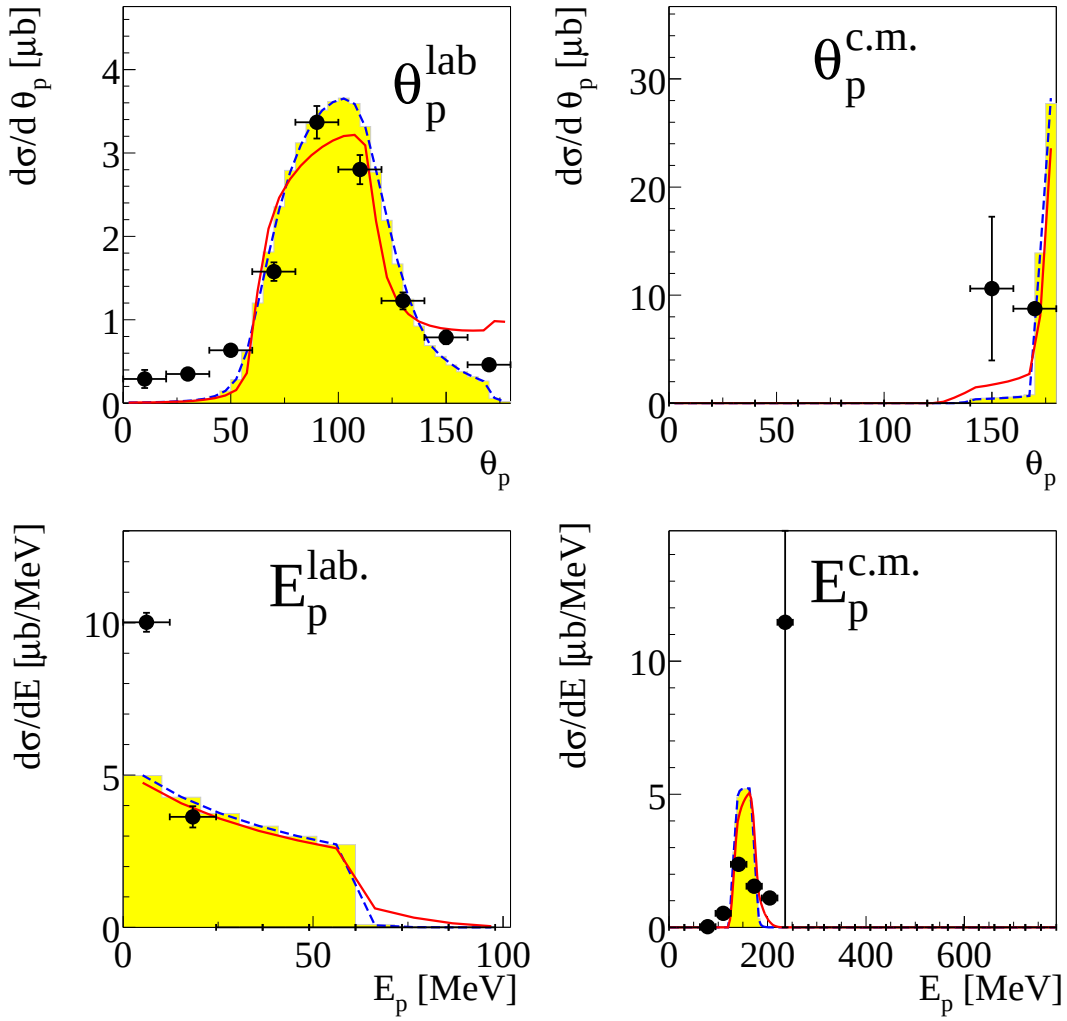

Figure C 4.2: Kinetic energy and angular distributions of spectator proton in labor and centre of mass systems at $T_p = 1.35$ GeV.
Uncorrected data (black points) are compared to the Monte Carlo through detector data (yellow filled area). Monte Carlo data are simulated according to the model described in Chap. 5.3.2.

Bibliography

[Aba60] A. Abashian, N.E. Booth, K. Crowe, *Possible Anomaly in Meson Production in $p + d$ Collisions*, Phys. Rev. Lett. **5**, 258 (1960)

[Aba61] A. Abashian et al., *Anomaly in Meson Production in $p + d$ Collisions*, Phys. Rev. Lett. **7**, 35 (1961)

[Abd06] M. Abdel-Bary et al., *Study of spectator tagging in the reaction $np \rightarrow pp\pi^-$ with a deuteron beam*, Eur. Phys. J. A, 353-361 (2006)

[Abd03] S. Abdel-Samad et al., *Isospin symmetry breaking and scaling observed in pion production in $p + d$ reactions*, Phys. Lett. **B553**, 31-37 (2003)

[Abd79] A. Abdivaliev et al., *Analysis of the Production Mechanism of Narrow Enhancements in the Effective Mass Spectrum (pi+ pi-) in the Reaction $np \rightarrow d\pi^+\pi^-$ at a Neutron Incident Momentum of P (n) = 1.73-GeV/c*, Sov. J. Nucl. Phys. **29**, 796 (1979)

[Alv98] L. Alvarez-Ruso, E. Oset, E. Hernández, *Theoretical Study of the $NN \rightarrow NN\pi\pi$ reaction*, Nucl. Phys. **A633**, 519 (1998)

[Alv99] L. Alvarez-Ruso, *The role of the Roper resonance in $np \rightarrow d(\pi\pi)^0$*, Phys. Lett. **B452**, 207 (1999)

[Alv99a] L. Alvarez-Ruso, PhD thesis, University of Valencia (1999)

[And00] M. Andersson et al., *Isospin resolved double pion production in the reaction $p + d \rightarrow^3 He + 2\pi$*, Phys. Lett. **B485**, 327 (2000)

[Anj73] J.C. Anjos, D. Levy, A. Santoro, *Dynamical model for the ABC effect*, Nucl. Phys. **B67**, 37 (1973)

[Ban71] J. Banaigs et al., *Observation de l'effet "ABC" et d'une structure a 450 MeV dans des spectres de masse manquante mesonique*, Nucl. Phys. **B28**, 509 (1971)

[Ban73] J. Banaigs et al., Nucl. Phys. **B67**, 1 (1973)

[Ban73a] J. Banaigs et al., *Observation of the ABC effect in the reaction $d + d \rightarrow \alpha + (mm)^0$*, Phys. Lett. **B45**, 394 (1973)

[Ban76] J. Banaigs et al., *A study of the inclusive reaction $d + d \rightarrow^4 He + X$, the ABC effect, and I = 0 meson resonances*, Nucl. Phys. **B105**, 52 (1976)

[Bar73] I. Bar-Nir et al., *Analysis of the reaction $np \to d\pi^+\pi^-$ below 3.5 GeV/c*, Nucl. Phys. **B54**, 17 (1973)

[Bar75] I. Bar-Nir, T. Risser, M.D. Shuster, *The ABC effect in the reaction $NN \to d\pi\pi$*, Nucl. Phys. **B87**, 109 (1975)

[Bash06] M. Bashkanov et al., *Exclusive measurements of $pd \to^3 He\pi\pi$: The ABC effect revisited*, Phys. Lett. **B637**, 223-228 (2006)

[Bash06a] M. Bashkanov, *Double Pionic Fusion: Towards an Understanding of the ABC Puzzle by Exclusive Measurements* , PhD thesis, Universität Tübingen, 2006

[Bash07] M. Bashkanov et al., Int.J. Mod. Phys. **A22** 625 (2007)

[Bash07a] M. Bashkanov et al., eConf C070910, 129 (2007)

[Bash07b] M. Bashkanov et al., Phys. Rev. **C76**, 048201 (2007)

[Bash08] M. Bashkanov et al., Proc. MENU07, econf C070919, 207 (2008)

[Bash08a] M. Bashkanov et al., Prog. Part. Nucl. Phys. **61**, 304 (2008)

[Bash08b] M. Bashkanov et al., Nucl. Phys. **A805**, 146 (2008)

[Bash08c] M. Bashkanov et al., Proc. MESON08, Int. J. Mod. Phys., in press

[Bash08d] M. Bashkanov et al., talk at PANIC08, to appear in proc. PANIC08

[Bash09] M. Bashkanov et al., *Double-Pionic Fusion of Nuclear Systems and the "ABC" Effect: Approaching a Puzzle by Exclusive and Kinematically Complete Measurements*, Phys. Rev. Lett. **102**, 052301 (2009)

[Bash] M. Bashkanov, private communication

[Bel99] E. Bellemann et al., *Pion-pion p-wave dominance in the $pd \to^3 He\pi^+\pi^-$ reaction near theshold*, Phys. Rev. **C60**, 061002(R) (1999)

[Bil97] R. Bilger et al., *CELSIUS as an eta factory*, Nucl. Phys. **A626**, 93c-96c (1997)

[Boo63] N.E. Booth et al., Phys. Rev. **122**, 2314 (1963)

[Bro01] W. Brodowski, *Measurement of Two Pion Production in Proton Proton Collision at 750 MeV*, PhD thesis, Universität Tübingen, 2001

[Bys87] J. Bystricky et al., J. Phys. (Paris) **48**, 1901 (1987)

[Cal96] H. Calén et al., *Detector setup for a storage ring with an internal target*, Nucl. Instrum. Meth. Phys. Res. A**379**, 57-75 (1996)

[Cal00] H. Calén and A. Kupść, Overview of the CELSIUS/WASA Offline Programs, Manual, 1992 (2000)

[CER93] CERNLIB - Catalog of Program packages and entries, CERN Program Library Short Writeups, 1993

[CER93a] GEANT - Detector Description and Simulation Tool, CERN Program Library Long Writeups W5013, 1993

[CER99] PAW - Physics Analysis Workstation User's Guide, CERN Program Library Long Writeups Q121, 1999

[Clem] H. Clement, private communication

[Cra70] Craun et al., NIM 80, 239-244 (1970)

[Dak83] L.G. Dakhno et al., *Measurement of the cross sections for production of pion pairs in nucleon-nucleon collisions at energies below 1 GeV. Isospin analysis*, Sov. J. Nucl. Phys. **37**(4), (1983)

[Dem05] L. Demirörs, *Investigating Interactions of Deuterons and Protons with the Hydrogen Pellet Target of the CELSIUS/WASA Experiment*, PhD thesis, Universität Hamburg, 2005

[Edm64] A.R. Edmonds, *Drehimpulse in der Quantenmechanik*, Bibliographisches Institut AG, Mannheim 1964

[Eks96] C. Ekstroem et al., Hydrogen pellet targets for circulating particle beams, Nucl. Instrum. Meth. Phys. Res. A **371**, 572-574 (1996)

[Fran] K. Fransson, private communication

[Fra95] H. Frauenfelder, E.M. Henley, *Teilchen und Kerne*, Subatomare Physik, 3 Auflage, R. Oldenbourg Verlag München Wien, 1995

[For02] Forschen in Jülich, Forschungszentrum Jülich in der Helmholtz-Gemeinschaft, Zeitschrift, 01/2002

[Gar98-99] A. Gardestig, G. Faldt, C. Wilkin, Phys. Rev. **C59**, 2608 (1999) and Phys. Lett. **B421**, 41 (1998)

[Gre99] J. Greiff, *Investigation of Inelastic Reactions in Deuteron Proton Collisions Between $T_d = 437$ and $559MeV$ using the PROMICE/WASA Detector at CELSIUS*, PhD thesis, Universität Hamburg, 1999

[Häg97] S. Häggström, *Production of η - meson in Proton - Neutron Collisions*, PhD thesis, Uppsala Universitet, 1997

[Hal69] J.H. Hall et al., *Evidence for a low - energy s-wave $\pi - \pi$ interaction and a possible doubly charged dibaryon enhancement*, Nucl. Phys. **B12**, 573 (1969)

[HBO95] CERN Computing and Networks DIVISION, *HBOOK - Statistical Analysis and Histogramming, Reference Manual*, CERN Program Library Long Writeup W5013, 1995

[Hom64] R.J. Homer et al., *Evidence for an anomaly in two pion production*, Phys. Rev. Lett.**9**, 72 (1964)

[Jac04] M. Jacewicz, *Measurement of the reaction $pp \rightarrow pp\pi^+\pi^-\pi^0$ with CELSIUS/WASA at 1.36 GeV*, PhD thesis, Uppsala Universitet, 2004

[Kas04] M. Kaskulov, H. Clement, *Correlated two-pion exchange in peripheral NN scattering*, Phys. Rev. **C70**, 057001 (2004)

[Kel08] S. Keleta, *Double Pion Production in the $dd \rightarrow \alpha\pi\pi$ Reaction*, PhD thesis, Uppsala Universitet, 2008

[Kha07] O. Khakimova et al., Int. J. Mod. Phys. **22**, 617 (2007)

[Kha08] O. Khakimova et al., Proc. MENU07, econf C070910, 307 (2008)

[Koc04] I. Koch, *Measurements of $2\pi^0$ and $3\pi^0$ Production in Proton-Proton Collisions at a Centre of Mass Energy of 2.465 GeV*, PhD thesis, Uppsala Universitet, 2004

[Kop96] H. Kopka, *LaTeX*, 2 Auflage, Addison-Wesley, 1996

[Kup95] A. Kupść, *Note on kinematical fit*, 1995

[Kup02] A. Kupść ,*CWlib C++ Libraries for CELSIUS/WASA*, Manual, 2002

[Kre08] F. Kren et al., Proc. MESON08, Int. J. Mod. Phys., in press

[Kre09] F. Kren, Dissertation (in Vorbereitung), Universität Tübingen (2009)

[Kre03] J. Kreß, *Entwicklung und Installation eines Zentralkalorimeters und Messungen der Reaktion $\vec{p}p \rightarrow pp\pi^+\pi^-$ mit spin-polarisierten Protonen am Flugzeitspektrometer COSY-TOF*, PhD thesis, Universität Tübingen, 2003

[Kuk01] V.I. Kukulin et al., *Dressed six-quark bags at short and intermediate NN ranges*, Nucl. Phys. **A689**, 327c (2001)

[Leo87] W.R. Leo, *Techniques for Nuclear and Particle Physics Experiments*,Springer-Verlag Berlin, Heidelberg, 1987

[Mar01] P. Marciniewski, *Fast digital trigger systems for experiments in high energy physics*, PhD thesis, Universitet Uppsala, 2001

[Mos99] C.A. Mosbacher, F. Osterfeld, *Double Δ (1232) excitation and the ABC effect in the reaction $n + p \rightarrow^2 H(\pi\pi)$*, nucl-th/9903064

[Pau06] C. Pauly, *Light Meson Production in pp Reactions at CELSIUS/WASA above the η Threshold*, PhD thesis, Universität Hamburg, 2006

[Pau] C. Pauly, private communication

[Pät02] J. Pätzold, *Exclusive Measurement of the $pp \rightarrow pp\pi^+\pi^-$ Reaction Close th Theshold*, PhD thesis, Universität Tübingen, 2002

[Per] E. Perez del Rio, Dissertation (in Vorbereitung), Universität Tübingen, 2009

[Plo78] F. Plouin et al., *Observation of the ABC Effect in the reaction* $n + p \rightarrow d+(mm)^0$ *with a 1.88 GeV/c Neutron Beam*, Nucl. Phys. **A302**, 413 (1978)

[Plo90] F. Plouin, P. Fleury, C. Wilkin, *Identification and analysis of the* $np \rightarrow d\eta$ *cross section near threshold*, Phys. Rev. Lett. **65**, 6 (1990)

[Pra00] D. Prasuhn et al., *Electron and stochastic cooling at COSY*, Nucl. Instr. and Meth. A**441**, 167 (2001)

[Pri] A. Pricking, private communication

[Pri06] A. Pricking, *WASA-at-COSY: Forward Detector Extension*, Poster, 2006

[Pri] A. Pricking, Dissertation (in Vorbereitung), Universität Tübingen - Bonn (2009)

[PDG06] Particle Physics Booklet, W.-M. Yao et al., Journal of Particle Physics G **33**, 1 (2006)

[Ris73] T. Risser and M.D. Shuster, *Anomalous Enhancements in Multiple-Pion Production with Deuterons*, Phys. Lett. **43B**, 68 (1973)

[ROOT] ROOT - An Object-Oriented Data Analysis Framework, http://root.cern.ch

[Roz88] F.M. Rozon, N. Grino, R. Rui, Nucl. Instr. Methods **A 267**, 101 (1988)

[Rub99] R. Ruber, *An ultra-thin-walled superconducting solenoid for meson-decay physics*, PhD Thesis, Universitet Uppsala, 1999

[SAID] SAID - Scattering Analysis Interactive Dial-in, http://said-hh.desy.de

[Sio00] U. Siodlaczek, *Photoproduktion neutraler Pionen am Deuteron*, PhD thesis, Universität Tübingen (2000)

[Sko05] T. Skorodko et al., Int. J. Mod. Phys. **A20**, 671 (2005)

[Sko07] T. Skorodko et al., Proc. MENU07, econf C070910, 392 (2008)

[Sko08] T. Skorodko et al., Proc. MESON08, Int. J. Mod. Phys. in press

[Sko09] T. Skorodko, Dissertation (in Vorbereitung), Universität Tübingen (2009)

[TSL99] The Svedberg Laboratory, Brochure, 1999

[Yuk35] H. Yukawa, *On the Interaction of Elementary Particle, 1*, Proc. Phys. Math. Soc. Jpn **17**, 48 (1935)

[Zło] J. Złomanczuk, private communication

List of Publications

M. Bashkanov et al., *Exclusive measurements of $pd \to {}^3He\pi\pi$: The ABC effect revisited*, Phys. Lett. **B637**, 223-228 (2006)

M. Bashkanov et al., *Two-pion production in the Delta Delta region: Is the ABC-effect the result of a resonance in the $pn \to \Delta\Delta$ system?*, AIP Conf.Proc.950:256-258,2007

H. Clement et al., *Single- and Double-Pion Production in Nucleon Collisions on the Nucleon and on Nuclei - the ABC Effect and its Possible Origin in a Dibaryonic Resonance*, Prog.Part.Nucl.Phys.61:276-282, 2008

M. Bashkanov et al., *Low-mass $\pi\pi$ enhancement in baryonic $\pi\pi$ production: ABC effect revised by exclusive measurements*, Int.J.Mod.Phys.A22:625-628, 2007

O. Khakimova et al., *Observation of the ABC effect in the first exclusive measurements of $pn \to d\pi^0\pi^0$*, Int.J.Mod.Phys.A22:617-620, 2007

T. Skorodko et al., *$\pi\pi$ production in proton proton collisions*, Int.J.Mod.Phys.A22:509, 2007

M. Bashkanov et al., *Large sigma channel low-mass enhancement in exclusively measured double pionic fusion to ${}^3He$*, AIP Conf.Proc.842:440-442, 2006

T. Skorodko et al., *Two-pion production in nucleon-nucleon collisions and the ABC-effect: Approaching a puzzle by exclusive and kinematically complete measurements*, Yalta 2006, New trends in high-energy physics, 119-130

H. Clement et al., *Evidence for a 'narrow' roper resonance: The Breathing mode of the nucleon*, Yalta 2006, New trends in high-energy physics, 23-32

P. Thorngren Engblom et al., *Anisotropy in the pion angular distribution of the reaction $pp \to pp\pi^0$ at 400 MeV*, Phys.Rev.C76:011602, 2007

M. Bashkanov et al., *On the $\pi\pi$ production in free and in-medium NN collisions: sigma-channel low-mass enhancement and $\pi^0\pi^0$ / $\pi^+\pi^-$ asymmetry*, Acta Phys.Slov.56:285-297, 2006

H. Clement et al., *Two-pion production, gamma gamma line and aspects of sigma meson, Bose-Einstein correlations and isospin breaking*, Int.J.Mod.Phys.A20:1747-1752, 2005

H.-H. Adam et al., *Proposal for the wide angle shower apparatus (WASA) at COSY-Julich: WASA at COSY*, nucl-ex/0411038

M. Bashkanov et al., *Structure around the $\pi\pi$ threshold in $pp \to pp\gamma\gamma$ and its possible interpretation as $\sigma \to \gamma\gamma$*, Int.J.Mod.Phys.A20:554-556, 2005

K. Schonning et.al., *Production of ω in $pd \rightarrow {}^3He\omega$ at kinematic threshold*, Proc ETA05, Acta Physica Slovaca 56 (2006) 299

M. Jacewicz et. al., *First results on $\eta \rightarrow \pi^+\pi^-e^+e^-$*, Proc ETA05, Acta Physica Slovaca 56 (2006) 367

C. Pauly et al., *Production of $3\pi^0$ in pp reactions above the η production threshold and the quadratic slope parameter α*, Proc ETA05, Acta Physica Slovaca 56 (2006) 381

M.Bashkanov et. al., *Low-mass enhancement in baryonic $\pi\pi$ production: ABC effect revised by exclusive measurements*, Int.J.Mod.Phys. A22,625-628, 2007

M.Bashkanov et. al., *Measurements of the slope parameter for the $\eta \rightarrow 3\pi^0$ decay in the $pp \rightarrow pp\eta$ reaction*, Phys.Rev.C76, 048201, 2007

M.Bashkanov et. al., *σ-channel low-mass enhancement in double-pionic fusion*, MENU07, econf C070919, 207 (2008)

T. Skorodko et al., *Excitation of the Roper resonance in single and double-pion production*, MENU07, econf C070910, 392 (2008)

O. Khakimova, et al., *Measurement of the ABC effect in the most basic double-pionic fusion process*, MENU07, econf C070910, 307 (2008)

M.Bashkanov, et al., *σ-channel threshold enhancement in double-pionic fusion*, Hadron07 Conf. Proc. to be published.

M. Berłowski et al., *Measurement of eta meson decays into lepton-antilepton pairs*, Phys. Rev. D,77, 032004

H. Clement et al, *Single and double-pion production in nucleon collisions on the nucleon and on nuclei-the ABC effect and its possible origin in a dibaryonic resonance*, Proc. Int. School Nucl. Phys., 29th course on Quarks in Hadrons and Nuclei, Erice 2007 (to be published in Progress in Particle and Nuclear Physics)

Chr. Bargholtz et al., *The WASA detector facility at CELSIUS*, Nuclear Instruments and Methods in Physics Research Section A, Volume 594, Issue 3

C. Pauly et al., *The $pp \rightarrow pp\pi\pi\pi$ reaction channels in the threshold region*, Physics Letters B, Volume 649, Issue 2-3, p. 122-127

K. Shoenning et al., *Polarisation of the ω meson in the $pd \rightarrow {}^3He\omega$ at 1360 and 1450 MeV*, Phys. Lett. B, **668**, 258-262 (2008)

M. Bashkanov et al., *Double-Pionic Fusion of Nuclear Systems and the "ABC" Effect: Approaching a Puzzle by Exclusive and Kinematically Complete Measurements*, Phys. Rev. Lett. **102**, 052301 (2009)

Conference contributions

π^0 and π^- production in NN collisions at $T_N \geq 0.8$ GeV and $pn \to d\pi^0\pi^0$ at 1.1 GeV, DPG Frühjahrstagung 2006 in München, contributed talk

π^0 and π^- production in NN collisions at $T_N \geq 0.8$ GeV and $pn \to d\pi^0\pi^0$ at 1.1 GeV (ABC-effect), MESON2006, contributed talk

Low-mass $\pi\pi$ enhancement in double pionic fusion processes, NPAE-2006 in Kiev, contributed poster

Measurement of the ABC-effect in the most basic double-pionic fusion process, MENU2007 in Jülich, contributed talk

Measurements of the ABC effect in the most basic double-pionic fusion reaction $pn \to d\pi^0\pi^0$, DPG Frühjahrstagung 2008 in Darmstadt, contributed poster